2013

Micro Surface Texturing for Friction Control

Ola Rashwan
University of Windsor

Recommended Citation

Rashwan, Ola, "Micro Surface Texturing for Friction Control" (2013). *Electronic Theses and Dissertations.* Paper 4869.

Micro Surface Texturing for Friction Control

By

Ola Rashwan

A Dissertation
Submitted to the Faculty of Graduate Studies
through Engineering Materials
in Partial Fulfillment of the Requirements for
the Degree of Doctor of Philosophy
at the University of Windsor

Windsor, Ontario, Canada

2013

Micro Surface Texturing for Friction Control

By

Ola Rashwan

APPROVED BY:

Dr. I.D. Marinescu (External Examiner), Mechanical, Industrial & Manufacturing Engineering, University of Toledo

Dr. T. Bolisetti (Outside Program Reader), Civil & Environmental Engineering

Dr. D.O. Northwood (Program Reader), Engineering Materials

Dr. D. Green (Program Reader), Engineering Materials

Dr. V. Stoilov (Co-Advisor), Engineering Materials

Dr. A.T. Alpas (Co-Advisor), Engineering Materials

Dr. F. Schlosser (Chair of Defense), Odette School of Business

[Feb 26, 2013]

DECLARATION OF CO-AUTHORSHIP AND PREVIOUS PUBLICATION

I hereby declare that this thesis incorporates material that is result of joint research, as follows:

This thesis incorporates one original paper that has been published in [Proceedings of ASME 2012 International Mechanical Engineering Congress & Exposition]and is included in Chapter 6 of the thesis:

Thesis Chapter	Publication title/full citation	Publication status*
Chapter 6	Effect of Surface Patterning on the Adhesive Friction, Ola Rashwan, Vesselin Stoilov, Ahmet Alpas, Ariel Guerrero, Proceedings of ASME 2012 International Mechanical Engineering Congress & Exposition,Paper Number IMECE2012-89644	*Published*

In all cases, the key ideas, primary contributions, experimental designs, data analysis and interpretation, were performed by the author, Dr. V. Stoilov, and Dr. A.T. Alpas as advisors.

I certify that, with the above qualification, this thesis, and the research to which it refers, is the product of my own work.

I certify that I have obtained a written permission from the copyright owner to include the above published material in my thesis. I certify that the above material describes work completed during my registration as graduate student at the University of Windsor.

I declare that, to the best of my knowledge, my thesis does not infringe upon anyone's copyright nor violate any proprietary rights and that any ideas, techniques, quotations, or any other material from the work of other people included in my thesis, published or otherwise, are fully acknowledged in accordance with the standard referencing practices. Furthermore, to the extent that I have included copyrighted material that surpasses the bounds of fair dealing within the meaning of the Canada Copyright Act, I certify that I have obtained a written permission from the copyright owner to include such material in my thesis.

I declare that this is a true copy of my thesis, including any final revisions, as approved by my thesis committee and the Graduate Studies office, and that this thesis has not been submitted for a higher degree to any other University or Institution.

ABSTRACT

Recently, surface texturing has gained momentum as a way to control the friction which is involved in various applications and systems, such as components of internal combustion engines, dies and punches of the metal forming processes and Micro-electrical-mechanical Systems (MEMS). This dissertation demonstrates that under dry sliding, there is a specific significant surface texturing parameter at which the coefficient of friction should be at a minimum. This dissertation met this objective through an extensive study of the relevant literature on surface texturing and friction, analysing the friction mechanisms involved in dry sliding, and highlighting the key factors that control friction as the real area of contact and material properties. An analytical proof is derived demonstrating that a minimum friction force exists if the two components of the friction force, adhesion and mechanical deformation, are differentiated with respect to the real contact area. In addition, numerical simulations and experimental work were performed to test this hypothesis. In the two and three dimensional finite element models, normal and sliding contact between a rigid indenter and elastic-plastic surfaces, which are textured by circular and hexagonal dimples of different sizes and densities, are simulated and analysed. Circular craters of different sizes and densities, are fabricated using laser ablation on hardened tool steel samples, while the hexagonal dimples are fabricated using photo-lithography. The dimples are arranged in adjacent equilateral triangles layout.

Coefficients of friction were measured using a scratch tester under dry sliding conditions and constant load. In addition, adhesion forces were estimated using an Atomic Force Microscope (AFM). The adhesion force is found to be exponentially decreasing with the increase of the spatial texture density. The dimensionless quantity, spatial texture density (D/L) was identified as the most significant texturing parameter. It is equal to the ratio of the size of the crater (D) to the distance between the centers of two consecutive craters (L). A minimum coefficient of friction exits at values of spatial texture densities that lie between 0.25 and 0.5.

.

DEDICATION

I would like to dedicate this dissertation to my dad (RIP), and my little family, Mohamed, Judi and Yahya.

ACKNOWLEDGEMENTS

I would like to thank Allah for giving me the strength and endurance to accomplish this work.

I would like to thank my doctoral advisor, Dr. V.Stoilov, for his dedication and continuous support and help.

I would like to thank my co-advisor Dr. A. Alpas, for his support of the experimental work and his advice during the course of my study.

I would like to extend my thanks to my committee members, Dr. D. Northwood, Dr. D. Green, and Dr.T. Bolisetti for their time and effort during my PhD study with special thanks to Dr. D. Green and Dr. D. Northwood for reviewing this dissertation, and their continuous support and advice.

I would like to thank Ms. Kora, Dr. Edrisy, and Dr. S.Das, for their help with my experimental work.

Special thanks go to my mother, my sisters and my brother for their unconditional love and support.

I also extend my heartfelt thanks to my husband, Mohamed Ismail, for his support and encouragement.

TABLE OF CONTENTS

LIST OF TABLES

LIST OF FIGURES

LIST OF ABBREVIATIONS

AJM	Abrasive Jet Machining
AFM	Atomic Force Microscope
COF	Coefficient of Friction
LBM	Laser Beam Machining
EDS	Energy dispersive spectroscopy
LST	Laser Surface Texturing
MEMS	micro-electrical mechanical Systems
PD	Penetration Depth
RIE	Reactive Ion Etching
rms	Root mean squares
SEM	Scanning Electron Microscope
VMT	vibro-mechanical texturing
WYKO	Profilometer brand name
2DFFT	2D fast Fourier transformation function

NOMENCLATURE

a_i	*separation distance*
A	*contact area.*
A_r	*Real Area of Contact*
C	*the constant in least square fitted power law*
D	*Diameter of the texture or Pattern*
$F_{Friction}$	*Total Friction Force*
F_{adh}	*Friction force due to adhesion*
F_{def}	*Friction Force due to mechanical Deformation*
F_s	*Intermolecular Forces*
G	*Scaling Constant for fractal Surface*
H_i	*Hamaker constant for material i*
H_{ij}	*Hamaker Constant for the two materials i and j*
L	*Linear distance between the centers of any two adjacent dimples*
M	*number of largest inscribed spheres in the projected area of AFM tip*
N	*the Power constant in least square fitted power law.*
P	*contact load*
R	*radius of Rigid sphere in contact*
$\mathrm{R_C}$	*Contact Radius*
Q_{max}	*the maximum tangential force needed to shear the formed junctions*
W_a	*Work of adhesion*
$\mathrm{r_i}$	*Radius of the sphere in contact in adhesion force contact mechanics models*
μ	*Coefficient of friction*
τ	*Shear Strength of the softer material in contact.*

Chapter 1 INTRODUCTION AND LITERATURE REVIEW

1.1 Introduction

Friction is involved in thousands of applications in our daily lives. In some applications high friction is desirable, as in vehicles' tires on the roadways, brakes, clutches, and frictional power transmission systems. In other applications, friction reduction is a constant demand which reflects on energy efficiency, component durability, and system reliability. For example, the energy loss due to friction in automobiles is estimated to be 40% of the total energy generated by the internal combustion engine [1]. In all cases, understanding the mechanisms involved in friction and the means to control it are necessary. Various approaches have been employed in order to control friction, some of which are lubrication, coating, and surface modification such as texturing, which is the focus of this study.

Lubrication, whether hydrodynamic, boundary, or mixed is one solution to control friction, however, lubrication in some operating conditions is not applicable. Such conditions are observed in micro-electrical mechanical systems. In addition, surface coating is another effective means of reducing friction. High strength and low friction coating materials have been employed in a wide range of applications, yet surface coating sometimes faces the challenges of debonding and fracture of the coating layer, which may result in more catastrophic results. Therefore, researchers have been searching for a more reliable approach that can control friction in all operating conditions. Three decades ago [2], attention was drawn to surface patterning, or surface texturing, as an effective means to improve the tribological performance.

The idea of surface texturing is inspired by nature. Shark skin, for instance, boosts swim speed by cutting the drag force; therefore, the skin suits of Olympic athletes have v-shaped grooves called riblets which mimic the texture of shark skin. The gecko foot is another example from nature that inspired many adhesive systems.

Many studies have investigated the effect of surface texturing on the performance of a variety of mechanical systems. It was found that surface texturing has great potential for improving the tribological performance in terms of reducing the wear, friction, and lubrication consumption. In the following sections, a review of the surface texturing effect on friction is presented. This includes a discussion of the surface texturing parameters, the different benefits of the textured surfaces based on lubrication regimes, the various methods which are used to fabricate the textured surface, and the applications that widely employ micro-surface texturing.

1.2 Surface Texturing Parameters

Different texture parameters, such as shape, size, density, depth, and orientation, or a combination of these parameters, control the effectiveness of the surface texture on tribological performance.

In general, surface texture may be positive, in that it protrudes out of the surface, or negative, such as dimples or holes. It can also be made up of continuous grooves, channels, or undulations. It can be discrete shapes, such as circular, square, triangular, or hexagonal, that are distributed evenly or randomly.

Positive surface textures are used extensively in micro-electrical mechanical systems (MEMS), and magnetic hard disks to decrease the friction by decreasing the area of contact. Negative texturing, which is the focus of the current study, is mostly employed in automotive components, and in machining tools and punches for metal forming processes.

1.3 Benefits of Surface Texturing

The role of the surface texturing in improving the tribological properties varies based on the contact conditions, whether they are hydrodynamic (full), mixed, boundary, or dry conditions. In the case of the full or mixed lubrication conditions, the micro-craters serve as micro-hydrodynamic bearings that increase the hydrodynamic pressure due to asymmetric pressure distribution, therefore the load carrying capacity increases [2-18]. In mixed lubrication conditions, this additional lift in hydrodynamic pressure alters the balance between hydrodynamic and boundary lubrication, consequently the number of the asperities in contact decreases, and friction and wear decrease [2-5, 14, 19-22].

In boundary lubrication these craters act as lubricant reservoirs for the continuous retention of lubricant [5, 12, 23-28], and for dry sliding the surface texture acts as wear debris traps so that plowing decreases. Consequently, abrasive wear and friction are reduced [2, 5, 27, 29-33].

1.4 Surface Texturing Fabrication Methods

Various machining methods have been employed to create micro-texturing on the surface of different materials. Schneider [34] developed the vibro-rolling method to create shallow channels using a hard indenter that vibrates as it translates across the workpiece. Suh et al. [28] used chemical etching and abrasive machining to create modulated or undulated patterns that act as traps for oxide wear debris, and Willis [35] used honing to generate micro-grooves for the cylinder bores of internal combustion engines. The micro-grooves improve the lubrication between the cylinder walls and the piston ring.

Reactive ion etching (RIE) was used by Wang et al. [14-16, 21] to explore the influence of micro-dimples on the silicon carbide surface sliding in water. Large circular dimples and small square depressions are fabricated using Reactive Ion Etching, where high energy chemical plasma is directed at the part causing surface material removal. The details of the fabrication steps are depicted in Figure 1-1 [14-15].

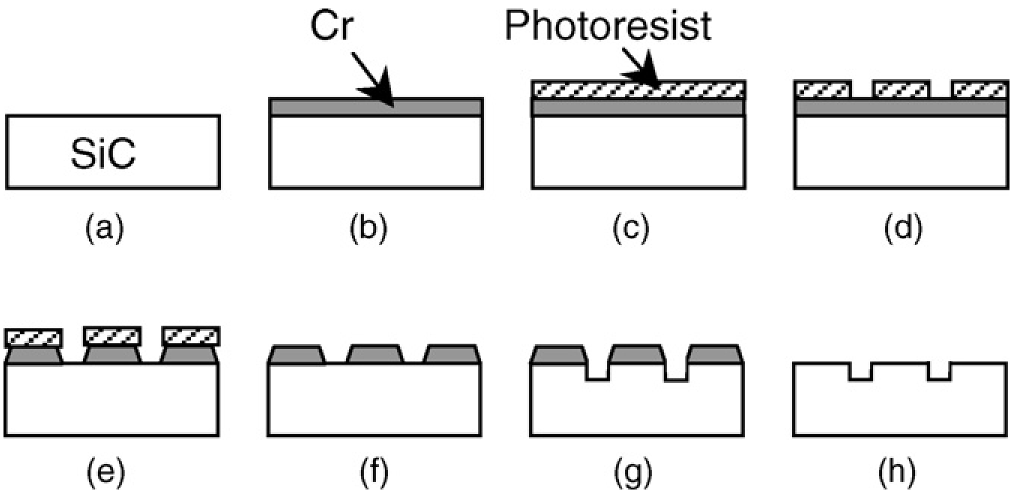

Figure 1-1: Fabrication Process for Reactive Ion Etching[15]

Pattersson and Jacobson [27] used a standard photolithographic technique, with Potassium Hydroxide as anisotropic etchant, to create runners and square depressions of 5µm in depth on silicon wafers. The standard steps for the anisotropic etching of silicon wafers are illustrated in Figure 1-2.

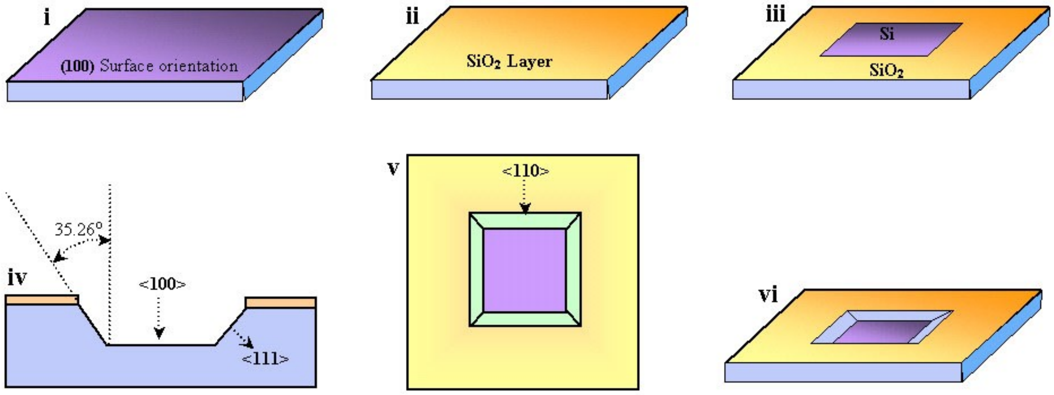

Figure 1-2: Standard Etching for Si Wafers [36]

Wukada et al. [25] employed abrasive jet machining (AJM), where the surface is bombarded with high velocity fine abrasive particles that cause the physical removal of material. Excimer laser beam machining (LBM) was also used by the same group. These two fabrication methods result in different profile shapes, circular and angular from AJM and LBM respectively, though the effect of the texture shape is found to be insignificant.

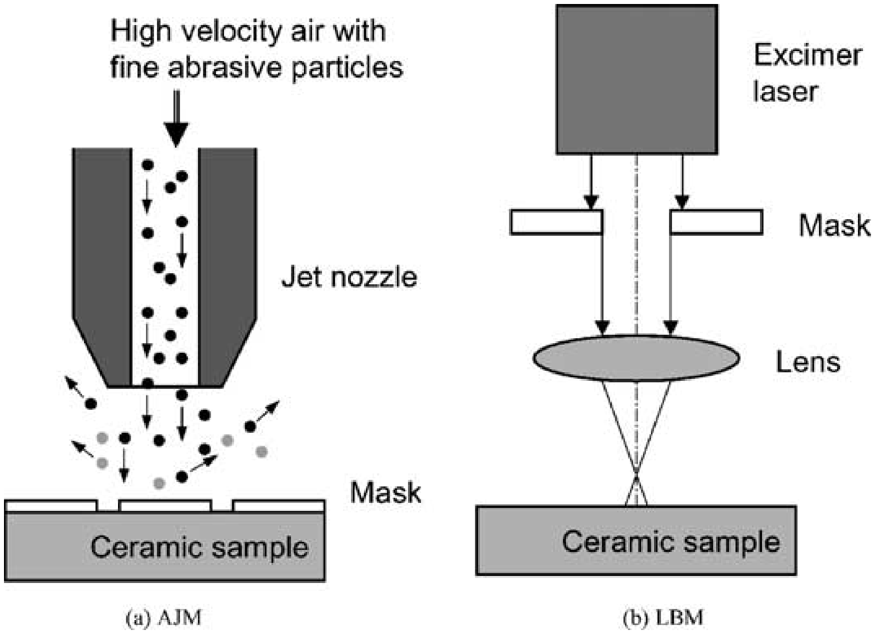

(a) AJM (b) LBM

Figure 1-3: Abrasive Jet Machining (AJM) and Laser Beam Machining (LBM) are used for Texture Fabrication [25]

The vibro-mechanical texturing (VMT) technique was developed by Greco et al. [37], and this technique is based on the conventional turning operation with a fast tool servo that is used to oscillate the cutting tool. This oscillating motion creates holes when the cutting tool contacts the work piece.

Laser surface texturing (LST) has been widely used for over 15 years in different applications [2]. In the following section, LST is discussed in detail as it has great potential for enhancing the tribological performance in a variety of applications.

1.4.1 Laser Surface Texturing (LST)

LST has many advantages over the previously mentioned texturing fabrication methods since it is very fast, environmentally clean, precise, and maskless. In addition, a variety of sizes can be created, and it can be used with most material types.

When a focused laser beam is localized on the surface of a material, the molten material evaporates immediately at a very high rate without causing severe damage to the surface or bulk material. Different types of laser beams are used to create the craters on the surface, and different media can generate the laser beam (photons). Examples of the gaseous media are He-Ne, Ar, Kr, Xe, N_2, and CO_2. Excimer laser beams, shown in Figure 1-4 [19] , that include halides in the ultraviolet (UV) range are ArF, KrF, XeCl, and XeF, and they are used frequently to create patterns in the hard coating layer, such as TiN, CrN, and DLC. Another type of laser medium is a metallic vapour, such as Cu, Au, HeCd, HeSe, and HeHg. In addition, the semiconductor media are GaN and GaAs based, and finally the most popular type, which is extensively used in the micro-machining, is the solid state media Nd:YAG laser.

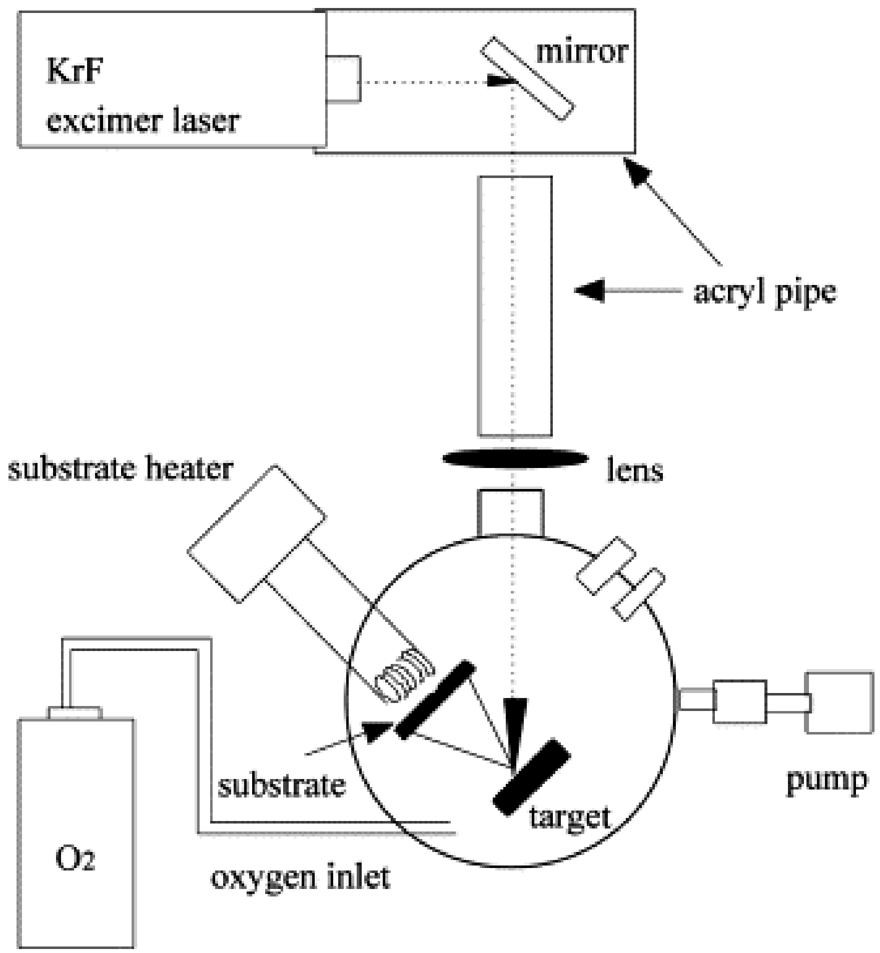

Figure 1-4: Excimer Laser Beams[19]

Many of the parameters of laser surface texturing must be optimized in order to get high quality, precise micro-craters. The resolution, for instance, depends on the wavelength of the laser source, whereas the ablation rate is based on energy density, and the depth of the craters is controlled by the number and duration of the pulses [38].

A statistical study [6] explored the effect of variations in crater size which results from the manufacturing process on the load carrying capacity and film thickness. One hundred cases with different dimple sizes that follow normal distribution were analyzed. The study [6] concluded that variations in the dimple depth and diameter have only a small effect on the load carrying capacity, but this variation in texture size affects the film thickness, which in turn affects the expansion of the hydrodynamic regime.

1.5 Optimization of the Surface Texturing Parameters

Most of the research done on surface texturing is experimental, except for a few analytical studies that try to optimize the surface texture parameters. In the following subsections, analytical studies are reviewed and followed by experimental investigations.

1.5.1 Analytical Studies of Optimization of the Surface Texturing Parameters.

Zhao et al. [39] studied the effects of micro-pores as lubricant reservoirs for a highly-loaded, boundary lubrication condition. This research developed a finite element model of a rigid cylinder in contact with an elastic and elastic-plastic half-space with lubricant filled micro-pockets. The results showed a reduction in the volume of these micro pores with loading, therefore if those pockets are filled with lubricant, the squeezed lubricant will partially support the applied load. This reduces the surface-to-surface contact between the rigid cylinder and the textured surface. Comparing the empty micro-pore with the micro-pore filled with lubricant, the pressure spikes and the sub-surface stresses of the filled micro pore are lower than in the empty one.

Sirpuram and Stephens [11, 40] addressed the effects of different texture shapes of positive and negative texturing. Square, diamond, circular, triangular and hexagonal shapes were modeled, with different area densities under a hydrodynamic lubrication condition. Two objectives were sought in this study, the effects of the shape and the texture areal density on the coefficient of friction and leakage rate. They concluded that the shape of the texture has an insignificant effect on the friction coefficient; however it had a great impact on the leakage rate. The square pattern provided the worst leakage rate, and the triangular pattern gave the best leakage rate. In addition, the texture areal density affects the minimum friction coefficients, which were obtained at 20% and 80% of the areal texture coverage for the positive and negative texturing, respectively.

Kligerman and Etsion [41] developed a theoretical model to identify the most significant parameters under hydrodynamic sliding conditions, specifically for mechanical seals. Based on the findings of an earlier study that promoted evenly distributed micro-textured patterns in order to increase the load carrying capacity, hemispherical dimples arranged in a rectangular layout were modeled. This study suggested that an optimal texture size could be found based on lubricant properties, pressure difference across the seal, and the areal density of the texture. A more sophisticated model [42-43] was developed by the same group, incorporating more accurate cavitation data and using a non-spherical pattern. It was found that the most significant parameter was the diameter to depth ratio. A diameter to depth ratio of 0.05 was identified as the optimal value, versus a ratio of 0.5 which was obtained from the first model of a hemispherical pattern [41]. The improved model showed agreement with the experimental results that involved a simple sliding textured rig.

Etsion et al. [7, 9] developed another analytical model to simulate the piston ring-cylinder liner system. The ring and liner were modeled as two parallel flat surfaces where only the ring surface was dimpled, and a reduction of 30% in friction was obtained. The optimal diameter to depth ratio was found to be between 0.1 and 0.18, and areal texture densities varied from 5% to 20% which contradicted with the values found by Stephen[40]. This analytical study showed a similar trend to the experimental test, however, the exact values differed due to the adjustment in the lubricant viscosity assumed in the analytical study.

Tnder [12, 44] proved analytically that a micro textured region can replace a macro feature, such as step or inclined plane, in creating hydrodynamic pressure in sliding seals. The role of either the macro feature or the proposed micro textured area is to decrease the friction which the entering flow to the seal encounters. In this analytical study, grooves oriented perpendicularly to the flow direction were modeled, as well as square and circular discrete dimples. All texturing designs showed improvement in the hydrodynamic pressure and the leakage rate.

1.5.2 Experimental Studies on the Effect of Surface Texturing on Friction

In the analytical methods, the mechanisms that control friction must be accurately defined; on the other hand, various tribometers (pin-on-disk, ball slider, or scratch tester) can directly measure the friction coefficient. Many researchers have investigated the effects of surface texturing on the friction experimentally under different sliding conditions. However, most of these studies focus on wet conditions.

Kovalchenko et al. [8] looked into the effects of laser surface texture on the lubrication regime transition. Specifically, the effects of the sliding speed, normal pressure, and the lubricant viscosity on the friction were tested. A pin-on-disk apparatus was used in this case, and the laser surface texturing had more impact on friction in cases of higher normal loads, higher sliding speed, and higher viscosity.

Pettersson and Jacobson [27] studied the effects of the surface texturing of coated silicon under boundary and dry sliding conditions. Etched silicon samples were coated with either TiN or DLC. This study showed the critical impact of the material interaction under oscillating sliding by a ball slider. Two texturing designs were investigated, grooves and square dimples as shown in Figure 1-5. The results of this study were compared to untextured samples. Under boundary lubrication conditions, the DLC coating with square dimples showed stable low friction behavior, while the grooved texture showed high friction. The textured TiN coating behaved differently and showed unstable friction behavior on all texturing patterns. In dry sliding conditions, the DLC coating showed high friction when compared to the untextured surface. DLC has self-lubricating properties where a thin low friction tribofilm was formed on the surface. When the DLC coated sample was textured, the sharp edges of the pores scraped off the thin tribofilm causing the fluctuations in the friction behavior. On the other hand, the TiN textured samples showed low friction with both the square and groove patterns.

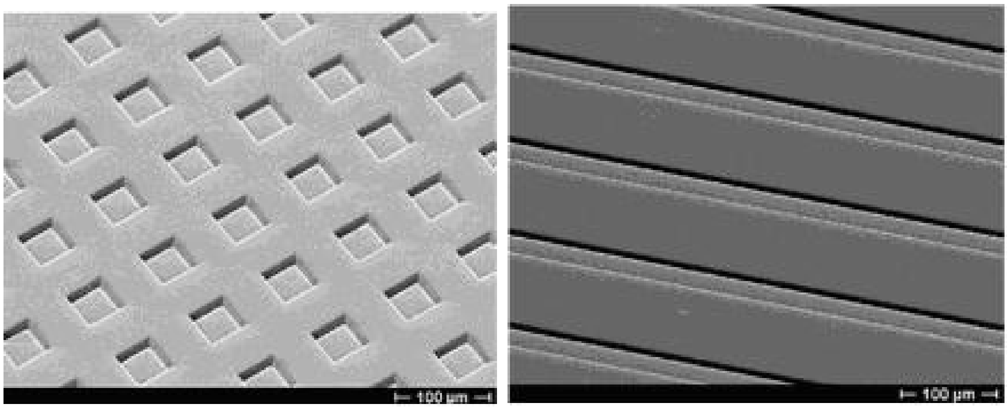

Figure 1-5: Textured squares and grooves by Pettersson and Jacobson [27]

Another study was carried out by Ryk et al. [45] that showed the negative effect of dimples under boundary lubrication conditions, if the depth of the groove is not appropriately chosen, or if the lubricant feed rate is not sufficiently high. This study showed that the deeper the dimples are, the higher the friction is. In addition, at a very low rate of lubricant supply, the friction resulting from the textured surface is higher than that of the flat surface.

Suh and others [23-24, 28, 32, 46] tested the effect of the width and orientation of undulations with respect to the sliding direction on the friction and wear, under boundary sliding conditions. Pin-on-disk tests were done, with the disks textured by abrasive machining. Grooves which were parallel to the sliding direction showed no improvement in either friction or wear. Yet, grooves perpendicular to the sliding direction decreased both the wear and friction. In addition, attention was drawn to the effect of the lubricant properties on the results.

Dumitru et al. [47] investigated the effects of micro dimples on steel disks under mixed lubrication conditions. The micro surface texturing dimples were arranged in arrays of micro-holes as shown in Figure 1-6. The diameters ranged between 50 to 100 μm and the depths were between 5 to 8 μm. The spacing distance of the holes ranged between 30 to 60 μm. The study showed eight times the improvement of the lifetime of the samples. The lifetime of the sample was defined as the sliding distance at which the coefficient of friction increased rapidly and reached the coefficient of friction of an un-textured surface.

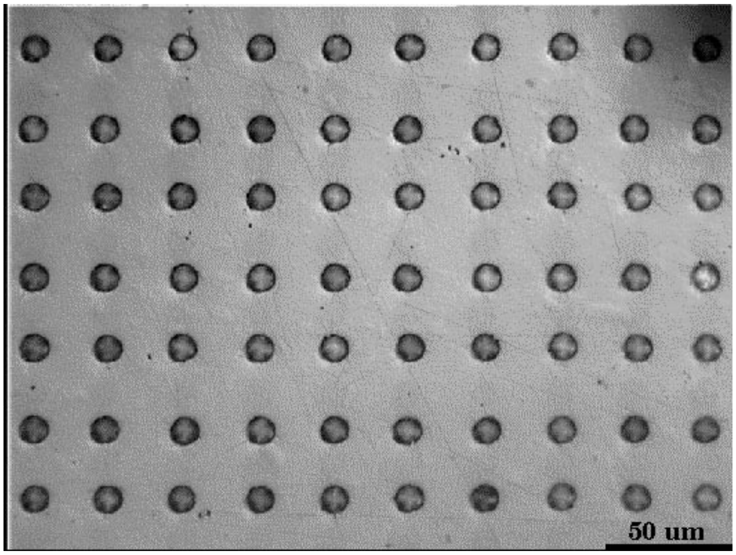

Figure 1-6: Circular Dimples Arranged in a Square Pattern[47].

Varenberg et al. [48] investigated the influence that groove depth had on wear and friction. In the cases where friction was concerned, wider grooves lead to greater friction reduction due to the fact that more wear particles could be contained in the grooves. Friction also decreased with the groove depth to a point, after which increasing the depth had no effect. They deduced that wear debris fell into the surface depressions. The particles first gathered around the edge of a dimple and then built inward and downward, not necessarily ever reaching the bottom. Once the depth of the groove was below the lowest particle size that the wear particles could reach, there was no benefit to creating a deeper groove.

1.6 Applications of Surface Texturing

Surface texturing has been used in various applications for different purposes. Mainly, it is used to enhance tribological performance which includes decreased wear and friction. In this section, the applications in which surface texturing is widely used are discussed. Most of these applications are automotive components, tools and punches of metal forming processes, and micro-electrical mechanical systems (MEMS) as shown in Figure 1-7.

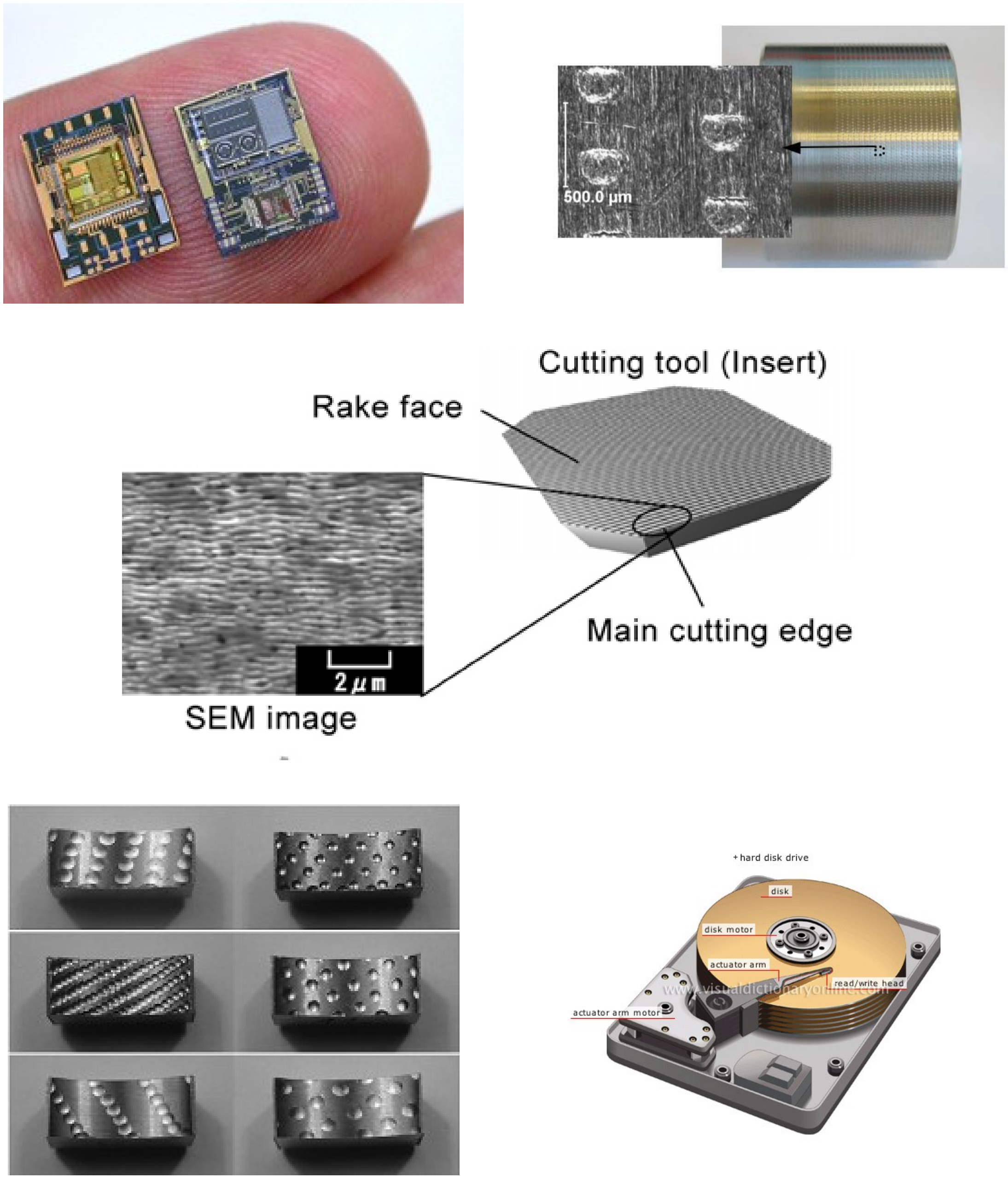

Figure 1-7: Surface Texturing in Different Applications[49]

1.6.1 Surface Texturing in Automotive Components

In 1966, Hamilton et al. [50] proposed the idea of having micro asperities act as hydrodynamic bearings in parallel sliding applications such as rotary shaft face seals. Anno et al. [51] verified that higher load carrying capacities were achieved when only one of the parallel surfaces of the rotary shaft face seals had micro-asperities in the form of cylinders.

Willis [35] used surface texturing in cylinder bores of a combustion engine. Wakuda et al. [25] investigated the influence of textured micro dimples on nitride silicon ceramic plates, which are used as a structural element in automotive engines, in contact with the hardened steel cylinder. Different texture densities, texture shapes, and texture sizes were investigated, but the texture depth was kept constant at 5 μm. Abrasive jet machining and excimer laser beam machining were used to fabricate the micro dimples with circular and angular profiles, respectively. Pin-on-disk tests were performed to measure the coefficient of friction under boundary and mixed lubrication conditions. A reduction of 20% in the coefficient of friction was obtained. The optimal texture parameters were identified as a texture size of 100 μm and a texture density of 5 to 20%. The texture shape was recognized as an insignificant factor.

Wang et al. [14] tried to find the optimum texture parameters that improved the load carrying capacity of SiC thrust bearings sliding in water. Micro pits were fabricated using RIE on one of the contact surfaces. The experiments showed that the critical load carrying capacity of the textured surface was doubled when compared to the un-textured surface for the transition between the hydrodynamic to mixed lubrication condition.

Etsion et al. [4, 7, 42, 52-53] and Yu et al. [54] used laser surface texturing on mechanical face seal rings. The results showed a significant reduction in frictional losses. The effect of the surface texturing on the friction losses by the cylinder liner-piston ring system, which was estimated at 30% of the total engine friction[55], was addressed in [9-10, 43, 45]. Friction was reduced by 30% through laser surface texturing of the cylinder liner.

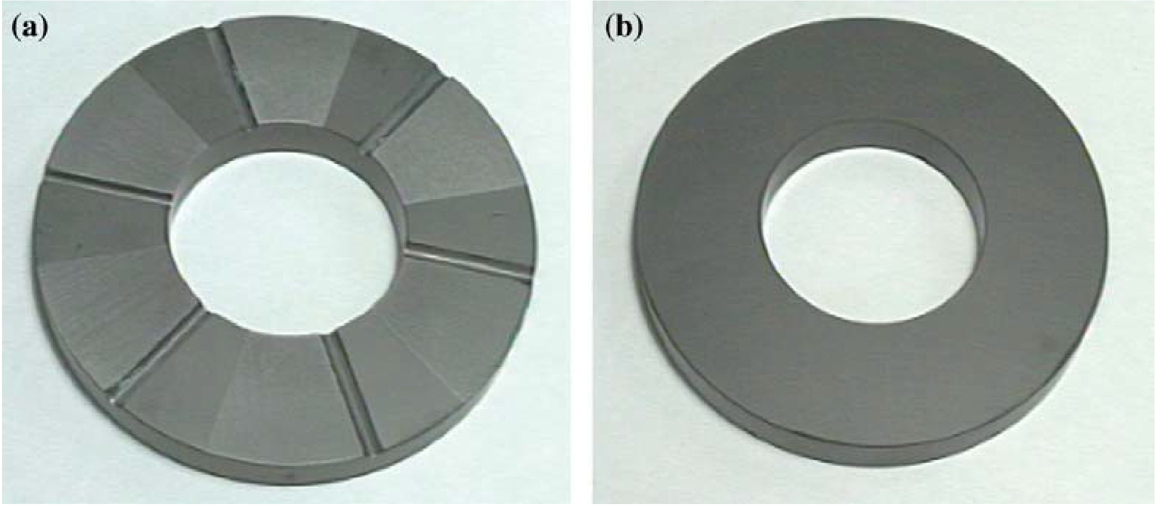

Figure 1-8: Partial surface texturing of a stator (a) in contact with plain rotor (b) [4]

1.6.2 Surface Texturing in MEMS Applications

Due to the high surface to volume ratios in MEMS, surface forces play a crucial role in adhesion and high friction between contacting surfaces. In such systems, lubrication is not an option; therefore, attention has been paid to surface texturing as an effective means to control both adhesion and friction [56].

Baumgart et al. [57] used a laser surface texturing technique to create discrete round dome-like protrusions on the inner diameter of the hard disk to reduce the stiction at the start up.

Tayebi and Polycarpou [56, 58] examined the effects of surface roughness, asymmetry, and peakiness on the adhesion and friction coefficients under low external normal forces. It was found experimentally and analytically that as the surface roughness, asymmetry, and peakiness of the contacting surfaces increased, the coefficient of friction and pull of force were reduced by an order of magnitude.

1.6.3 Surface Texturing in Metal Forming

Rivin [59] proved that surface texturing also increased the static contact pressure, so this surface modification approach could effectively increase the stiffness of tool fixtures. In stainless steel sheet forming, the study of Wiklund et al. [60] showed a linear relationship between the surface roughness of the blank and the coefficient of friction.

Geiger, et al. [61-62] were the first to consider laser texturing on the tool and its relevance to micro-lubrication. They found in strip drawing that the texture shape and depth had an impact on the friction. Recently, Costa and Hutching [3] used surface texturing to texture the inserts of strip drawing dies as shown in Figure 1-9.

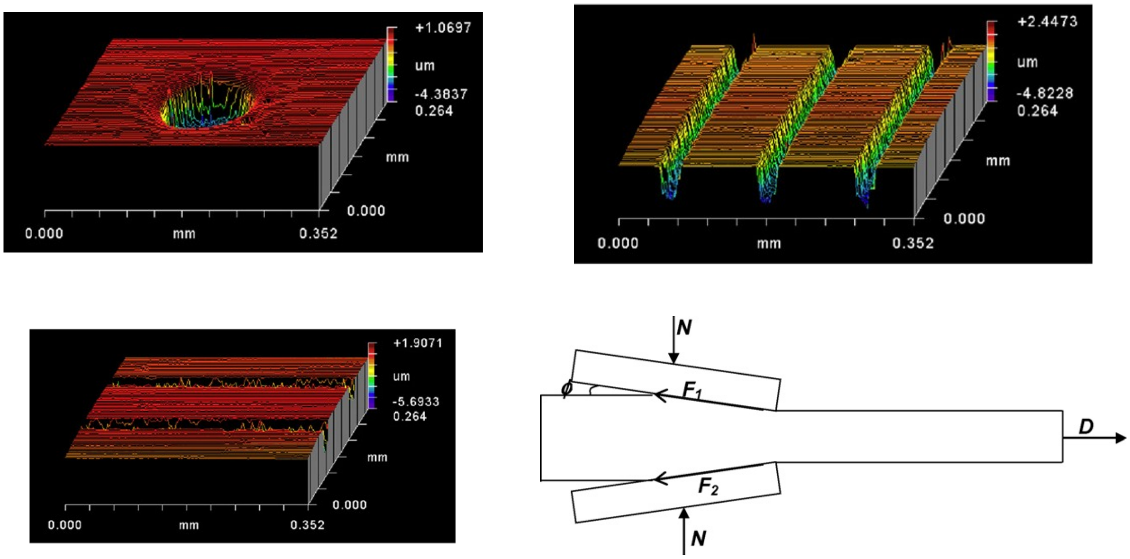

Figure 1-9: Textured Inserts of Wire Drawing Dies [3]

1.7 Summary

Based on the above mentioned literature, micro surface texturing has proven to be an effective means of enhancing tribological performance. Most of the studies investigated the effects of micro surface texturing in wet conditions with a very limited number of studies tackling the dry sliding condition. Most of the studies showed the potential benefits of adding micro surface texturing to one surface only of the contact pair in different sliding conditions. Moreover, micro surface texturing plays different roles based on the lubrication regime. In full (hydrodynamic) lubrication mode, the dimples develop pressure differences, thus they act as bearings. In the boundary lubrication mode, the texture pores provide a continuous lubricant supply to the contact interface, which decreases surface to surface contact. In the dry condition, they act as traps for wear debris so that plowing decreases.

It is obvious that the identification of significant texture parameters is inconsistent, and the minimum texture parameters widely vary for all wet and dry conditions. Etsion [2] stated that most studies done in the dry condition were based on trial and error, since there is no clear theoretical foundation that explains the mechanisms involved in dry sliding. Therefore, finding optimum texture parameters that reduce friction is very challenging.

In this study, the friction of the dry sliding contact is addressed, and the effect of surface texture on dry friction is explored. In addition, the most significant texture parameters of the dry sliding contact are sought.

1.8 Research Objectives and Approach

In this thesis, the control of the friction of dry sliding contact through micro surface texturing is the main objective. To accomplish this objective, a thorough analysis of the mechanisms involved in dry sliding conditions is made. Then, the most significant surface texture parameters that control the coefficients of friction are identified. Finally, the optimal range of the significant surface texture parameters that minimize friction is sought.

First, an analytical proof is derived which shows that there is a certain real area of contact at which the friction force is at a minimum. Second, 2-D numerical textured plane strain finite elements models are developed in order to investigate texturing parameters that significantly contribute to the frictional forces, and eventually the friction coefficient, to prove that a minimum overall coefficient of friction exists. In these 2-D models, fractal geometry is employed to model the actual rough textured surfaces, and get the closest comparison to the real surface, so that accurate clues are obtained. Then, 3-D finite elements models of various textured surfaces in contact with a rigid spherical indenter are developed. The effects of different texture parameters, such as texture size, density, shape, and anisotropy on coefficient of friction are addressed, and the most significant surface texture parameters at which the coefficient of friction is minimum are determined. Actual textured samples of air hardened tool steel are then fabricated using two methods, laser ablation and photolithography. The coefficients of friction and pull off force are measured using a scratch tester and atomic force microscope, respectively. Finally, the outputs of the numerical analyses are benchmarked to the experimental outcomes, and the micro surface texturing parameters at which the coefficient of friction is minimum are verified.

1.9 Dissertation Outline

Chapter 1 first introduces the problem of friction and reviews the effect of surface texturing on friction. It then presents the motivation and significance of this research. Finally it describes the objectives and the approaches followed to accomplish the objectives.

Chapter 2 reviews the friction mechanisms involved in dry contact, and it presents an analytical proof that shows that a minimum friction force exists at a certain range of real contact area.

Chapter 3 presents numerical 2D plane strain finite elements models to envisage the effect of different texturing parameters on the coefficient of friction.

In addition, 3D numerical models that extensively examine the effects of all the texture parameters under dry normal sliding contact on the coefficient of friction components are developed.

Chapter 4 shows the effects of the circular texturing, which are fabricated by the laser ablation technique, on coefficients of friction.

Chapter 5 presents the effect of hexagonal patterns, which fabricated by photolithography, on the coefficients of friction.

Chapter 6 addresses in detail the effects of surface texturing on the adhesion force.

Chapter 7 highlights the conclusions arising from the current study.

Chapter 2 THEORY AND ANALYTICAL APPROACH

In this chapter, the friction mechanisms of the dry static and sliding contacts are reviewed, and an analytical proof also derived to show that a minimum friction force can be obtained through optimizing the real area of contact. Hence, the surface texturing parameters are designed accordingly.

2.1 Dry Friction Mechanisms

In 1942, Bowden et al. [63-65] made a micro-examination of the sliding surfaces under the dry condition, and they suggested that the friction forces between two clean contacting surfaces were made up of two components. The first force component is the force required to shear the junctions formed between the surfaces when they were brought into contact. The second was the plowing force that was responsible for displacing the softer material from the path of the harder material, or in other words, the force that was responsible for the plastic flow or the plastic deformation [63-66]. Persson [67] defined the coefficient of friction as a ratio between the shear strength of the softer material and the flow pressure, which was defined as a pressure that required initiating the plastic flow under compressive stress.

The last finding agreed with the second law of friction by Amonton, which stated that friction force is independent of the apparent area of the sliding bodies. Figure 2-1 clarifies the difference between the apparent or nominal area of contact and the real area of contact, which is a very small fraction of the nominal area.

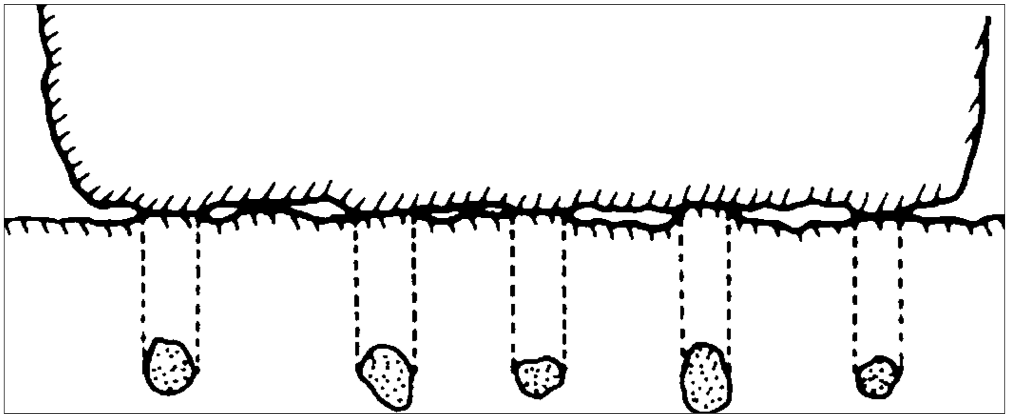

Figure 2-1: Real Area of Contact vs. the Apparent Area of Contact [67]

The friction force depends on the real area of contact, and it is equal to the shear strength of the formed junctions integrated over the real area of contact [67]. Bowden and Tabor [63-65] assumed that the two mechanisms that are involved in dry sliding are independent; therefore, the two resulting forces can be added together as in Equation 2.1 [68].

$$F_{Friction} = F_{adh} + F_{def} \tag{2.1}$$

Where $F_{Friction}$ is the total frictional force resulting from sliding, F_{adh} is the frictional force component resulting from shearing the adhesive junctions, and F_{def} is the frictional force responsible for the mechanical deformation which occurs at the contacting spots as shown in Figure 2-2.

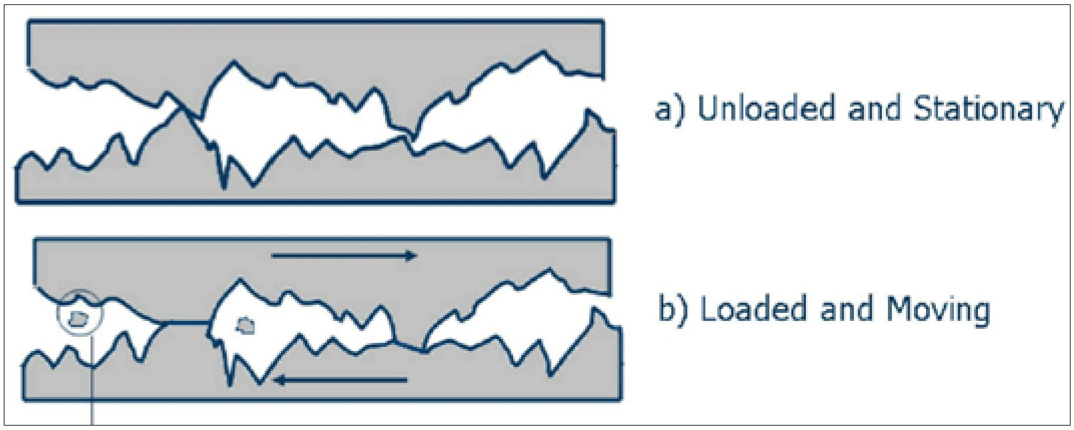

Figure 2-2: The Contact of Two Sliding Surfaces Relative to Each Other[69]

Bowden and Tabor as cited by Bhushan in [[68] related the frictional force to the interfacial shear strength and the real area of contact as shown in Equation 2.2.

$$F_{friction} = A_r \tau_a \tag{2.2}$$

The interfacial shear strength is assumed to be the bulk shear strength of the softer material, and if the interfacial shear strength exceeds this, it means that the contact asperities of the softer material fracture.

Bhushan et al. [68] rearticulated Tabor and Bowden's theory of junction growth, and defined a third type of frictional force called plowing (ploughing). They stated that when two solid surfaces are brought into contact, junctions are formed between the two surfaces due to the proximity of the two surfaces. Only fractions of the nominal area are in actual contact, and those fractions are called the real area of contact. If the two surfaces in contact start to slide relative to each other, two types of frictional forces appear. These are forces required for shearing or overcoming the junctions which are formed at discrete spots, and forces required for the micro scale deformation which occurs locally at the contacting spots. The former force is called the adhesion force, while the latter force is called the mechanical deformation force. An additional type of force might appear if one of the surfaces is harder than the other. This force is called the plowing force, which results from plowing the harder material through the softer material causing macro scale plastic deformation or grooving.

Tabor [70] highlighted three elements that are involved in the friction of the dry sliding contact. They are the true area of contact between the mating surfaces, the type and the strength of the bonds formed at the interface, and the way in which the materials in and around the contacting spots are sheared or ruptured during sliding.

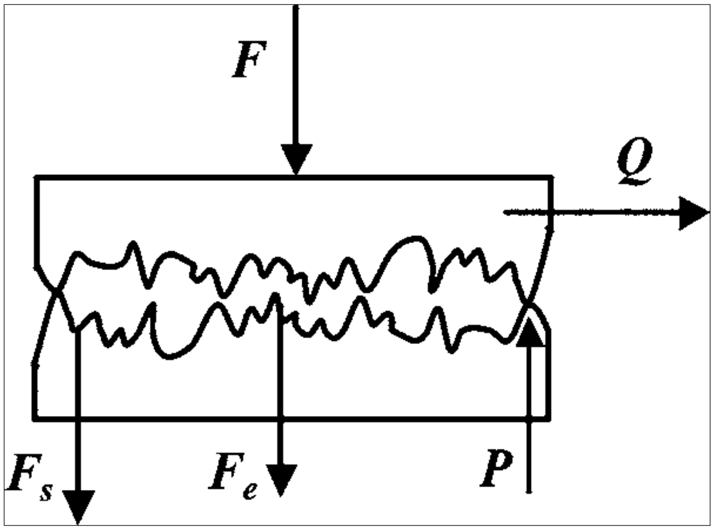

Figure 2-3: The Surface Forces of the Chang et al. Model[71]

Based on Tabor's definition, Chang et al. [71-72] introduced an analytical model that defined the static coefficient of friction μ, based on the conservation of volume as follows:

$$\mu = \frac{Q_{max}}{F} = \frac{Q_{max}}{P - F_s} \tag{2.3}$$

Where Q_{max} is the maximum tangential force needed to shear the formed junctions at the interface, and F is the normal external force that includes the balance of the actual contact load P, and the intermolecular forces, F_s. The actual contact load, P is related to the real area of contact and the material properties, therefore it determines the deformation mode of the contact, whether it is elastic, elastic-plastic, or fully plastic. The adhesion force F_s depends on the type of bonds formed and the real area of contact. Chang et al. [72] used a statistical representation of the rough surface and calculated the required static frictional force to shear all junctions between contacting asperities, taking into the account the asperities of normal preloading. The shortcoming of this model is considering the static friction force as a plastic yield failure mechanism. This means that the junctions fail at the onset of the first yield point, ignoring the ability of the elastic-plastic deformed asperities to withstand additional loading before failure. Kogut and Etsion [73-74] overcame this limitation by modeling the elastic-plastic deformation mode numerically, and demonstrated that the contacting asperities could carry additional loading after the first yielding before they fractured.

Nosonovsky and Bhutan et al. [31, 75-77] introduced the concept of the multi-scale modeling of dry friction, which was inspired by biology. In this multi-scale model, friction, in micro and nano scales, was considered and described as a complex phenomenon and a simultaneous set of dissipative mechanisms at different hierarchies and scale levels. These mechanisms can still be characterized by a single parameter, which is the friction coefficient. The coefficient of friction was classified based on the involved mechanism, whether it is due to adhesion, mechanical deformation, or plowing. It was also classified based on the deformation mode, either elastic or plastic [68] classified the deformation which occurred in the mating surfaces based on the scale of interaction. The microscopic interaction involved either elastic or plastic deformation that was characterized by the displacement of interlocking surface asperities, while macroscopic interaction included plow (plough) grooves in the softer material by the harder material or by wear debris through plastic deformation. Nevertheless, it was stressed that all frictional components in all length scales and deformation modes depended on the real area of contact and the shear strength during sliding contact.

Based on the previous review, a couple of conclusions can be drawn. First, there are two components of friction, one component is due to intermolecular forces and another component is due to mechanical deformation. Second, both components depend on the real area of contact.

In the subsequent sections, a brief description of both components of the friction that were used in this study is presented, then an analytical model proves how to minimize the frictional forces through optimizing the real area of contact.

2.2 Adhesion Component of the Friction Force

The adhesion component of friction results from overcoming the junctions which are formed due to the surface forces. Many researchers have investigated the factors that influence adhesion on friction force. Bhushan [68-69] highlighted that the adhesion force is affected by real area of contact which is a function of the normal load, surface roughness and mechanical properties. McFarlane and Tabor [78-79] defined the relationship between the surface topography, material properties, the real area of contact and adhesion as a result. Materials with higher roughness, high modulus of elasticity, higher hardness, and lower ductility exhibit lower real area of contact which results in lower adhesion. Besides, the normal and tangential loading increase the real area of contact due to the increase in the plastic flow. In addition, the real area of contact increases as a result of the interatomic attraction, such as van der Waals bonds [80-81].

There are two types of interactions between molecules that could contribute to the adhesion at the intimate contact surfaces: either physical or chemical in nature. Physical interaction involves van der Waals bonds while the chemical interactions involve covalent bonds, ionic bond or electrostatic bonds, metallic bond and hydrogen bonds [68].

When solids with covalent bonds are brought into contact, a substantial amount of energy is required to activate the bonds on the free surfaces. In addition, most covalent solids have a very high modulus of elasticity and high hardness; therefore, it is not possible to get a large area in contact even if a high load is applied. For ionic or electrostatic bonds, they are significantly based on the separation distance between the mating surfaces. If the separation distance between two ionic materials is less than or equal to atomic spacing, the bonds resemble that within the bulk materials. Whereas for separations larger than the atomic dimensions, the bond appears electrically neutral and the net Coulombs force is very small compared to van der Waals bonds. If two ionic surfaces slide over each other, this increases the fraction of the surface area charged, and consequently increases the electrostatic force. This is commonly called the "triboelectric" effect.

When two clean metals come together with a separation equals to the atomic distance, metallic bonds are formed along with short range repulsive forces which results in final equilibrium between the two metals. The metallic bonds are usually affected by the degree of cleanliness, surface roughness, the material ductility, crystallographic planes, and atomic structure.

The higher the surface cleanliness, the higher the adhesion force due to metallic bonds is. Nevertheless, the surface roughness has an opposite effect.

The ductility of the metal plays a crucial role on the adhesion force due to the increase of the plastic deformation which results in increase of the contact area.

In general, similar metals with non hexagonal structures, such as iron, exhibit high adhesion forces when they are brought in contact. In addition, the metals with polycrystalline structure show higher adhesion forces when they are brought in contact with themselves than single crystal metals in contact with themselves. This highlights the effect of the grain boundary energies [68].

The previously mentioned bonds are relatively strong primary bonds while van der Waals forces are weak secondary bonds. Van der Waals forces encompass three forces from different origins. The dominant type is called dispersion or London force, and it is due to instantaneous dipole moments of all atoms and molecules. In general, electrons around the nucleus oscillate, generating a fluctuating dipole field. This field interacts with the nearby atoms, inducing a substantial instantaneous dipole moments in them which are always attractive. This force exists between all materials since all atoms have oscillating electrons.

The second type is referred to as Keesom force, which results from attraction between rotating permanent dipoles. The third type is known as Debye force, and it originates from interaction between rotating permanent dipoles and polarizability of all atoms and molecules [82].

Much effort has been devoted to estimate the adhesion forces in the light of contact mechanics. The work of adhesion is defined as the energy per unit area required to separate two surfaces in contact while the adhesion force is the force needed to separate two bodies. On the other hand, in the force-displacement curve analysis, the maximum negative force upon the separation of tip and the sample is known as the pull-off force.

The first mathematical approximation of the adhesion force between two arbitrary undeformable spheres of radii , r_1 and r_2 , was provided in 1934 by Derjaguin, and it is equal to :

$$F_{adh} = 2\pi \frac{r_1 . r_2}{r_1 + r_2} W_a \tag{2.4}$$

Where W_a is the work of adhesion

The work of adhesion is a function of the distance (a) between the two surfaces which are brought in contact. This distance (a) is a function of surface curvature, mechanical properties, external load, and surface forces.

The JKR model was developed by Johnson, Kendall, and Robert [83], and it is based on Hertz contact problem. This model predicted larger contact area than Hertz model, and assumed that the adhesion forces existed inside the contact area only. The contact radius was estimated in the absence of the external load as follows:

$$R_{contact} = 2 \sqrt[3]{E^* W_a \left(\frac{r_1 . r_2}{r_1 + r_2}\right)^2} \tag{2.5}$$

Where E* is the equivalent elasticity modulus of the two surfaces.

And the adhesion force was defined as

$$F_{adh} = \frac{3}{2}\pi \left(\frac{r_1 . r_2}{r_1 + r_2}\right) W_a \tag{2.6}$$

From equations (2.5) and (2.6), it can be understood that the adhesion force increases non linearly with the increase of the contact radius.

Derjaguin, Muller, and Toporov [84] followed the same approach of the JKR but they assumed that the adhesion force acts outside the contact area, and can cause local deformation. They estimated the adhesion force as in equation (2.4), which increases non linearly with the increase of the contact area as with JRK model.

Bowden et al. [66] also defined the adhesion in the light of contact mechanics. The adhesion force was considered as one of the components of friction force between two clean metallic surfaces, and it was identified as a force required to shear the junctions formed between the surfaces in contact. Later, Tabor [85] investigated the idea of junction growth and how combined stresses and area of contact might affect the junction growth and the resulting adhesion force. Furthermore, Tabor [86] emphasized the importance of integrating the concept of surface energy with the contact mechanics, and he calculated the adhesion force between a sphere and a flat object in terms of their surface energies. Johnson [87] attempted to investigate the adhesion and friction forces between a smooth spherical asperity and a plane surface using the fracture mechanics approach. In this approach, the rate of release of the elastic strain energy is equated to the work done against both friction and adhesion forces.

2.3 Mechanical Deformation Component of Friction Force

The mechanical deformation component of the friction that occurs during sliding is influenced by the surface roughness, real area of contact, surface contamination (including wear debris), and the mechanical properties of the materials in contact, such as yield strength, hardness, and modulus of elasticity. The deformation component is proportional to the surface roughness and the hardness of the materials, and it is inversely proportional to the contact area and the surface contamination. In sliding contact, adhesion and mechanical deformation are always present, yet the plowing component might or might not be present depending on surface roughness, relative hardness of the materials involved in the contact, the characteristics of the wear debris, or the contaminating particles in between the sliding surfaces.

2.4 Micro Surface Patterning as an Effective Means for Controlling Friction

From the previous discussion, it is obvious that the real area of contact is a crucial parameter that controls both components of the frictional force. Therefore, engineering the real area of contact via surface patterning at a micro-scale, which is the scale of the asperities in most engineered surfaces, is a promising approach to control friction. In the following section, an analytical approach is derived that proves that there is a certain micro contact area at which the overall frictional force could be at a minimum.

2.5 Analytical Proof that Friction Force Has a Minimum Value

Material properties and the real area of contact of two surfaces sliding relative to each other are the major factors that govern the friction behaviour at the interface. Therefore, it can be assumed that if friction forces due to adhesion and mechanical deformation are plotted against the real area of contact, the following is observed. As the area of contact increases, the frictional force due to the adhesion component increases asymptotically, while the mechanical deformation component of the frictional force decreases. Assuming that both components are independent, if the equations of the two curves are added, the overall frictional force (red dotted curve) is obtained as shown in Figure 2-4. This overall curve should have a certain area at which the resulting overall frictional force is at a minimum. This results from the fact that the mechanical deformation gets extremely high as the real area of contact approaches zero, while the adhesional friction gets smaller, so the overall frictional force is a decreasing function at a small area of contact as shown in region (I) of Figure 2-4. Whereas, the mechanical deformation decreases as the contact area goes to ∞, the adhesion component increases. Therefore, the overall frictional force is an increasing function when the real area of contact is large as shown in region (III) of Figure 2-4. A minimum overall friction force at a certain value of a real area of contact should exist, and it should be located somewhere in region (II) that is shown in Figure 2-4.

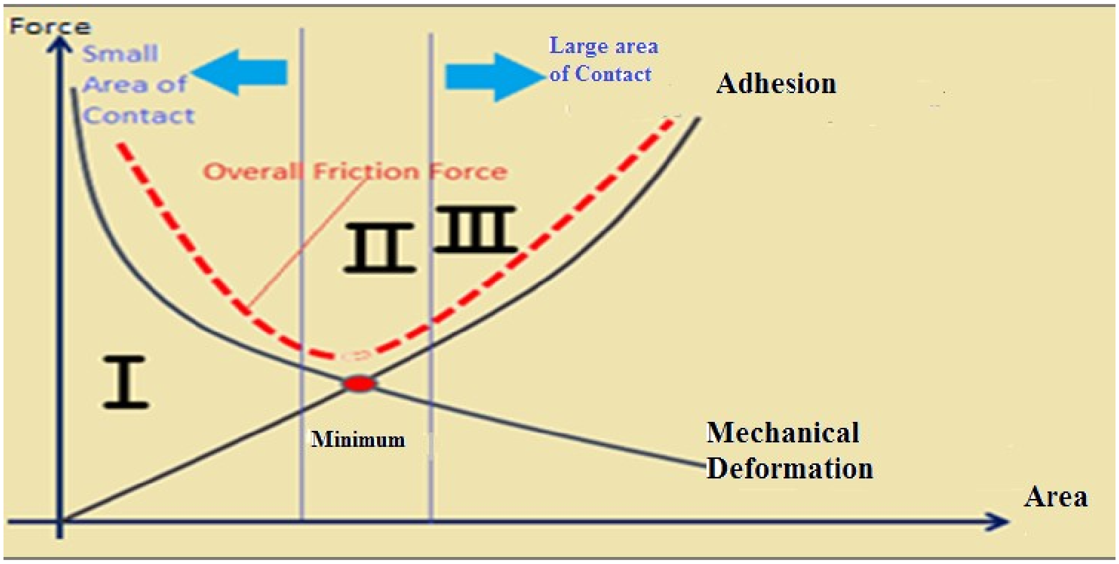

Figure 2-4: The Friction Force Components vs. the Contact Area

In order to prove that a minimum overall coefficient of friction exists, the derivative of the overall frictional force in Equation 2.1 should exist, and should be zero.

Where F_{adh} is the friction force which results from adhesion, F_{def} is the friction force which results from the mechanical deformation, and both are a function of the real contact area A.

$$F_{adh} = f_1\,(A_r) \tag{2.7}$$

$$F_{def} = f_2\,(A_r) \tag{2.8}$$

The adhesion force increases as the real contact area A increases.

$$for\ A_1 < A_2,$$

$$f_1(A_1) < f_1(A_2) \tag{2.9}$$

On the other hand, the mechanical deformation is inversely proportional to the contact area A,

$$f_2(A_1) > f_2(A_2) \tag{2.10}$$

Therefore, a minimum frictional force can be achieved at a specific contact area A_r, if

$$\frac{\partial F_{friction}}{\partial A_r} = 0 \tag{2.11}$$

Or

$$\frac{\partial F_{friction}}{\partial A_r} = \frac{\partial f_1}{\partial A_r} + \frac{\partial f_2}{\partial A_r} = 0 \tag{2.12}$$

Equation (2.12) is trivially satisfied if

$$\frac{\partial f_1}{\partial A_r} = \frac{\partial f_2}{\partial A_r} = 0 \tag{2.13}$$

That corresponds to the theoretical minimum adhesion and mechanical deformation. However, a more realistic result is obtained from the case of

$$\frac{\partial f_1}{\partial A_r} \neq 0 \text{ and } \frac{\partial f_2}{\partial A_r} \neq 0 \tag{2.14}$$

But

$$\frac{\partial f_1}{\partial A_r} > 0 \; (\, follows\; from\; eq. 2.9 \,) \tag{2.15}$$

$$\frac{\partial f_2}{\partial A_r} < 0 \; (\, follows\; from\; eq. 2.10) \tag{2.16}$$

Therefore, there is a non-zero contact area A at which the friction is at a minimum. This contact area is given by the non-trivial solution of Equation 2.12.

2.6 Conclusion of Dry Friction Mechanisms

In this chapter, different models that tackle the friction mechanisms under dry conditions were presented. It was agreed that the real area of contact is one of the significant parameters that controls the friction coefficient; therefore, if it is optimized, the coefficient of friction can be minimized. The optimization of the real area of contact can be realized by micro surface texturing the highly polished surfaces. An analytical proof shows that there is a certain real area of contact at which the overall frictional force is at a minimum. In the coming chapters, this minimum range of the real area of contact will be determined numerically and experimentally.

Chapter 3 NUMERICAL SIMULATIONS FOR TEXTURED SURFACES

Numerical simulations using the finite element method are considered to be one of the most powerful approaches for the prediction of the tribological behaviour, because they are both time and cost efficient. In addition, they can be used as predictive tools to explore new designs, understand the involved friction mechanisms, and identify and optimize the critical parameters. In this chapter, a review of the numerical simulations which tackled the contact of two sliding surfaces is presented, followed by initial 2D plane strain finite element models that simulate the contact between a rigid surface and engineered textured surfaces. Fractal geometry is used to properly simulate the topographies of the engineered surfaces in the 2D finite element models. Finally, 3D finite element models are developed to simulate the contact between a rigid spherical indenter and elastic, fully-plastic textured surfaces. These models investigate the effects of the pattern geometry, density, and shape on the friction coefficients.

3.1 Background of the Analytical and Numerical Contact Models

Many analytical models that investigate the contact between two surfaces are derived from the basic Hertz model [88] which is limited to the elastic contact between two smooth spheres. However, real engineered surfaces undergo different deformation modes; furthermore, they are rough and not smooth.

Therefore, the Hertz model usually gives misleading results for the contact properties. Many studies have been undertaken to investigate the surface interactions during normal loading and sliding extended beyond the limitations of the Hertz model. Greenwood and Williamson [89] developed a model which calculated the contact properties, such as contact pressure and real area of contact between two nominally flat surfaces. This model has been known as GW model. Greenwood and Tripp [90] modified the basic GW model by exploring the properties of the contact between two flat rough surfaces instead of smooth surfaces. Many analytical models [72, 91-97] were based on the Greenwood and Tripp model [90], and incorporated more realistic surface properties. However, those analytical models are computationally complex and involve many approximations and assumptions.

With the advancement of computational capabilities, various numerical analyses have investigated the contact behaviour between a rigid surface and elastic, elastic-plastic, or fully plastic surfaces.

Tangena and Wijnhoven [98] developed 2D finite element models to describe the interaction of a hard asperity when it slides over an elastic-plastic soft asperity. The vertical separation was kept constant as the normal force, while shear force, and the coefficient of friction were calculated for different separation distances. The adhesion friction was introduced between the two asperities in this model. It was shown that although the adhesion friction raised the shear force and the friction coefficient, it did not affect the normal force.

Faulkner and Arnell [99-100] incorporated the results of the 3D finite element model of two elastoplastic hemispherical asperities into a statistical model that was used to predict the effects of the surface roughness on the overall friction coefficient.

Jackson and Green [101] presented a normalized 2D axi- symmetric finite element model of an elastic fully-plastic hemisphere in contact with a rigid flat surface. A precise form for the critical interference at which the plastic deformation was initiated was determined based on the von Mises yield criterion.

The surface topography and surface texture have a crucial influence on the friction and tribological performance in general. The modeling of the surface texture was first introduced by modelling the textured layered media in contact with a rigid indenter that simulated the contact between the head and the magnetic hard disk. Komvopoulos [102-103] used the finite element method to investigate the normal contact between a rigid surface and a layered medium, while Tian and Saka [24] studied the sliding contact between rigid surfaces and a two-layer elastic-plastic half space. Later, Kral and Komvopoulos [104-105] elucidated the combined effect of indentation and sliding on the three dimensional finite element layered elastic-plastic half space to determine the surface and subsurface stresses and strain fields. Ye and Komvopoulos [106] studied the effect of residual stresses in the surface layer on contact deformation of layered media. It was concluded that the residual stress in the surface layer depended on the type of contact, indentation or sliding, coefficient of friction and the dominant deformation mode in the surface layer.

Wang and Zhu [20] introduced the term of “virtual texturing” for a numerical tool that was able to determine the basic geometric features of the surface texture. Correlations were found between the lubricant film thickness, and the contact ratios with the dimples' size, density, shape, and depth.

Gong and Komvopoulous [107] developed plane strain finite element analyses for patterned layered media to investigate the effects of the pattern geometry, such as meandered and sinusoidal patterns, on-contact pressure distribution, tensile surface stresses, and subsurface equivalent plastic-strain. A rigid cylindrical asperity slid on the patterned layered media under normal loading, and a relationship for the contact pressure concentration factor was defined. The same group [108] developed a three dimensional finite element model of a rigid sphere indenter in normal and sliding contact with an elastic-plastic layered medium with equally spaced rectangular pads. The effects of patterning on the contact pressure distribution, sub-surface stress-strain fields, and thermal stresses were identified.

Ramachandra and Ovaert [109] investigated the effects of discontinuous coating on the normal pressure distributions and subsurface stress fields. Different patterned coatings were investigated including sharp edges, rounded edges, and crowned profiles. The coatings with the sharp and rounded edges exhibited normal pressure spikes, while the discontinuous coating with the crowned profile reduced or eliminated the normal pressure singularities.

With the advancement of computational capabilities and measurement devices that inspect surface topography, various models have been developed to measure the roughness of the surfaces. Roughness measurements of many engineered surfaces show that the power spectra of engineered surfaces follow power laws [110]. Such engineered surfaces are processed by turning, drilling, electrical discharge machining, grinding, and rubbing [111]. This means that when the surface sufficiently is magnified, the magnified surface looks very similar to the original surface. This property can be modeled using the concepts of self-similarity and self-affinity of fractal geometry.

Different fractal models in the literature have been used to define engineered surfaces but the most common fractal model is Weierstras - Mandelbrot (WM) functions. The two dimensional WM functions are defined as follows:

$$z(x) = G^{(D-1)} \sum_{n=1}^{\infty} \frac{\cos 2\pi\gamma^n x}{(\gamma)^{(2-D)n}} \qquad 1 < D < 2\,; \quad \gamma > 1 \tag{3.1}$$

Where G is a scaling constant, D is a fractal dimension, and γ^n is the frequency mode which is the reciprocal of the wavelength of the roughness. The fractal dimension, D measures the complexity of the repeated shape, and it has a non-integer value [112].

Komvopoulos and Ye [113] used a 3D Weierstrass-Mandelbrot (W-M) fractal function to characterize the layered interface of the hard disk. This function is continuous at all points. Sahoo and Ghosh [114] used the 3D modified W-M function to develop a parametric study to relate the contact properties such as contact area, contact displacement, and contact load with the key material properties and surface parameters. Jiang et al. [111] incorporated experimentally measured topography by the Atomic Force Microscope, and used them as inputs to determine the spatial power spectra of the profile. From the spatial power spectra, the fractal dimension was determined and the surface topography was simulated. A ground surface was used in this study as an example.

Warren et al. [115] used the deterministic fractal cantor set to model the perfectly plastic rough surface in contact with a rigid smooth indenter. A brief description of the cantor set is explained in the next section as it is used in the prediction of the optimal surface texture parameters.

It is noticed from the previous studies that the effect of the surface patterning on the coefficient of friction under dry sliding conditions has not been investigated so far. Most of the research done so far focused on the effect of the surface patterning on the contact pressure distributions and surface and sub-surface stresses and strains. In the following sections, numerical two dimensional and three dimensional models are developed to investigate the effect of surface texturing on the coefficient of friction.

3.2 Two Dimensional Models for Prediction of the Significant Texture Parameters

In this section, the effect of the surface texture geometry on the coefficient of friction is investigated. Two-dimensional plane strain finite element models are developed with different surface texturing parameters.

3.2.1 Cantor Set

The Cantor set has two scaling parameters such that the width L_{n+1} and the height h_{n+1} are given by

$$h_{n+1} = \left(\frac{1}{f_z}\right) h_n = \left(\frac{1}{f_z}\right)^{n+1} h_o \qquad (3.2)$$

$$L_{n+1} = \left(\frac{1}{f_x}\right) L_n = \left(\frac{1}{f_x}\right)^{n+1} L_o \qquad (3.3)$$

where f_x and f_z >1, and L_o and h_o are the initial width and height of the surface profile.

The Cantor set surface [115-116] which is shown in Figure 3-1 is constructed by joining the segments of the successive stages of the Cantor set. At each stage, the middle sections of the initial segments are removed so that the lengths of the remaining segments are $\frac{1}{f_x}$ multiplied by the length the initial segment. The same manner is followed in the vertical direction.

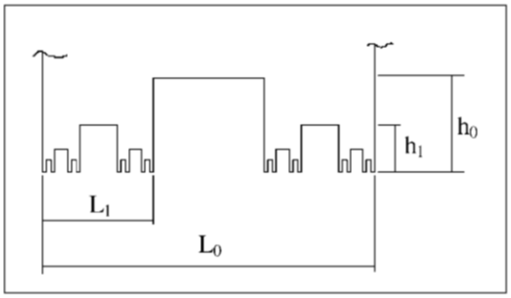

Figure 3-1: Generalized 2D Cantor set [115]

ABAQUS 6.10, a finite element code, was used to model the two-dimensional plane strain textured surface in contact with a rigid hemispherical indenter. The pattern design consists of set of rectangular pads with different widths and the same depth. A randomized three level fractal Cantor set is superimposed on the meandered surfaces to simulate the roughness of the engineered surfaces.

3.2.2 Geometry of 2D Plane Strain Models

The width of the tested sample is 100 µm, while the height is 110 µm, and the width of the individual rectangular pads varies from 5 µm to 25 µm, as shown in Figure 3-2. The spatial distance between the rectangular protruded pads is kept constant at 10 µm so that the spatial texture densities vary between 0.33 and 0.6667.

Figure 3-3 depicts the different geometries of the superimposed fractal surface in contact with a hemispherical rigid indenter of 20 µm radius. The material which is used in this study is tool steel. The modulus of elasticity is 194 GPa and the yield strength is 1950 MPa.

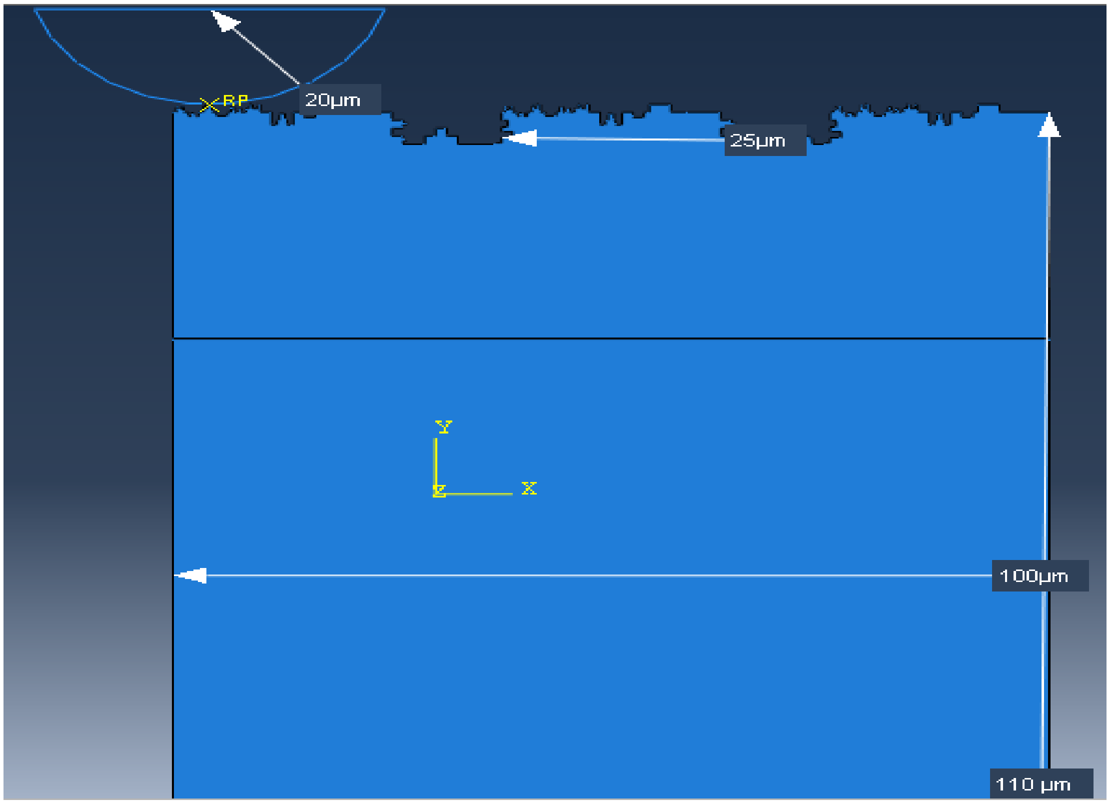

Figure 3-2: Dimensions of the 2D Fractal Model.

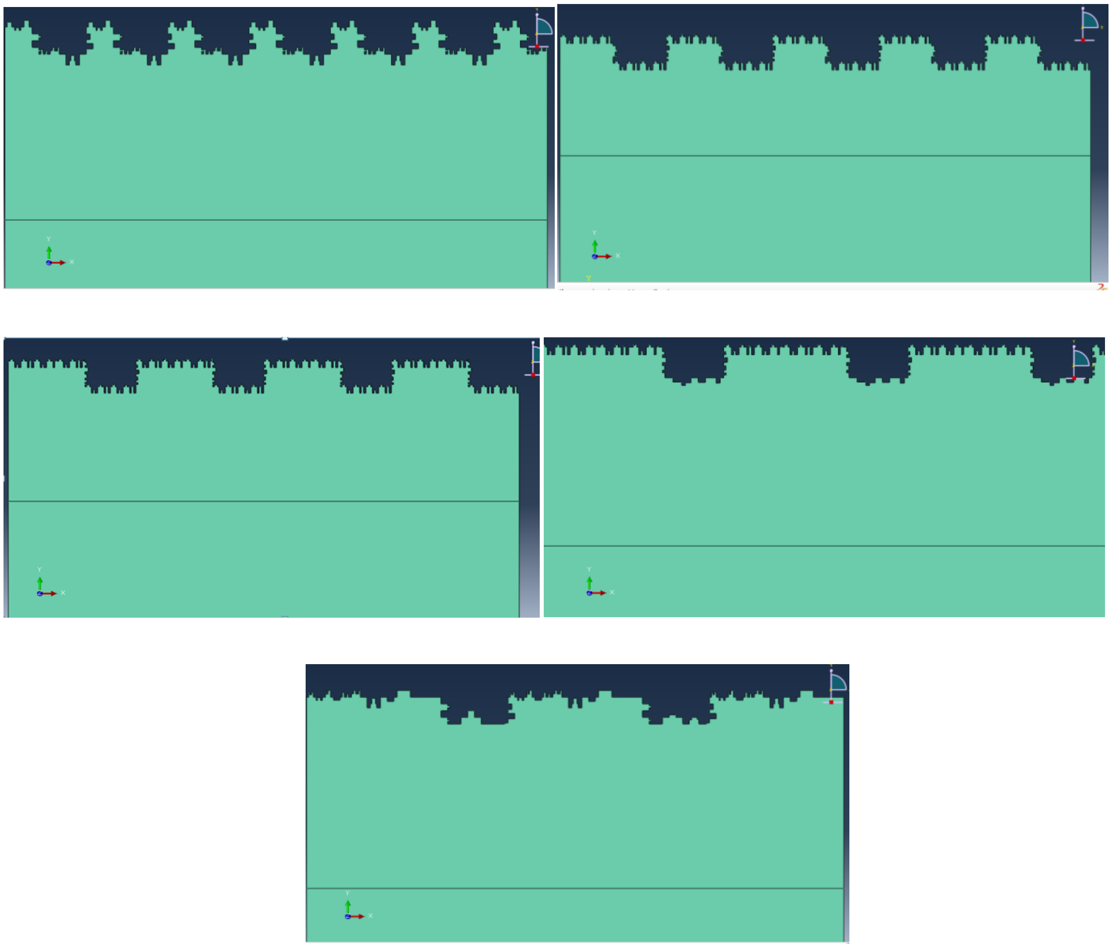

Figure 3-3: Different Surface Texturing Parameters.

3.2.3 Boundary and Loading Conditions of 2D Models

Figure 3-4 illustrates the boundary conditions and the applied loading. The bottom side is restrained from motion in the Y direction, and the left side is constrained in the X direction. The rigid indenter is constrained to rigid body motion. The indenter moves downward until it contacts the textured surface through the prescribed displacement. The rigid indenter slides in the X direction for 100 µm. The prescribed vertical displacement is selected such that the resulting stresses are less than the yield strength of the material, while the horizontal sliding distance is selected to be more than the largest wavelength of the proposed texture.

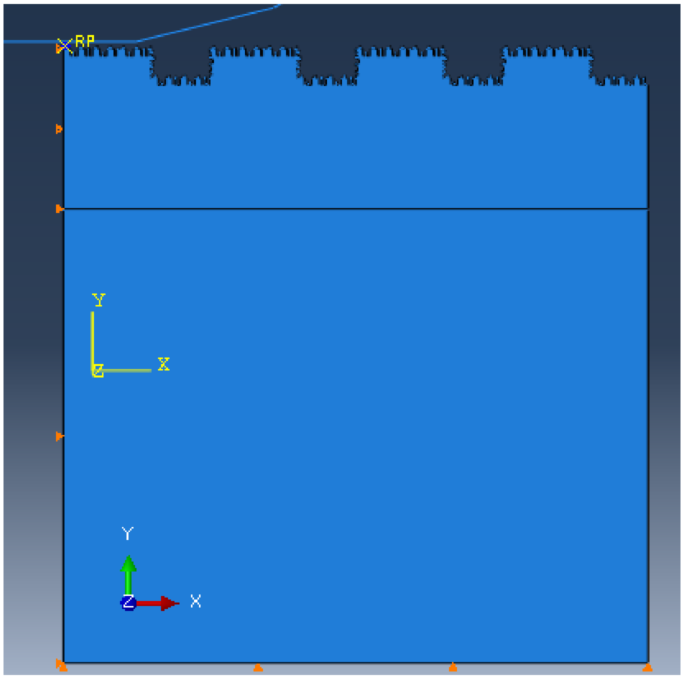

Figure 3-4: Boundary Conditions for the 2D Plain Strain Model.

3.2.4 Mesh Properties of 2D Models

Three node linear plane strain triangular elements were used to mesh the deformable textured surface as shown in Figure 3-5. The total number of nodes is around 6000, and the total number of elements is approximately 11,200. Linear rigid elements were used to mesh the rigid indenter. The mesh density increases at the contact interface in order to increase the accuracy. The size of the elements was selected to be less than a quarter of the smallest geometric length scale.

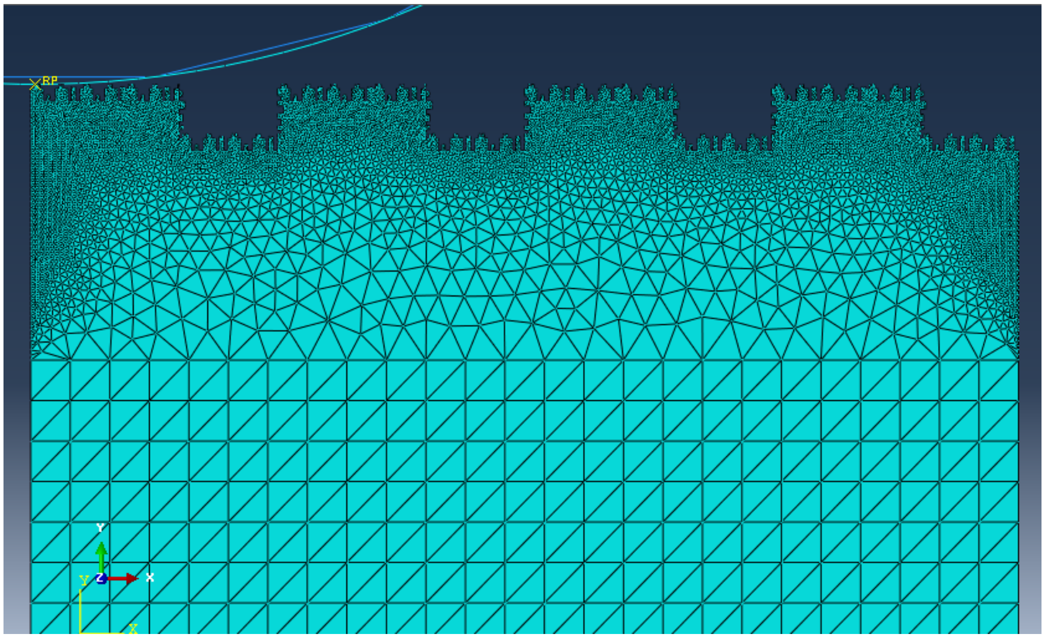

Figure 3-5: Mesh of the 2D Textured Part.

3.3 Results and Discussion of 2D Models

The two-dimensional plane strain models with different geometric texturing parameters are used to initially predict the trend of the coefficient of friction when the texturing sizes and density change.

Figure 3-6 shows that the smallest length scale asperities undergo full plastic deformation due to the small area of contacts and the resulting high stresses. On the other hand, the square pads have not reached the yield point. This observation proves that the stresses increase with the decrease of the length scale.

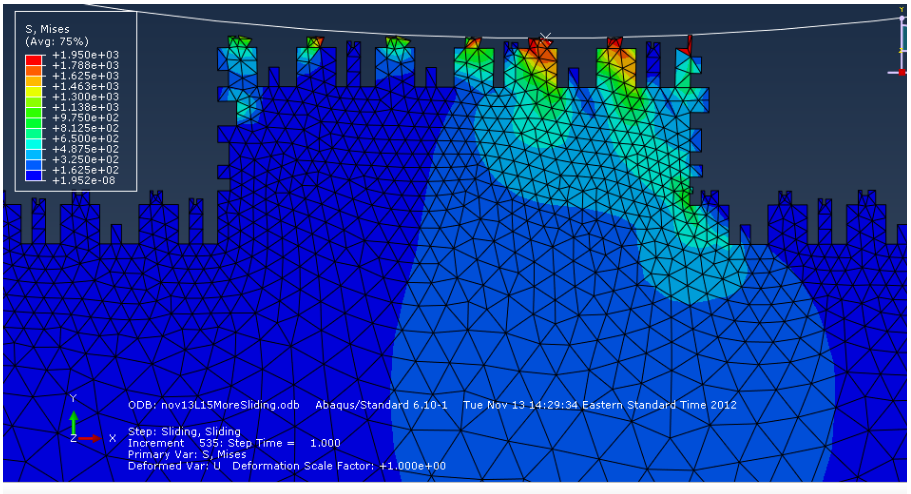

Figure 3-6: Yielding of the Smallest Asperities

There is no pronounced trend observed when the coefficient of friction is plotted vs. the width of the square pads. However, when the coefficient of friction is plotted vs. the spatial texture density (D/L), which is width of the recessed square (D) divided by the distance between the centres of the two recessed squares (L), as shown in Figure 3-7, a minimum value of the coefficient of friction is obtained. This ratio (D/L) could be called the spatial texture density. In Figure 3-8, for the spatial texture density (D/L) of 0.334, the coefficient of friction is relatively high, after that it decreases until it reaches its minimum value at (D/L) equal to 0.4. Afterwards, it increases again as the spatial texture density increases to 0.667.

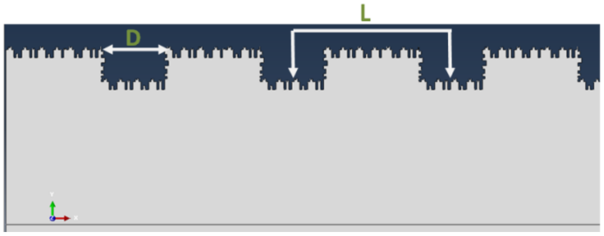

Figure 3-7: The Spatial Texture Density (D/L) for 2D Textured Model

This phenomenon could be explained by the following. When the spatial texture density is small, the real area of contact is quite large, so the adhesion component contributes to the increase of the friction coefficient. Then, as the real area of contact decreases with the increase of the spatial texture density, the adhesion component of the friction decreases as well; however, the stresses increase which result in an increase in the mechanical deformation component. Yet, at a certain spatial texture density, the overall coefficient of friction is at a minimum. From Figure 3-8, this minimum overall friction falls at a spatial texture density of 0.4.

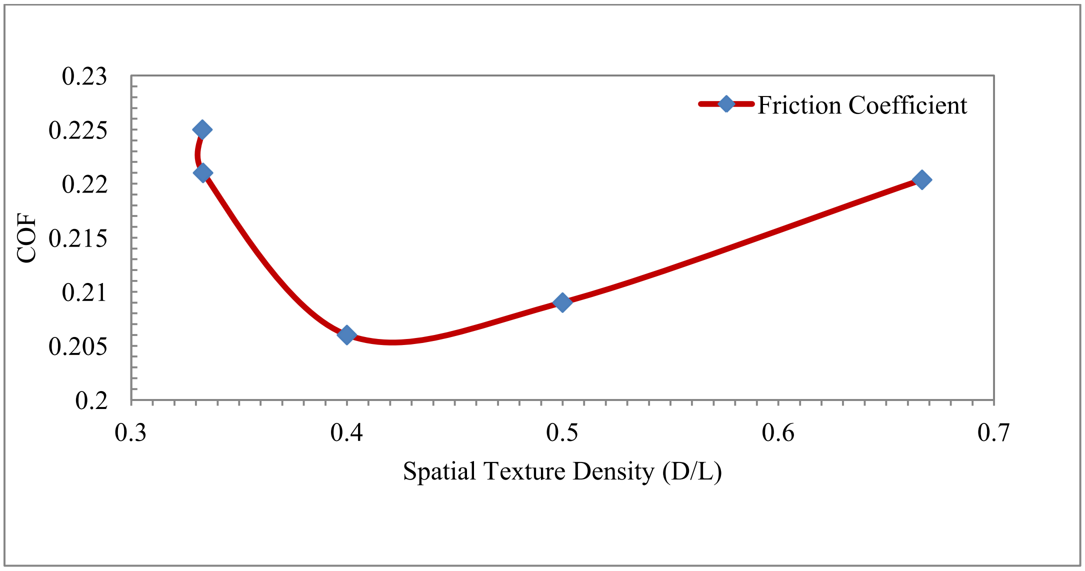

Figure 3-8: The Coefficient of Friction vs. the Spatial Texture Density (D /L)

Although the 2D plane strain models give insightful conclusions with regard to the existence of the minimum friction coefficient, which agrees with the analytical proof presented in Chapter 2, more comprehensive numerical simulations were needed to further explore the effect of different parameters of the surface texture on the friction coefficient.

In the following sections, full three-dimensional finite element models were developed to further investigate the effect of the surface texturing on the coefficient of friction components.

3.4 Three Dimensional Textured Surface Models

In the following sections, three-dimensional micro patterned elastic fully-plastic deformable parts, that are in contact with a rigid indenter, are modeled and analyzed using the multi-purpose finite element code, ABAQUS 6.10. The main purpose of these analyses is to further investigate the findings of the plane strain two-dimensional models, to find the optimal texture parameter at which the coefficient of friction is minimal, to examine the effects of the pattern shape on the friction coefficients, and finally, to check the anisotropy of the patterns. First, the model description is presented in detail, then the results of the circular patterns, followed by the results of the hexagonal patterns. Afterwards, a comparison between the outcomes of the circular and hexagonal shapes is made. Finally, the results of the pattern anisotropy are illustrated.

3.4.1 Geometry of 3D Models

The deformable part is first created as a 3D deformable extruded solid with a 315 μm length, 210 μm width, and 50 μm thickness as shown in Figure 3-9. These dimensions are chosen so that the largest proposed design is examined, and the effects of the boundary conditions are reduced or eliminated.

Patterns with different shapes and dimensions are cut in the XY plane, as shown in Figure 3-10. The depth of the pattern is constant since only the dry sliding contact is investigated, and it was selected to be 5 μm as recommended in the literature [47].

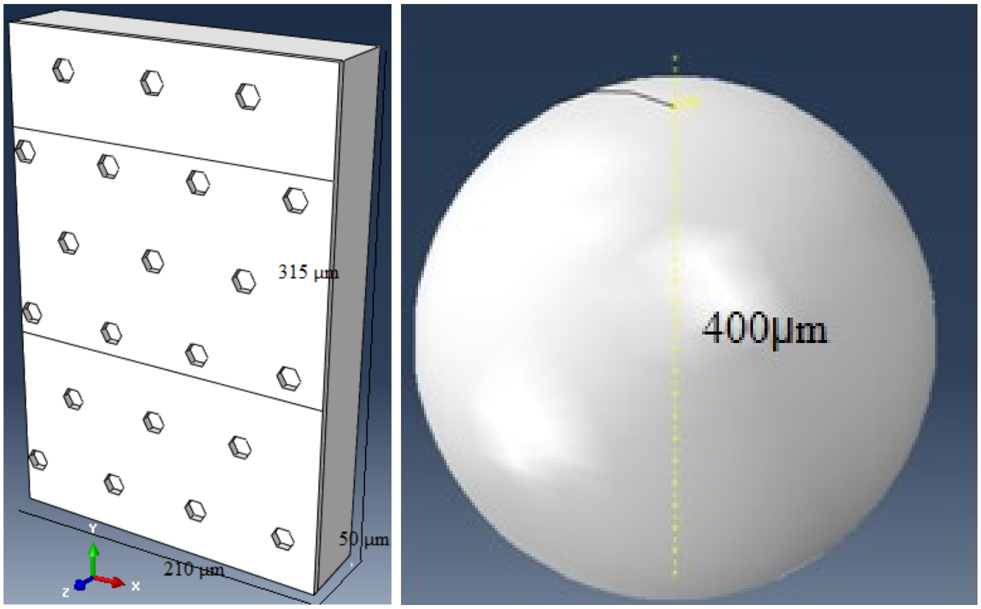

Figure 3-9: The Geometry of the Parts in Contact

The rigid indenter was modeled as a discrete rigid solid sphere with a radius of 200 μm, with a reference point assigned on the sphere surface. This specific indenter size was selected for two reasons. First, the results of the simulations are to be compared to the outcomes of the experimental work where a diamond indenter with a tip radius of 200 μm is used. Second, it is large enough to cover the largest proposed texture periodicity.

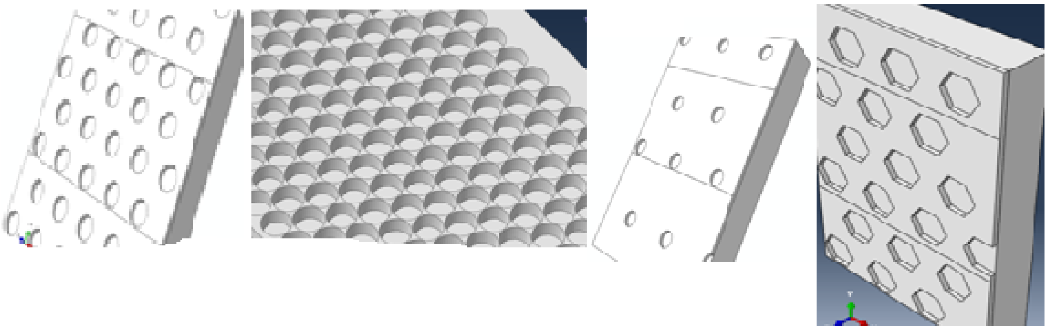

Figure 3-10: Different Texture Designs with Different Dimensions and Densities

3.4.2 Material Properties of 3D Textured Surface Models

The textured samples were made from air hardened tool steel (A2), and the mechanical properties of the tool steel are listed in Table 3-1. The deformation modes are assumed to be elastic fully-plastic without strain hardening, as shown in Figure 3-11.

Table 3-1: The Material Properties of Air Hardened Tool Steel (A2)

Young's Modulus	Yield Strength	Poisson's ratio
194 GPa	1.95 GPa	0.3

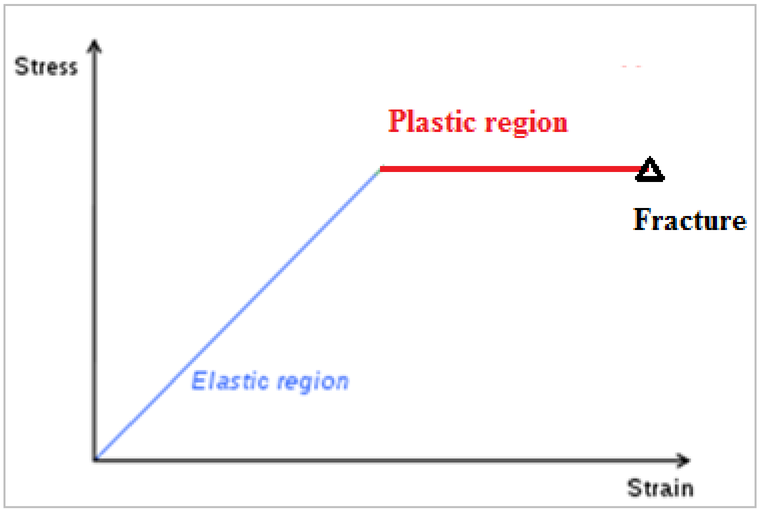

Figure 3-11: The Elastic -Fully-Plastic Deformation Model

3.4.3 Assembly and Contact Interaction of 3D Models

Three sequential general static steps, where the inertia effect is neglected, were carried out to model the dry sliding contact condition. First, is to bring the rigid indenter is brought into contact with the patterned surface. Second the indenter is slid over the patterned surface for a certain distance, which simulates the mechanical deformation. Finally, the indenter is removed from the patterned surface, which simulates the pull off force measurement. The direct full-Newton-Raphson technique was employed to solve the equations implicitly. The contact interaction was defined between the rigid indenter, which is designated as a master surface, and the patterned surface that acts as a slave surface. For the sliding formulation, the finite sliding is selected as it is more general, and allows for any arbitrary relative separation and sliding motion between the surfaces in contact [117]. The surface to surface discretization method was used as it provides more accurate pressure and stress results, since more nodes are involved per constraint. In addition, surface to surface discretization resists the penetration of the master surface into the slave surface in an average sense, which results in a smoothing effect. The basic Coulomb friction model allows the contacting surfaces to carry a certain shear stress before starting to slide relative to each other. This is known as the stick/slip condition. The transition between stick to slip or vice versa occurs when the shear stress reaches a critical value, which is a fraction of the contact pressure between the contacting surfaces, and is defined as a coefficient of friction μ.

$$\tau_{critical} = \mu P \qquad (3.3)$$

Where $\tau_{critical}$ is the critical shear stress at which the sliding starts, P is the contact pressure, and μ is the static coefficient of friction.

This frictional constraint is enforced with a certain stiffness that allows small relative motion between the contacting surfaces during the sticking state, which is known as an elastic slip. In these models, the elastic slip is determined as a small fraction that equals 0.005 of the characteristic contact surface length of the slave surface. This value is suggested in [117] as this value provides a balance between efficiency and accuracy.

3.4.4 Boundary and Loading Conditions of 3D Models

The sides and the base of the deformable textured part are completely constrained with zero degrees of freedom allowed. The top textured surface, which is in contact with the indenter, is free to deform in any direction as shown in Figure 3-12. This boundary condition is set because no constraints should be applied to the regions in contact as the contact constraints are already in effect.

For the rigid indenter, it is constrained from rotation around any of the three axes. Forced displacement in the negative Z direction is applied to bring the indenter into contact with the textured surface in the first two steps, in order to avoid the chattering between the patterned surface and the rigid indenter. The sliding distance of 200 μm was assigned along the X axis for the horizontal sliding and the negative Y axis for the vertical sliding. During the third step where the indenter is removed from the patterned surface, the displacement along the negative Z axis and sliding were prevented, so that the effect of the pull off force is simulated, and the adhesion component of the friction can be measured separately.

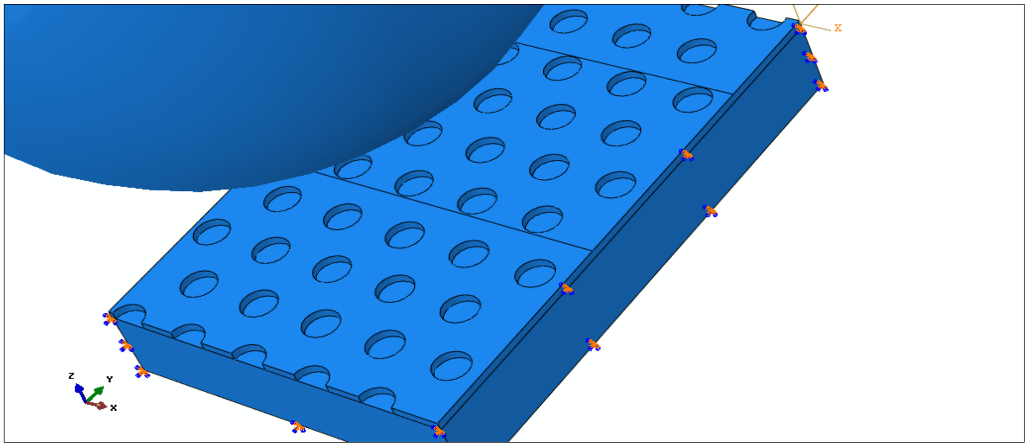

Figure 3-12: Boundary Conditions Applied to the Sides and the Bottom of the Deformable Textured Parts

3.4.5 Mesh and Mesh Sensitivity of 3D Models

Three dimensional 4-node linear tetrahedron solid elements are used to discretize the textured parts, and 4-node 3D quadrilateral rigid elements are employed for the indenter. The number of elements varies according to the texture size and the spatial texture density. The size of the elements at the contact interface is reduced in order to increase the accuracy of the results. In all simulations, the element size is at least 10 times smaller than the dimple diameter. Along the sliding path, the element size is further reduced to capture the effects of the different pattern parameters as shown in Figure 3-13.

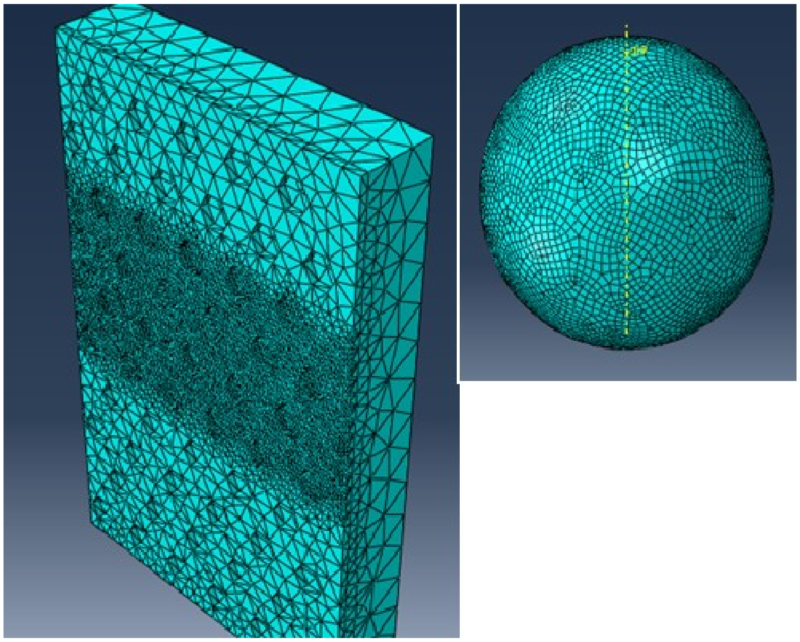

Figure 3-13: Mesh Elements for the Patterned Surface and Rigid Indenter

The mesh sensitivity was tested by increasing the mesh density two-fold and four-fold as shown in Figure 3-14, the errors were 2% and 0.5%, respectively, however, the processing times increased 4 and 10 times, respectively. Therefore, the mesh density was doubled to find a good compromise between accuracy and processing time.

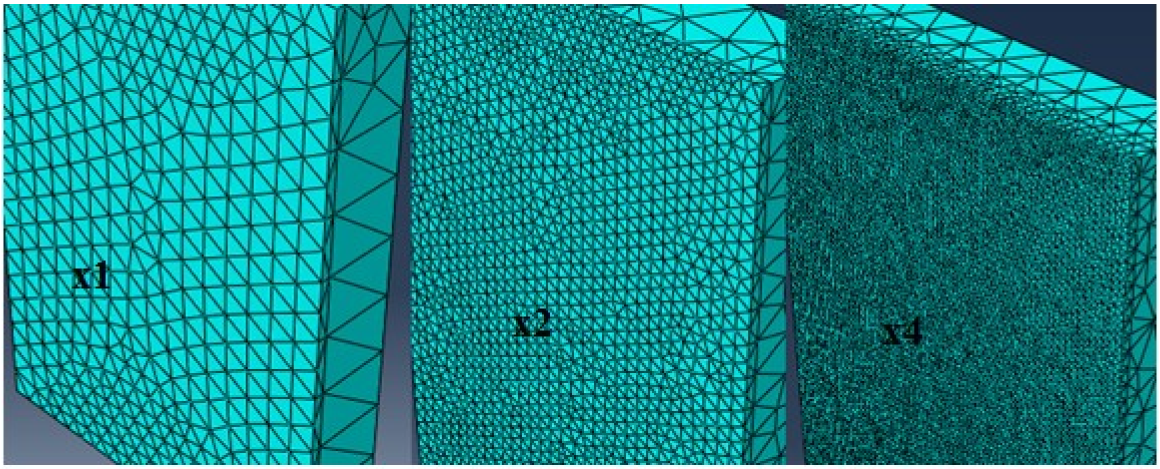

Figure 3-14: Different Mesh Densities to Check Mesh Sensitivity

3.5 Results and Discussion of 3D Models

In this section, the two friction components, adhesion and mechanical deformation, are presented separately, and a fitted curve that combines the two best fit regression curves is plotted to demonstrate the existing minimum.

First, the effect of the texture parameters, such as the texture size D, the distance between the centres of two consecutive dimples L, and the dimensionless spatial texture density (D/L) on the coefficient of friction was investigated for both circular and hexagonal dimples. Second, the effect of the texture shape was examined, and finally, the texture anisotropy is checked. The two friction coefficients were recorded in each analysis: the mechanical deformation which was recorded during the sliding step, and the adhesion component which was recorded during the third step when the indenter was removed from the patterned surface. In order to estimate each friction coefficient, the total shear force was divided by the normal force, which resulted from the prescribed displacement and the sliding distance, at the interface between the textured surface and the indenter.

3.5.1 The Numerical Models for Circular Patterns

Three spatial texture densities and combinations of three different diameter were modeled and examined. The three different spatial texture densities are 0.25, 0.5, and 1 while the three sizes of the circular dimples are 5 μm, 10 μm, and 15 μm. These texture parameters are the same as those of the sample dimensions that were experimentally fabricated and tested in order to validate the results of the finite element models. Table 3-2 lists the texture parameters for each simulation models.

Table 3-2: The Combination of the Samples' Diameters and the Spatial Texture Densities

Sample#	**1** **D5L5**	**2** **D5L10**	**3** **D5L20**	**4** **D10L10**	**5** **D10L20**	**6** **D10L40**	**7** **D20L20**	**8** **D20L40**	**9** **D20L80**
D/L	1	0.5	0.25	1	0.5	0.25	1	0.5	0.25
D(μ)	5	5	5	10	10	10	20	20	20
L(μ)	5	10	20	10	20	40	20	40	80

In Figure 3-15 through 3-17, the adhesion and mechanical deformation components for each texture dimple diameter are plotted against the dimensionless spatial texture densities (D/L). Some observations are worth mentioning. As the spatial texture density increases, the coefficient of friction due to mechanical deformation increases, while the adhesion component decreases. This is primarily due to the decrease in the contact area. Therefore, each friction component curve either increases or decreases monotonically with the spatial texture densities.

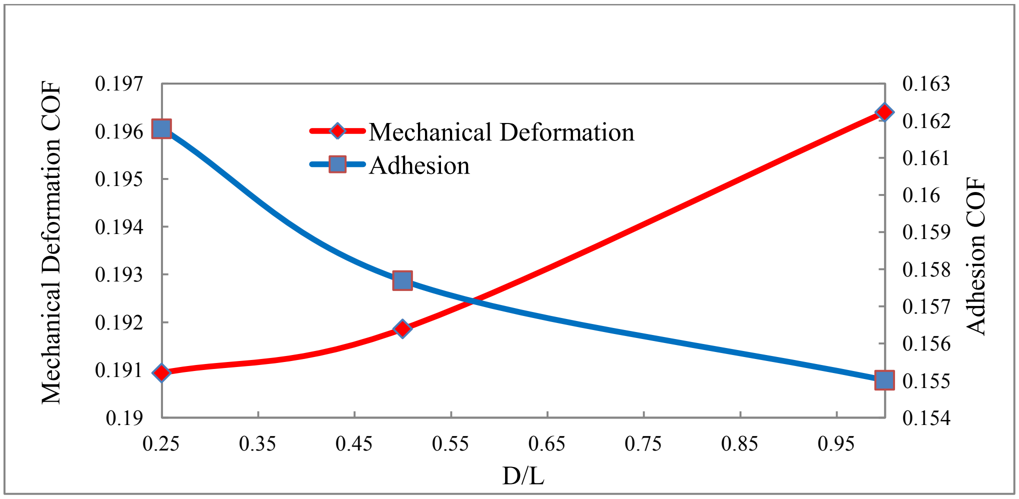

Figure 3-15: Coefficients of Friction due to Mechanical Deformation and Adhesion for the Circular Diameter of 5 μm.

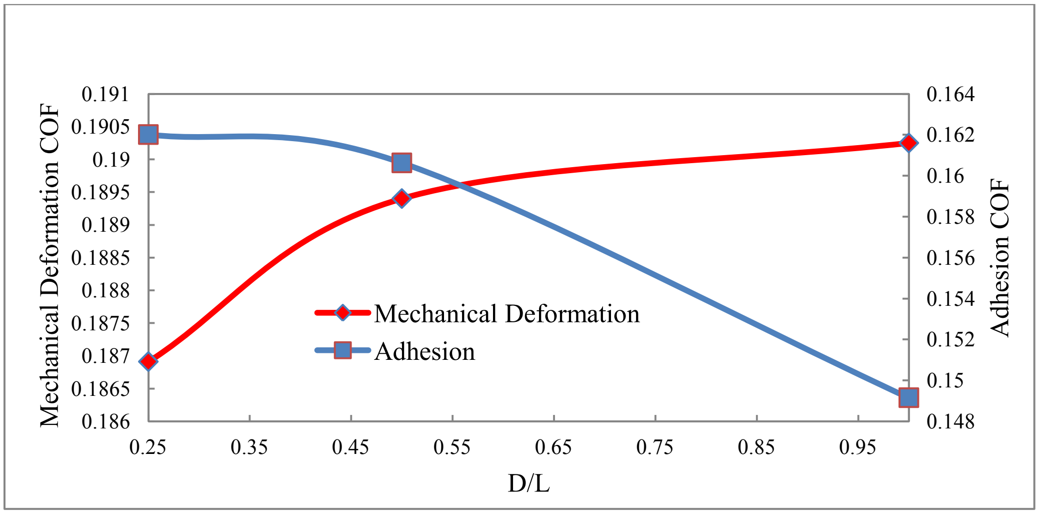

Figure 3-16: Coefficients of Friction due to Mechanical Deformation and Adhesion for the Circular Diameter of 10 μm

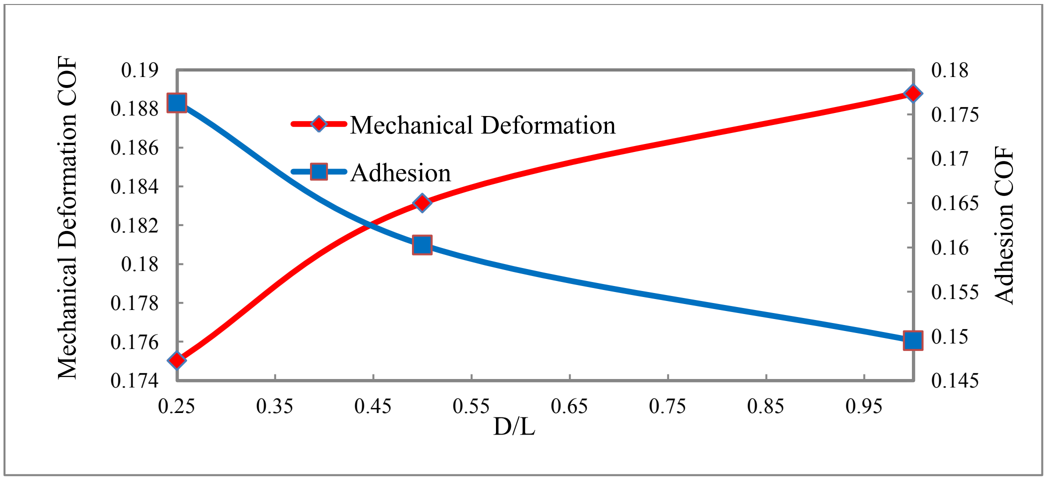

Figure 3-17: Coefficients of Friction due to Mechanical Deformation and Adhesion for the Circular Diameter of 20 μm

For the mechanical deformation component, there is a trend between the size of the dimples and the coefficient of friction. As the size of the dimples increases, the coefficient of friction due to the mechanical deformation decreases as shown in Figure 3-18. For the adhesion component, there is no clear trend that is revealed between the size of the dimple and the adhesion component when the adhesion friction coefficients are plotted for the three diameters in Figure 3-19. As a result, it is very misleading to identify the size of the texture as a significant texture parameter since the adhesion component, which shows no relationship with dimple diameter, crucially contributes to the overall friction coefficient.

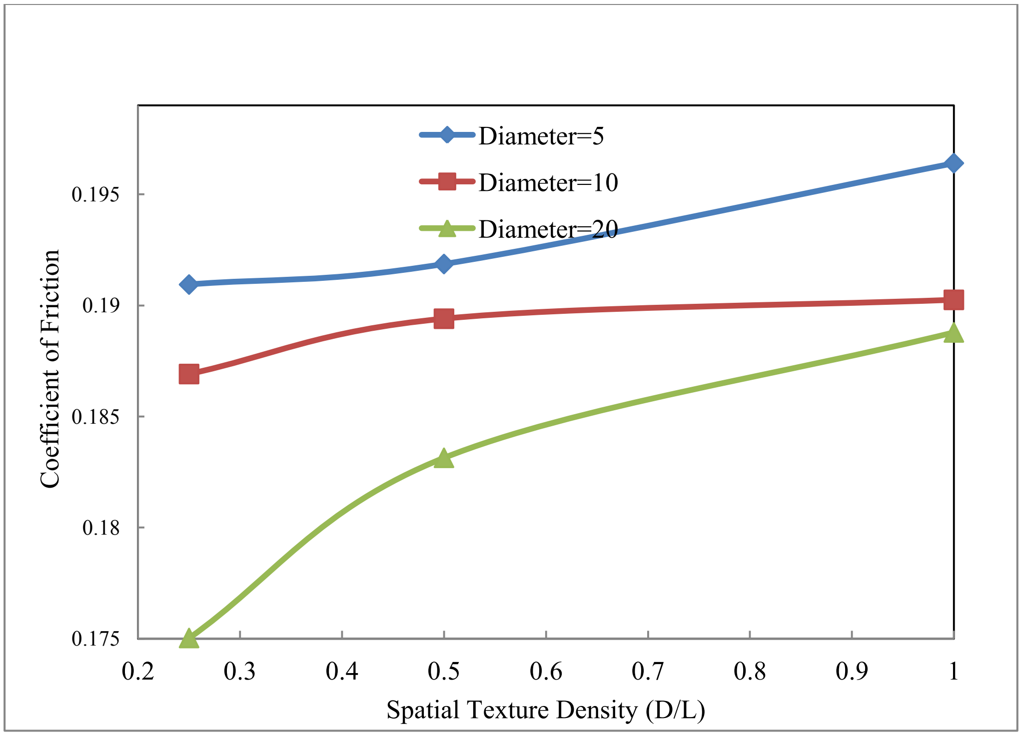

Figure 3-18: The Mechanical Deformation Component for 3 Different Dimples' Diameters

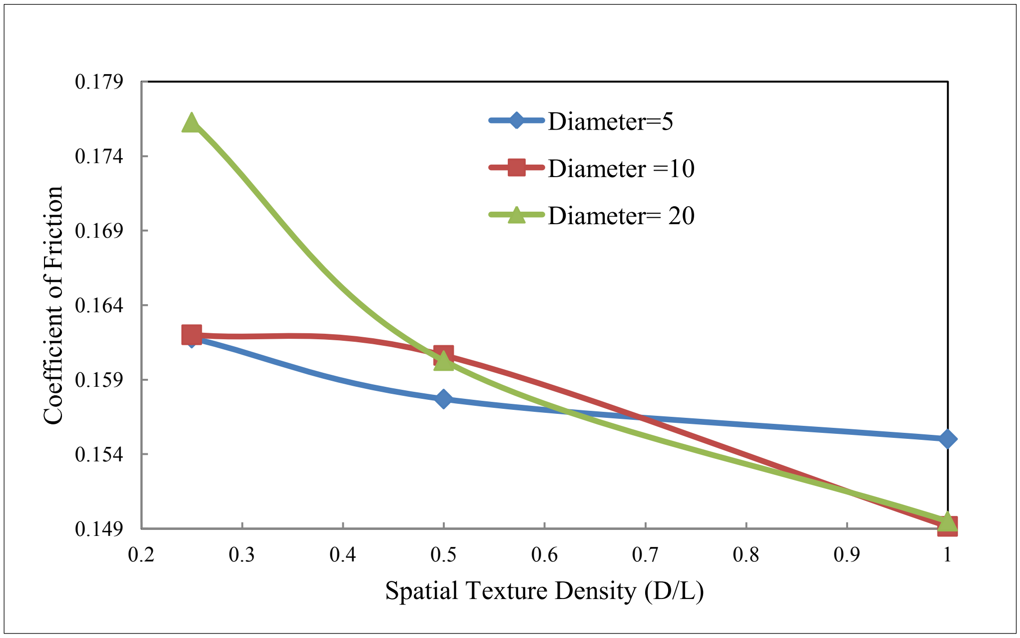

Figure 3-19: Adhesion Component for the Three Different Dimples' Diameters

For the purposes of comparison with the experimental samples, the overall friction coefficients that combine the effects of the mechanical deformation and adhesion components are curve fitted, and plotted against the spatial texture densities for the three different dimples' sizes as shown in Figure 3-20.

There is an observed region with a minimum coefficient of friction that ranges between the spatial texture densities of 0.25 and 0.5. This confidently proves the hypothesis of the existence of an optimal surface patterning. Also, there is no clear trend between the dimple size and the overall friction coefficient, consequently, the dimple size cannot be recognized as a significant parameter. Figure 3-21 shows the plastic deformation zone which results from the sliding of the indenter on the patterned surface. This proves that the plastic mode is the dominant mode of the mechanical deformation component.

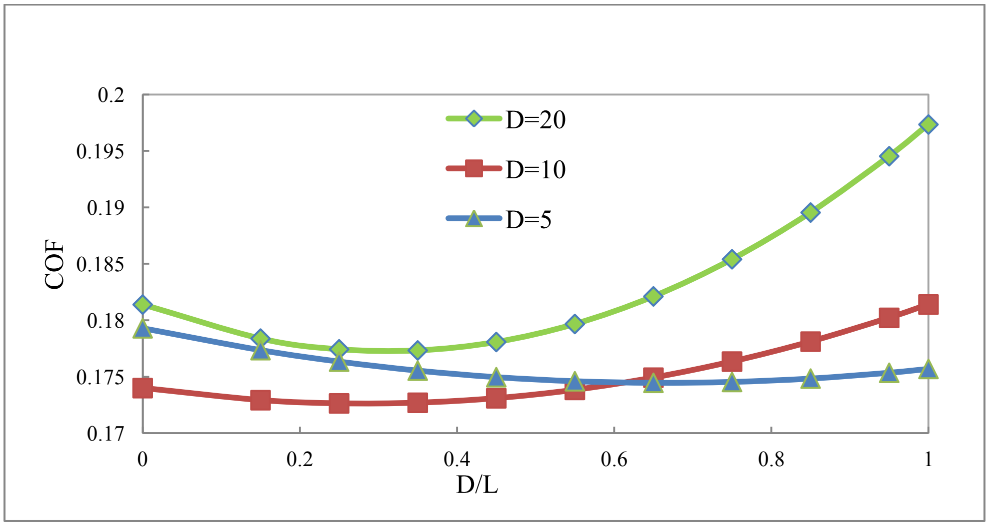

Figure 3-20: The Overall Coefficient of Friction Curve Fitted for the Three Different Diameters for Circular Dimples

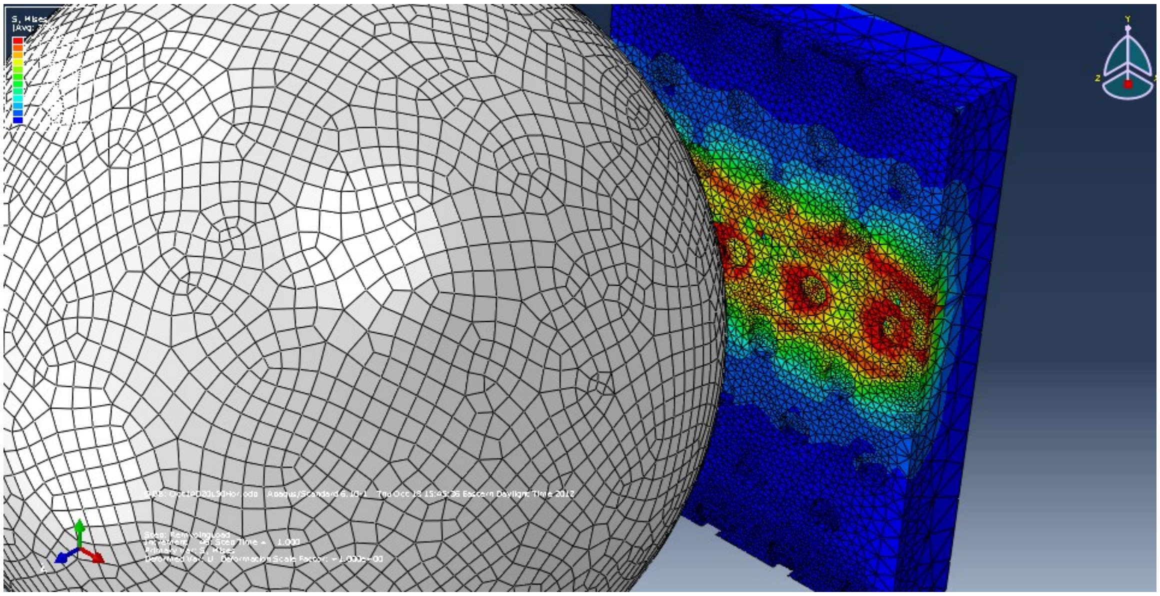

Figure 3-21: Von Mises Stress Shows Plastic Deformation Mode along the Sliding Path

3.5.2 The Numerical Models for Hexagonal Patterns

Hexagonal dimples are modeled in an equilateral triangle layout. The diameter of the hexagon, D equals the diameter of the circumscribed circle (vertex to vertex), while L is the distance between the centers of the two adjacent hexagons as shown in Figure 3-22. Different models with different texture parameters, which are listed in Table 3-3, are developed, and the effect on the coefficient of friction is examined.

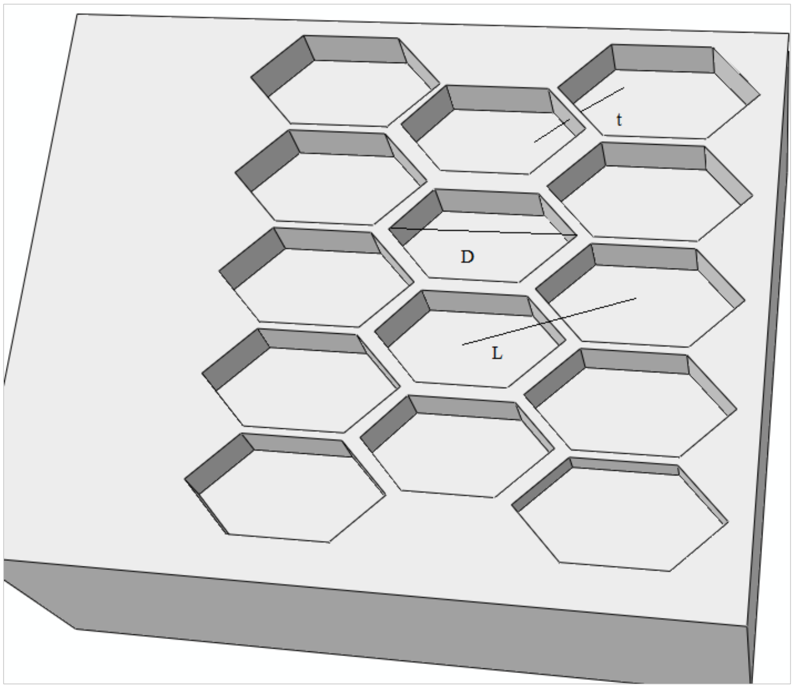

Figure 3-22: Hexagonal Pattern Texture Parameters

The spatial texture density (D/L) was narrowed down to between 0.25 and 0.667 in order to verify the optimum spatial texture density bracket, from 0.25 to 0.5, at which the minimum coefficient of friction should exist. The same hexagonal texture parameters were fabricated using photolithography to validate the outputs of the finite element models.

Table 3-3: Combination of the Spatial Texture Densities and Hexagonal Dimples Diameters

D (μm)	15	15	15	15	20	20	20	20	40	40	40	40
L (μm)	22.5	30	37.5	60	35	40	50	80	60	80	100	160
D/L	0.667	0.5	0.4	0.25	0.667	0.5	0.4	0.25	0.667	0.5	0.4	0.25

In the mechanical deformation and adhesion components curves in Figure 3-23-through Figure 3-27, the behaviour is similar to that with the circular patterns. As the spatial texture density (D/L) increases, the coefficient of friction due to the mechanical deformation increases as well, while the coefficient of friction due to the adhesion component decreases. This contributes to the decrease in the contact area which results in very high contact stresses that make the material flow plastically. In addition, the optimal spatial texture densities, at which the minimum overall coefficient of friction falls, are bracketed between 0.25 and 0.5.

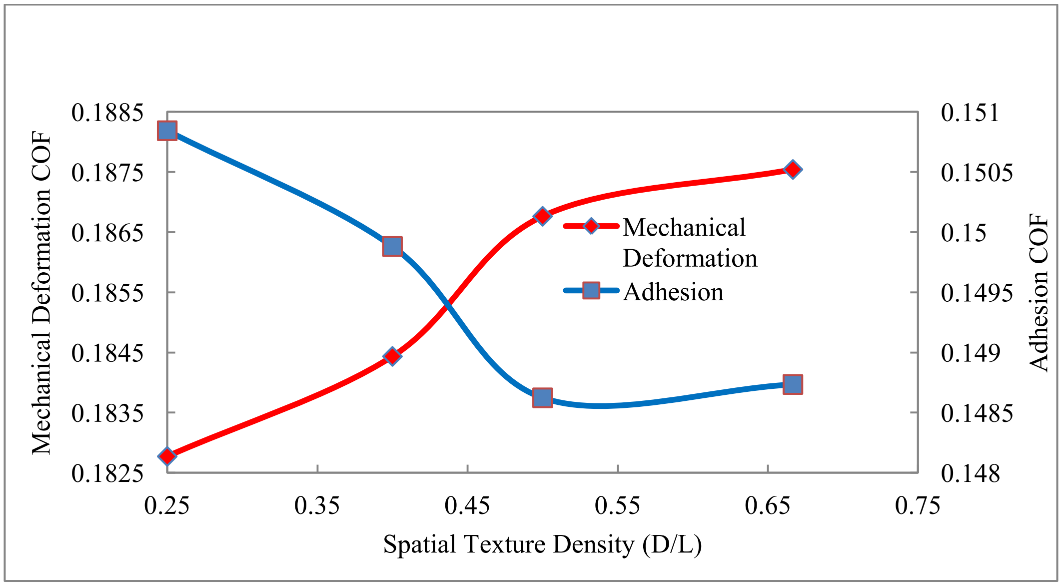

Figure 3-23: Coefficient of Friction Due to Mechanical Deformation for Hexagonal Diameter of 15 µm

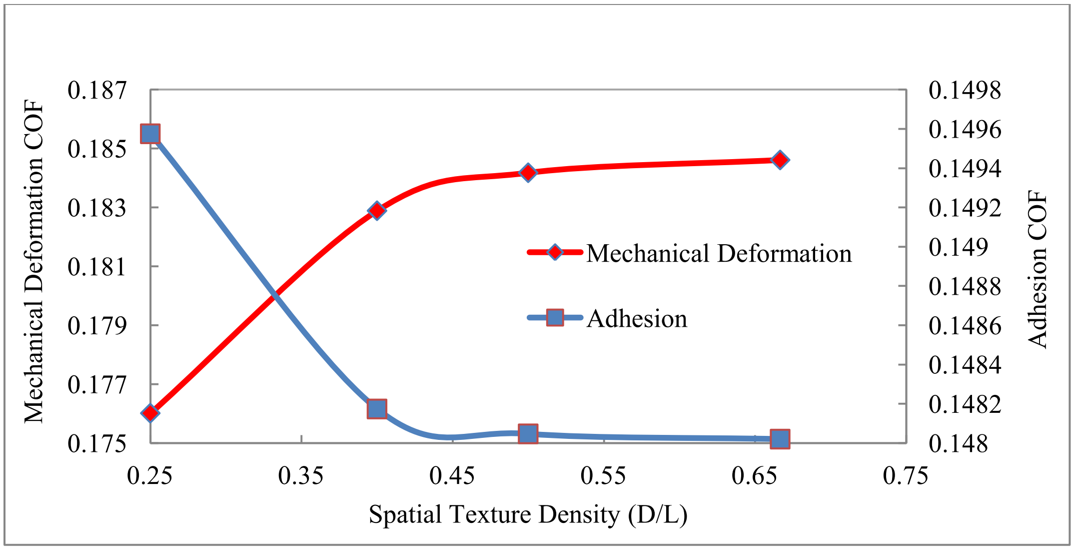

Figure 3-24: Coefficient of Friction Due to Mechanical Deformation and Adhesion for Hexagonal Diameter of 20 μm

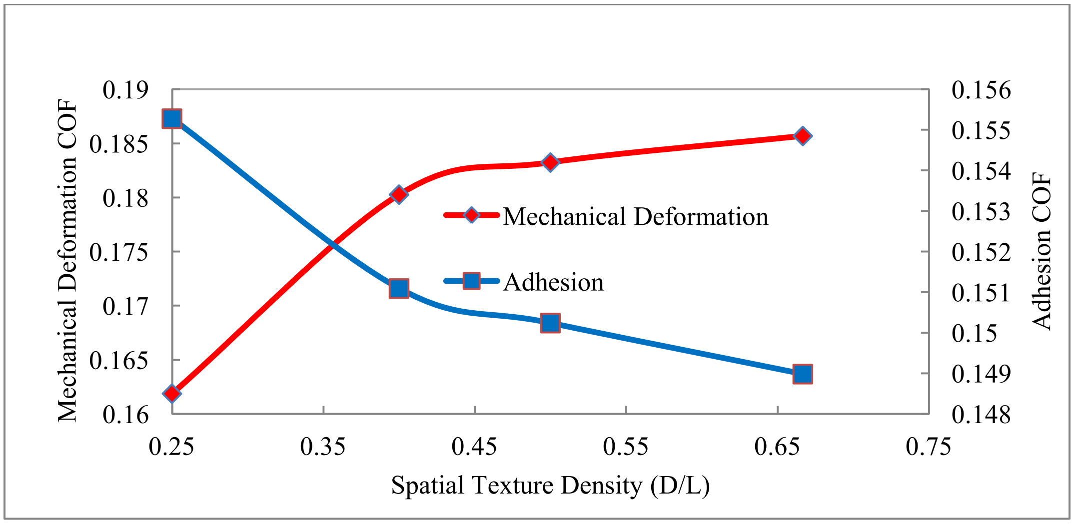

Figure 3-25: Coefficient of Friction Due to Mechanical Deformation and Adhesion for Hexagonal Diameter of 40 μm

In Figure 3-26, the friction coefficients due to the mechanical deformation that occurred during the sliding step are plotted against the spatial texture densities for different hexagonal diameters of 15 μm, 20 μm, and 40 μm. Figure 3-27 depicts the adhesion component of the friction coefficients versus the spatial texture density. The same trend is observed, as the texture diameter increases, the friction coefficients due to the mechanical deformation decrease. For the adhesion component, as with the circular pattern, no obvious trend is recorded.

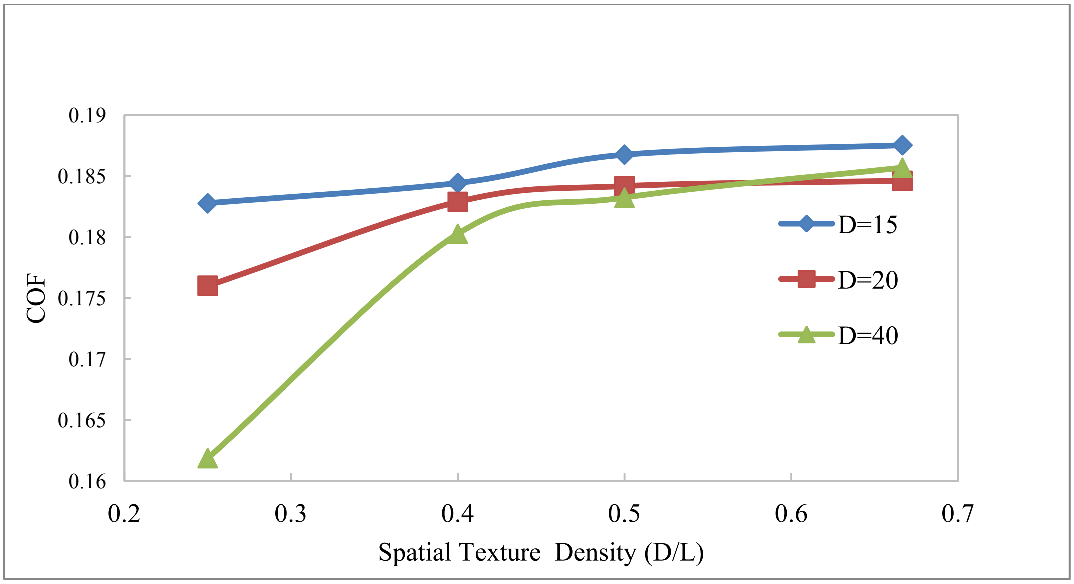

Figure 3-26: Coefficient of Friction Due to Mechanical Deformation for the Three Hexagonal Diameters

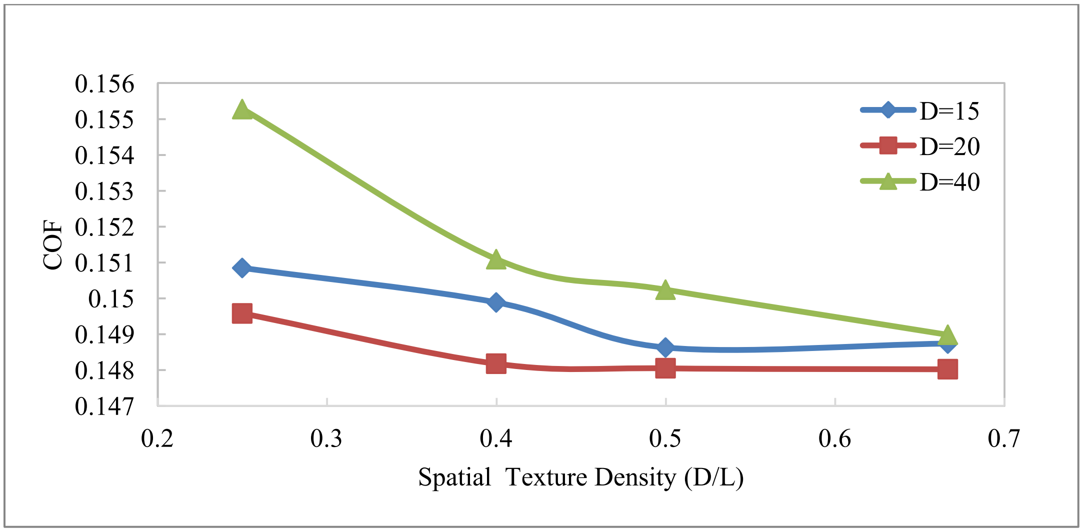

Figure 3-27: Coefficients of Friction Due to Adhesion for the Three Hexagonal Diameters

3.5.3 The Effect of the Texture Shape on COF in the 3D Numerical Models

When the friction components, adhesion and mechanical deformation, for two different shapes (hexagonal and circular) of the same size of 20 μm are compared, it can be concluded that for the adhesion component of the friction in Figure 3-28, at the small spatial texture density, both circular and hexagonal shapes perform similarly. However, when the spatial surface texture density increases, the circular shape outperforms the hexagonal, and it records a smaller adhesion friction coefficient. On the contrary, for the mechanical deformation friction component as shown in Figure 3-29, the hexagonal shape surpasses the circular shape, and it records lower coefficients of friction for all spatial texture densities. This behaviour may be explained by the fact that the contact area which results from the circular texture shape is less than that of the hexagonal shape because the area of the hexagon is less than the area of the circle of the same diameter.

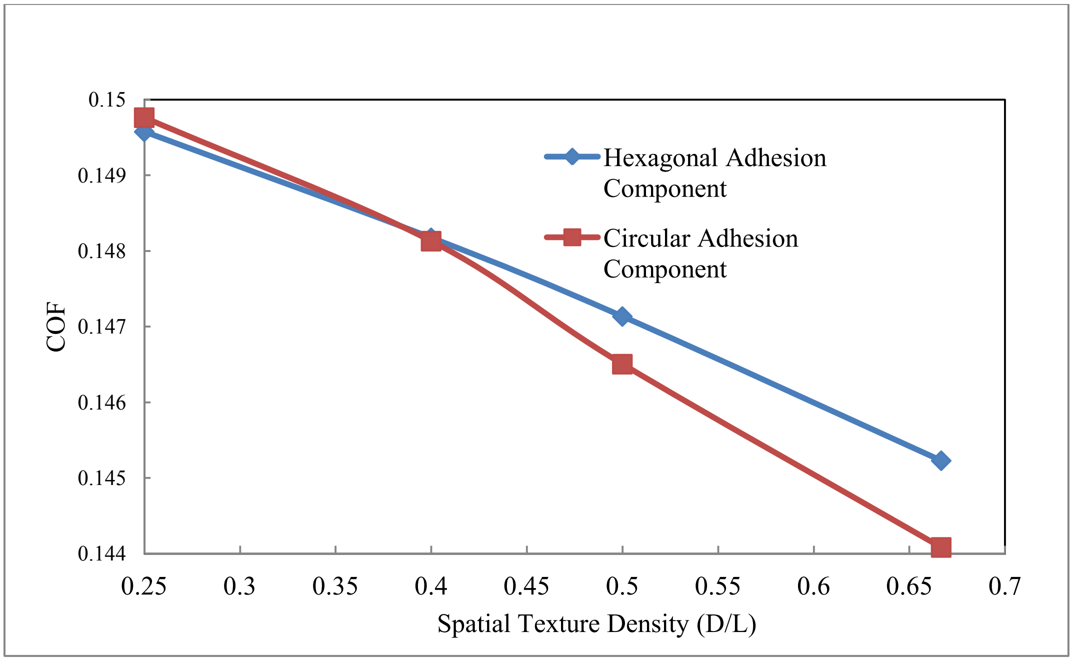

Figure 3-28: Comparison between Circular and Hexagonal Shapes for the Adhesion Component of Friction

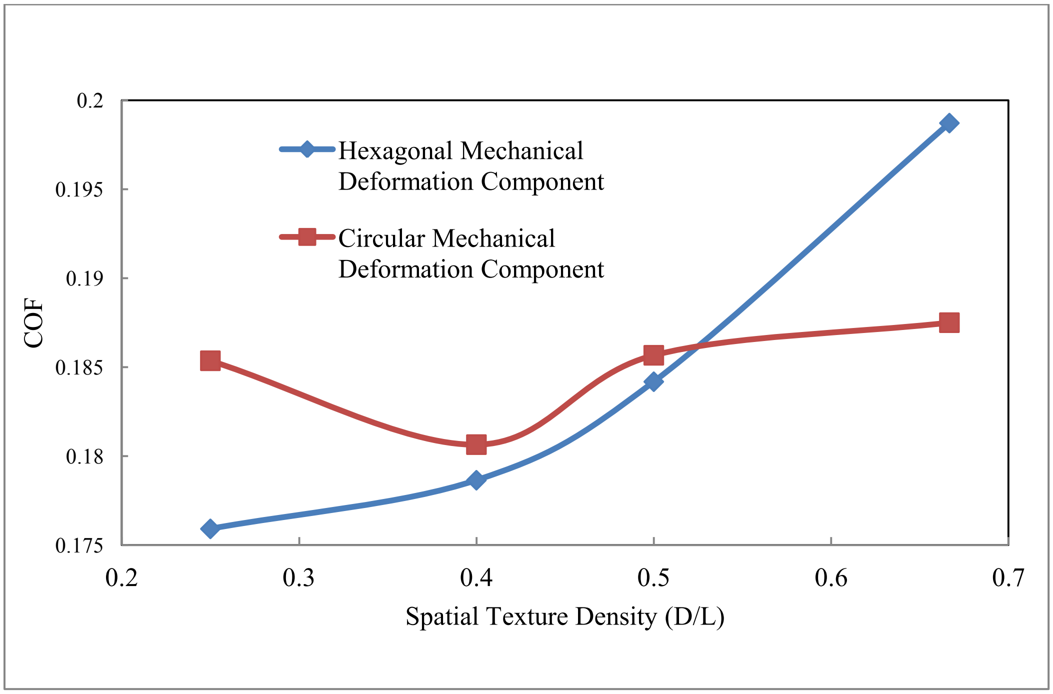

Figure 3-29: Comparison between Circular and Hexagonal Shapes for the Mechanical Deformation Component

3.5.4 The Effect of the Pattern Anisotropy on COF of the 3D Numerical Models

As it was mentioned in earlier sections, the dimples are set into an adjacent equilateral triangles layout. In Figure 3-30, the spatial texture density in most of the directions is the same, however, the spatial texture density in the vertical direction differs. Therefore, a comprehensive investigation is done to investigate the effects on the coefficient of friction components. The same loading conditions are applied to the hexagonal patterns with different spatial texture densities except for the sliding direction. Instead, the indenter slides along Y direction for the same distance of 200 μm as shown in Figure 3-31. The components of the friction coefficients in the vertical direction and horizontal direction, as well for different spatial texture densities are depicted in Figure 3-32. At the small spatial texture densities of 0.25 and 0.4, the coefficient of friction components that result from the vertical sliding are higher than those that result from the horizontal sliding. Yet, when the spatial texture density increases up to the value of 0.667, the coefficient of friction results from the vertical sliding are less than the coefficient of friction results from the horizontal sliding. In order to elucidate this behaviour it is worth pointing out that in the vertical direction, spatial surface texture density (D/L) is reduced by factor of $\frac{1}{\sqrt{3}}$. Therefore, for the small spatial texture density (D/L) of 0.25, the resulting spatial texture density in the vertical direction $(D/L)_v$ is less than 0.25, which is outside the optimal bracket extending from 0.25 to 0.5. Conversely, when the spatial texture density is 0.6667, the consequent spatial texture density in the vertical direction $(D/L)_v$ is approximately 0.385, which falls into the optimal bracket. This justifies the trend of the friction coefficients shown in Figure 3-32. The difference in the friction coefficients resulting from the horizontal and vertical sliding is less than 3% which indicates the insignificant effect of the pattern anisotropy.

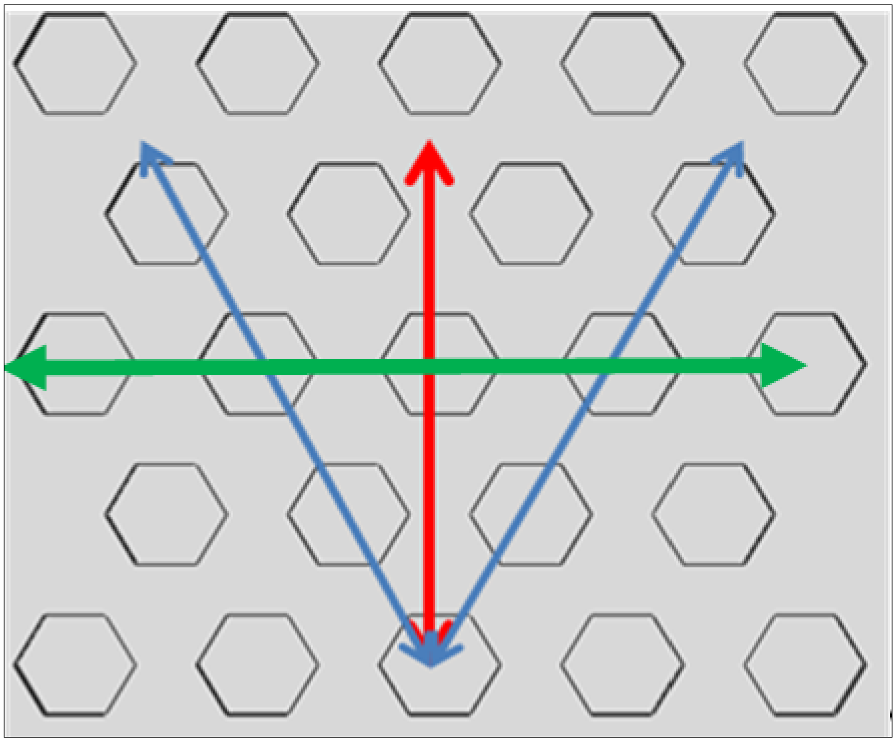

Figure 3-30: The Vertical Direction has Different Spatial Texture Density

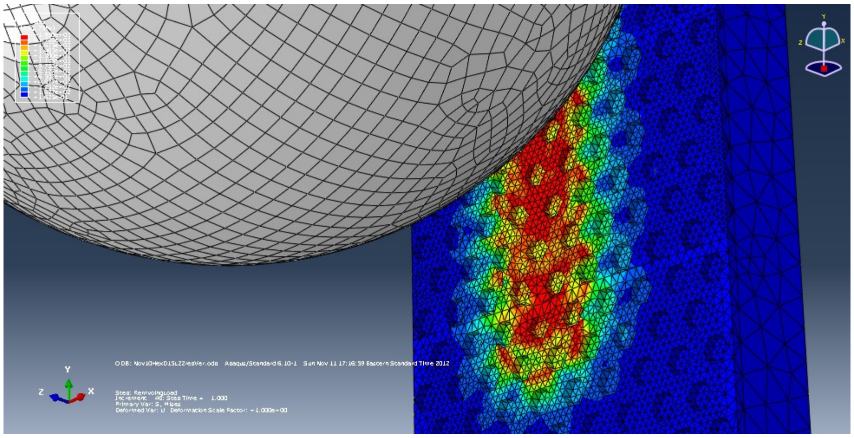

Figure 3-31: The Plastic Flow along the Vertical Sliding Path of the Indenter

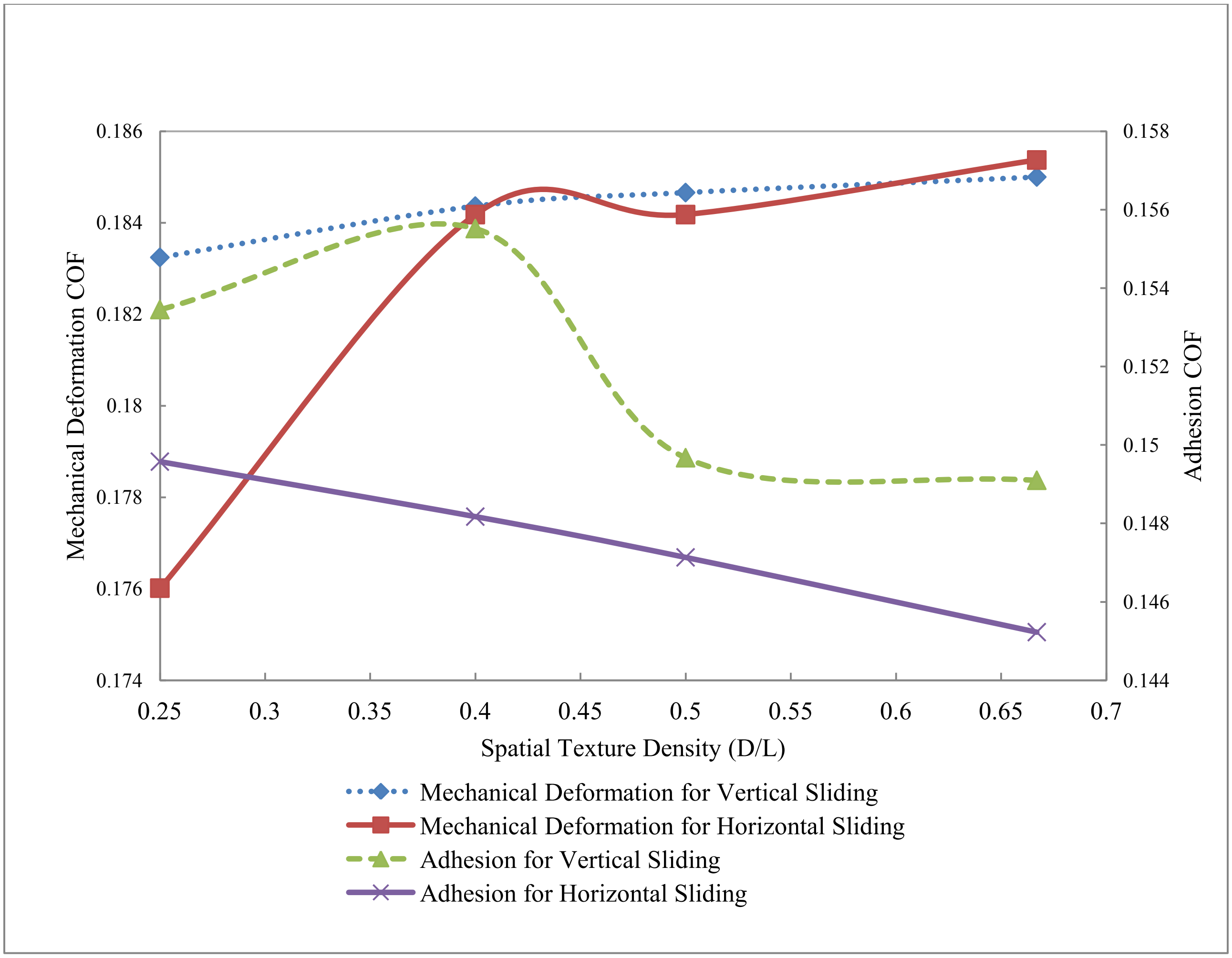

Figure 3-32: Comparison between the Horizontal Sliding and Vertical Sliding for Diameter 20 μm

3.6 Conclusions of the Numerical Simulations

In this chapter, two dimensional plane strain models, and three dimensional models of the patterned surfaces in contact with the rigid indenter were developed using the multipurpose finite element code, ABAQUS6.10. Normal and sliding contact were simulated, and the effect of the surface patterning on the coefficient of friction was investigated.

The two-dimensional plane strain models were initially used to predict the effect of the texturing on the friction coefficient. A fractal Cantor set was superimposed on the meandered patterned surface to simulate the real engineered surface. No perceptible correlation between the coefficient of friction and width of the square pads was found. However, a minimum coefficient of friction was found when it was plotted vs. the spatial texture density (D/L). The minimum coefficient of friction was found at (D/L) equals 0.4.

The 3D finite element simulations were developed to further inspect the effects of surface texturing on the coefficient of friction components of mechanical deformation and adhesion under dry sliding conditions. Each model consisted of three steps. First was to bring a rigid indenter into contact with the solid deformable patterned surfaces of different texture parameters, but at the same depth of 5 μm. Second was the sliding step, during which the mechanical deformation component of the coefficient of friction was estimated. The final step was to remove the rigid indenter from the patterned surface. During the last step, the adhesion component of the coefficient of friction was measured. The texture parameters, such as the diameter, shape, and orientation were investigated, and the following conclusions were attained:

1. The overall minimum coefficient of friction exists and it falls from 0.25 to 0.5 of the spatial texture density.
2. As the spatial texture density (D/L) increases, the coefficient of friction due to the adhesion component decreases as a result of the reduction in contact area.
3. As the spatial texture density (D/L) increases, the coefficient of friction due to mechanical deformation increases because of the decrease in the contact area, hence an increase in the concentrated stress.
4. The hexagonal shape gives a lower coefficient of friction for the spatial texture densities from 0.25 to 0.5, however, the circular pattern gives lower coefficient of friction at higher spatial texture densities.
5. When D/L is greater than or equals to 0.5, the difference between the two shapes is less than 1% which is considered insignificant.
6. The proposed patterns do have anisotropic properties; however, the difference in the coefficient of friction in the two perpendicular sliding directions is less than 3%.

7. The material falling within the indenter sliding path undergoes plastic deformation, which justifies the higher mechanical deformation component of the friction.

These results are validated experimentally by fabricating the same texture parameters using laser and photo-lithography methods, which are described in detail in chapter #4 and chapter#5.

Chapter 4 CIRCULAR SURFACE TEXTURING BY LASER ABLATION

In this chapter, micro circular dimples of different sizes and densities, which were analysed by the finite elements method, were fabricated by the laser ablation technique to validate the results predicted by the numerical models. In this study, the coefficients of friction were evaluated by the micro scratch tester.

4.1 Material Properties and Sample Preparation of the Circular Texture

The samples which were used in this study were air hardened tool steel (A2) with a measured hardness of 2.04 GPa. One long rectangular bar is cut into smaller blocks of 12x10x10 mm, so that all of the samples have the same material properties. The samples are ground and polished to a roughness of 50 nm using silicon carbide disks, followed by a diamond paste of 9 μm in size, and finally aluminum oxide suspensions of 0.1 μm and 0.05 μm.

4.2 Design of the Circular Patterns

Based on the findings of the finite elements study which was discussed in Chapter 3, three different diameters (D) of 5 μm, 10 μm, and 20 μm of circular dimples were fabricated using the laser ablation technique. The spatial distance (L), between the centers of the two neighboring circular dimples varies, and is equal to 10 μm, 20 μm, 40 μm, or 80 μm. However, spatial texture densities $\left[\frac{D}{L}\right]$

that are equal to 0.25, 0.5, and 1 are maintained constant for the different combinations between D and L, as listed in Table 4-1.

In addition, the arrangement of the circular craters forms adjacent equilateral triangles as shown in Figure 4-1, so that the direction of the applied load becomes an insignificant parameter, and the resulting stresses are propagated. The depth of the dimple is fixed and is equal to 5 μm.

Table 4-1: Different Combinations for Hole Diameters (D) and Spatial Distance (L)

Hole Diameter D (μm)	**For (D/L_1) =1 L_1 (μm)**	**For (D/L_2) =0.5 L_2 (μm)**	**For (D/L_3) =0.25 L_3 (μm)**
5	5	10	20
10	10	20	40
20	20	40	80

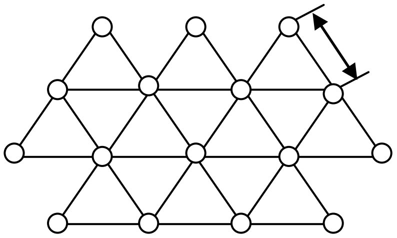

Figure 4-1: The Orientation of the Holes in Equilateral Triangles Arrangement

4.3 Fabrication of the Circular Patterns Using Laser Ablation

The high quality–high power CuBr vapour laser, which is equipped with an optical system for laser beam control as shown in Figure 4-2, is used to fabricate these micro dimples. Two wavelengths are used (510 nm and 578 nm). The power ranges from between 0.08 W to 1.6 W. At low pulse energies, the dimples consist of a central depression which is surrounded with a rim. As the pulse energy increases, the bottom of the crater flattens and a central dome is popped out. With a further increase in power, the central high dome is broadened and becomes lower than the rim, and eventually the central dome forms a depression in the middle.

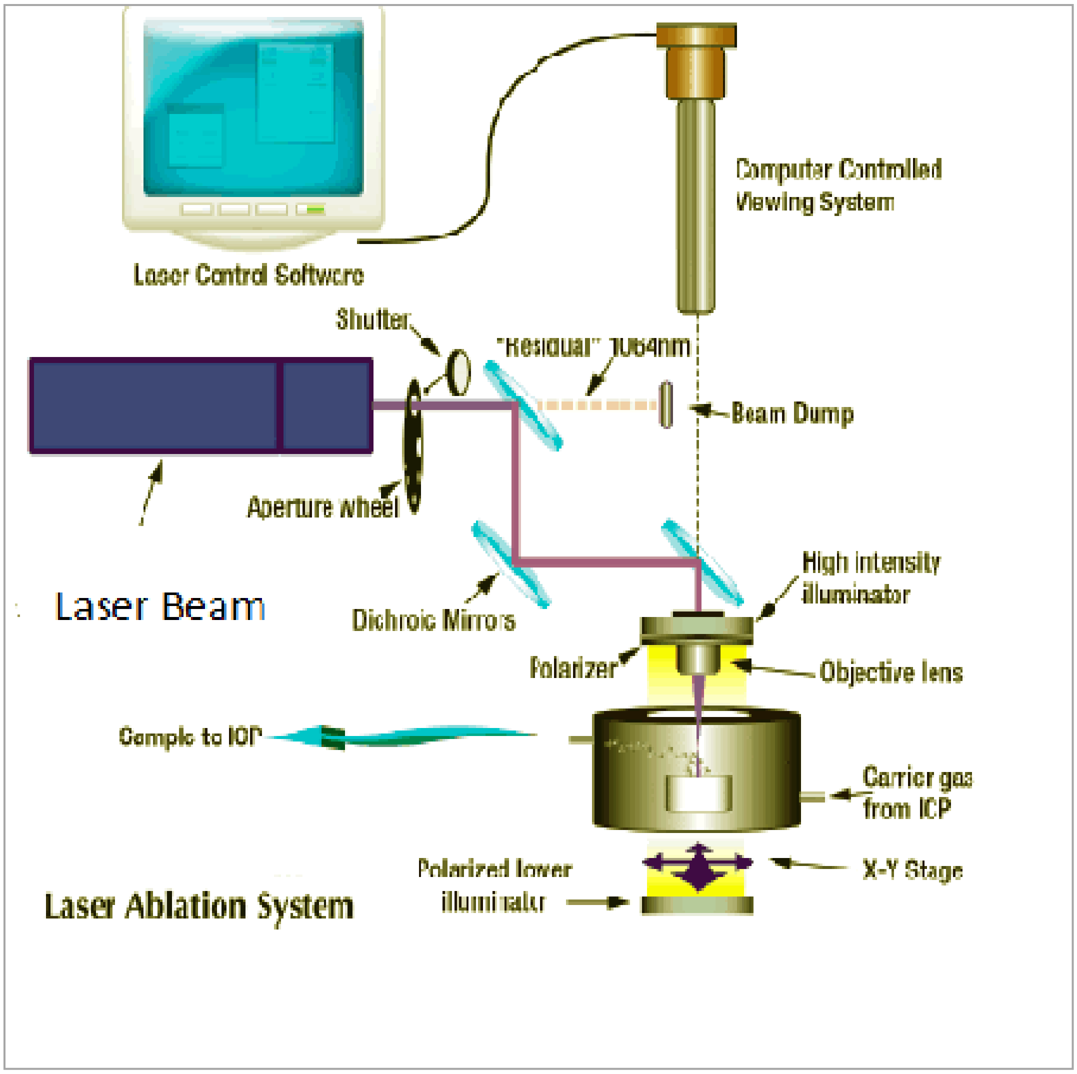

Figure 4-2: Laser Ablation System

The SEM and profilometer WYKO pictures for all samples are depicted in Figure 4-3, with magnifications of 500 x and 1200 x respectively. Light polishing was needed after the laser texturing in order to remove the burrs around the circular pockets. 1 μm diamond paste is used to remove these sharp burrs.

Sample #	**SEM**	**Profilometer Pictures**
1D5L5	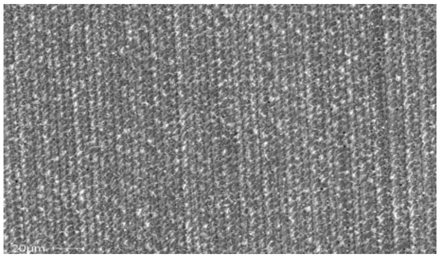	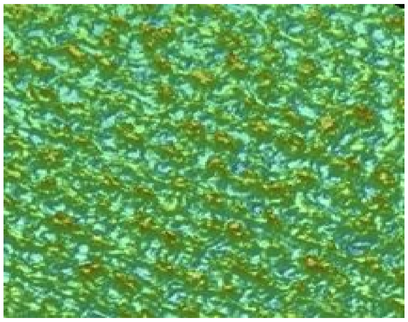
2D5L10	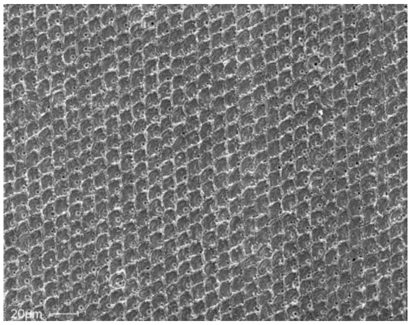	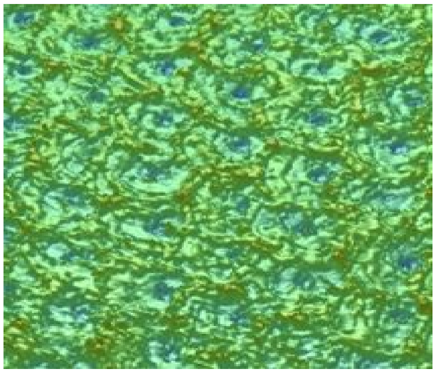
3D5L20	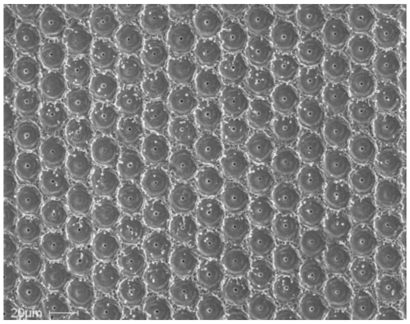	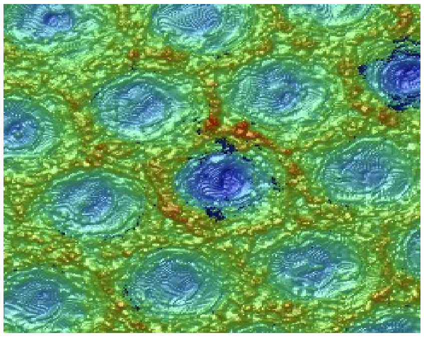
4D10L10	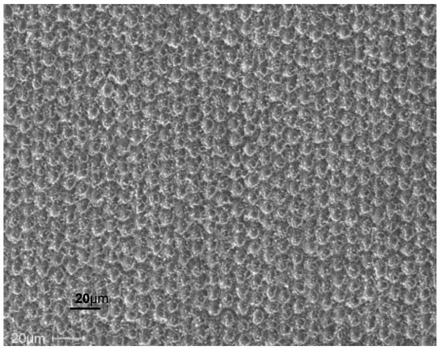	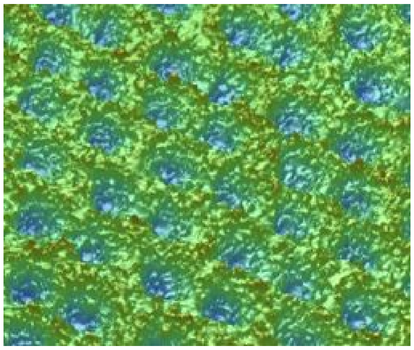

5D10L20

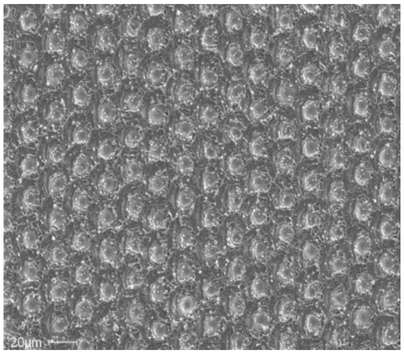

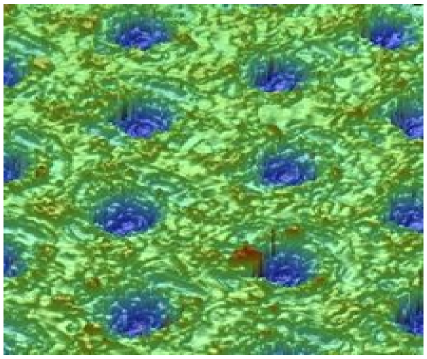

6D10L30

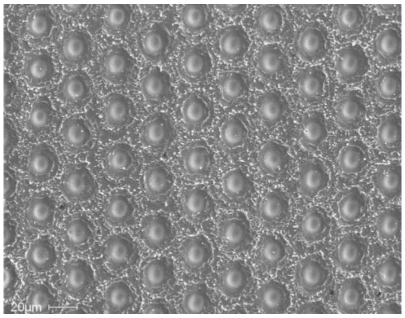

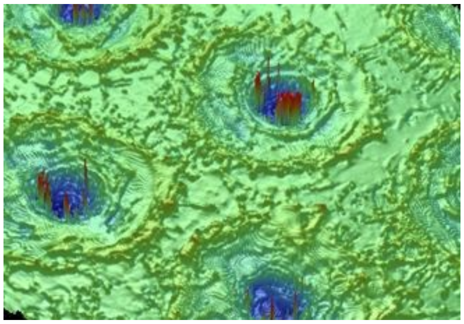

7D10L40

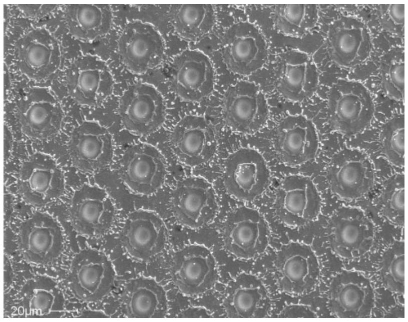

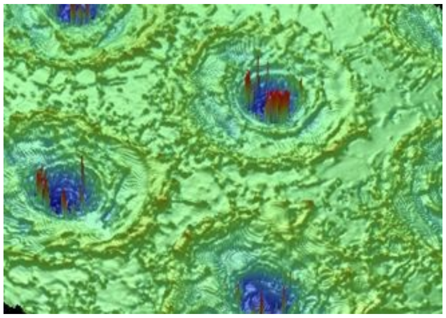

8D20L20

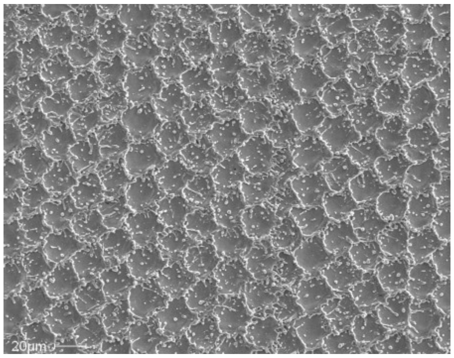

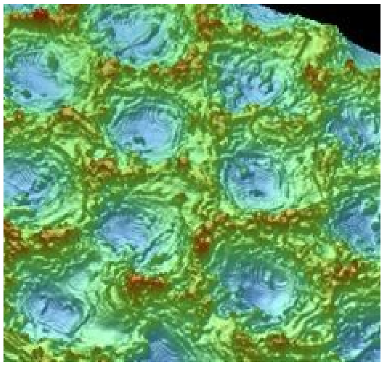

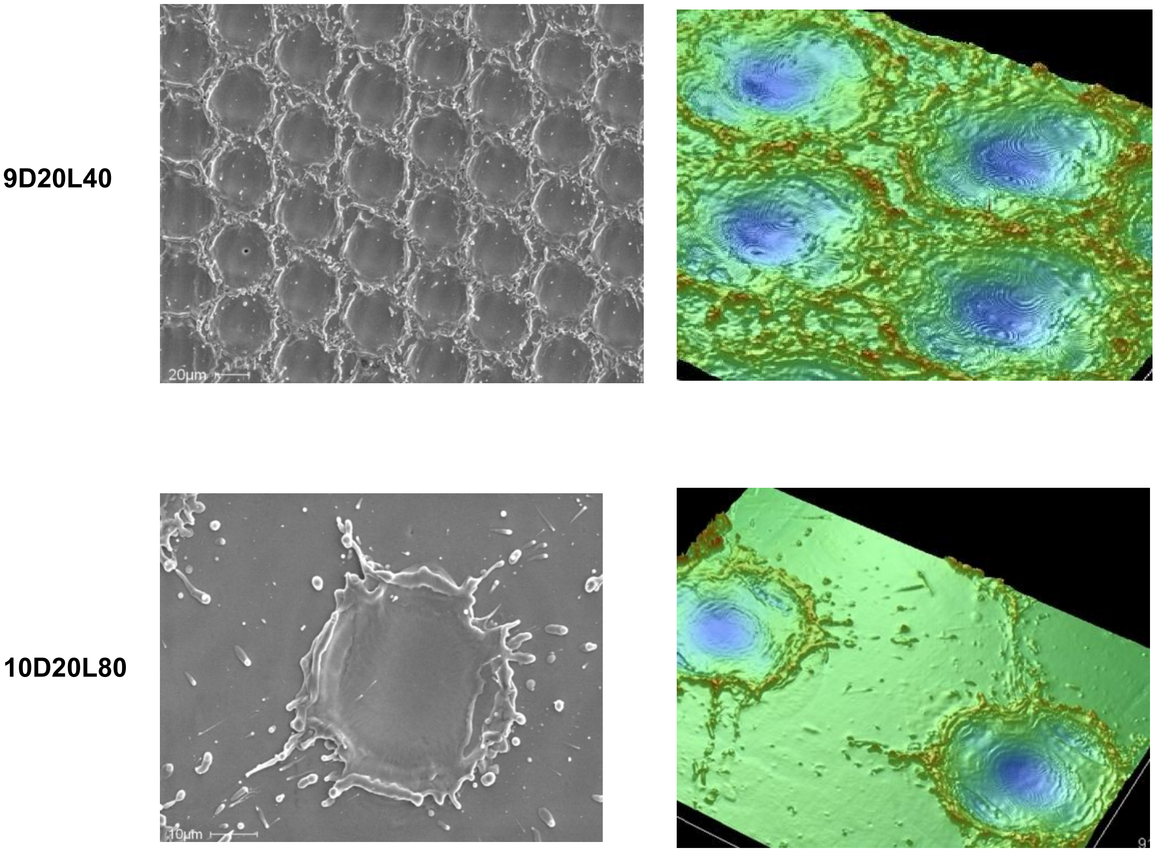

Figure 4-3: SEM and WYKO Profilometer Pictures for Circular Textured Samples

4.4 Tribological Tests for Circular Texture

A commercial micro scratch tester illustrated in Figure 4-4, with a diamond indenter, was used to measure the friction coefficient. The sliding stylus of the scratch tester is Rockwell C, and the radius of the spherical tip is 200 microns. Young’s modulus of the diamond indenter is 1140 GPa, the hardness is 80 GP, and Poisson’s ratio is 0.07. This conical indenter is selected so that any directionality in the measurements is eliminated.

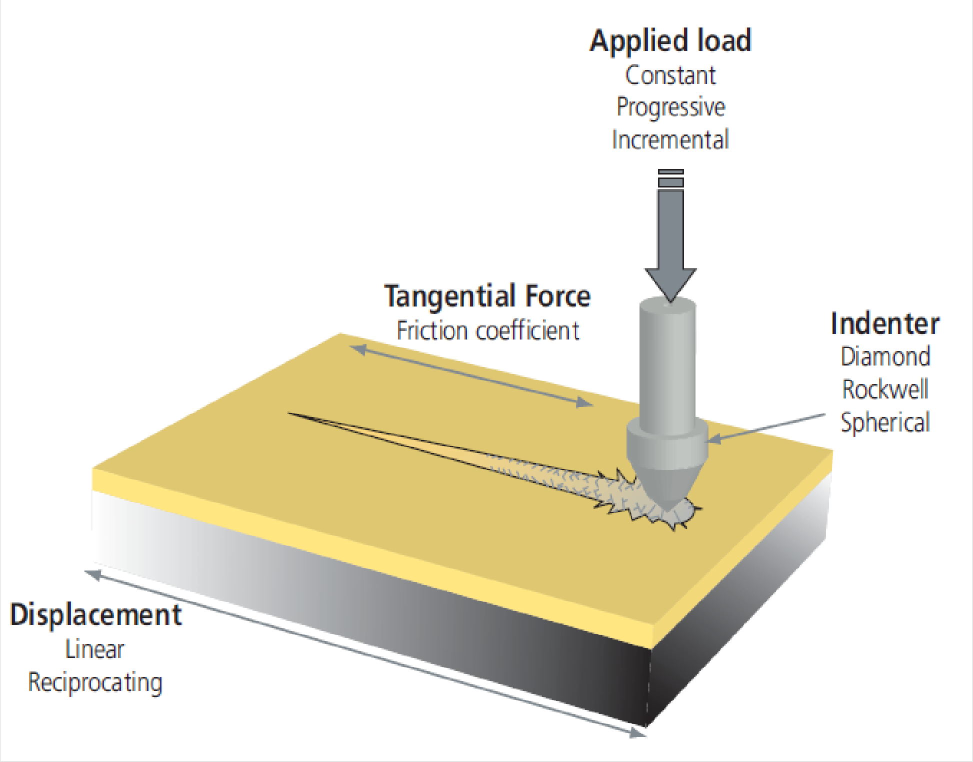

Figure 4-4: Micro scratch Tester with Rockwell Diamond Tip

Three linear scratches of 500 microns were made at the center of each textured sample, as well as the un-textured (plain) reference sample, and then the average friction coefficients were calculated. The scratches were done under a constant loading condition of 7 N at a speed of 0.5 mm/min. The tangential and instantaneous normal forces were recorded at the interval of 1 μm. Micrographs of the resulting scratches are depicted in Figure 4-5.

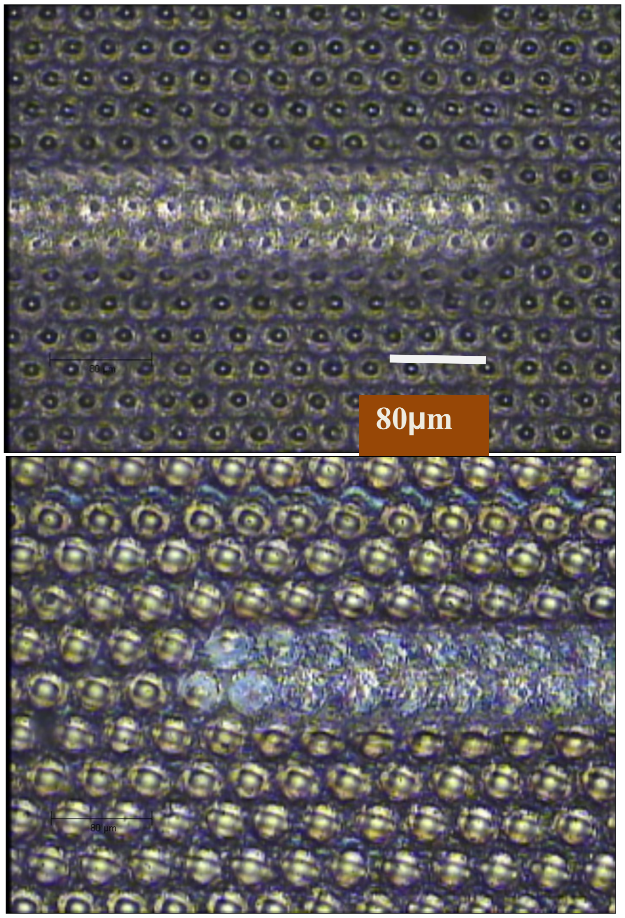

Figure 4-5: The Scratches of Samples # 6D10L30 (Top) and # 9(D20L40)(Bottom)

4.5 Results and Discussion of Circular Patterns

According to the discussion in Chapter 2, sliding friction under dry conditions is mainly attributed to adhesion and mechanical deformation, which are both affected by the real area of contact. In this section, the results of the scratch tester are the instantaneous normal force and the corresponding tangential force, from which the average coefficient of friction is calculated and plotted against the sliding distance. Then the difference in the coefficients of friction of the textured samples and the plain un-textured sample is calculated for each textured sample. The effect of the spatial texture density on the coefficient of friction is investigated, as well as the individual effect of the texture diameter (D), and the distance between the centers of two consecutive dimples (L).

4.6 The Effect of Circular Patterns on COF vs. Un-textured Surface

The effect of the surface texturing is pronounced on the coefficient of friction. The calculated friction coefficients of the textured samples are summarized in Table 4-2 and Figure 4-6 which display the average coefficient of friction of each sample. The plain sample, which is un-textured and mirror polished, has the highest coefficient of friction of 0.1606, and the standard deviations for all samples are less than 1 %, which indicates a small error as shown in Figure 4-6. However, it could be carefully generalized that under the dry sliding contact condition, any texture can reduce the coefficient of friction since the contact area is reduced; consequently, the adhesion component which has a major contribution to the friction, decreases. In Figure 4-6, for each diameter, a minimum coefficient of friction exists at spatial texture densities between 0.25 to 0.5. Sample 5D10L20 shows slightly higher coefficient of friction. This happens due to higher roughness that results in higher traction.

Table 4-2: Summary of the Experimental Results for Circular Texture Fabricated by Laser Ablation

Sample No.	Plain	1 D5 L5	2 D5 L10	3 D5 L20	4 D10 L10	5 D10 L20	6 D10 L30	7 D10 L40	8 D20 L20	9 D20 L40	10 D20 L80
Average	0.163	0.15	0.145	0.144	0.145	0.145	0.141	0.142	0.145	0.137	0.144
Standard Deviation	.003	.002	.002	0.001	0.003	0.006	0.000	0.003	0.002	0.002	0.001
Reduction %	0	4.23	9.54	10.49	9.76	6.66	12.22	11.23	6.68	14.50	9.87

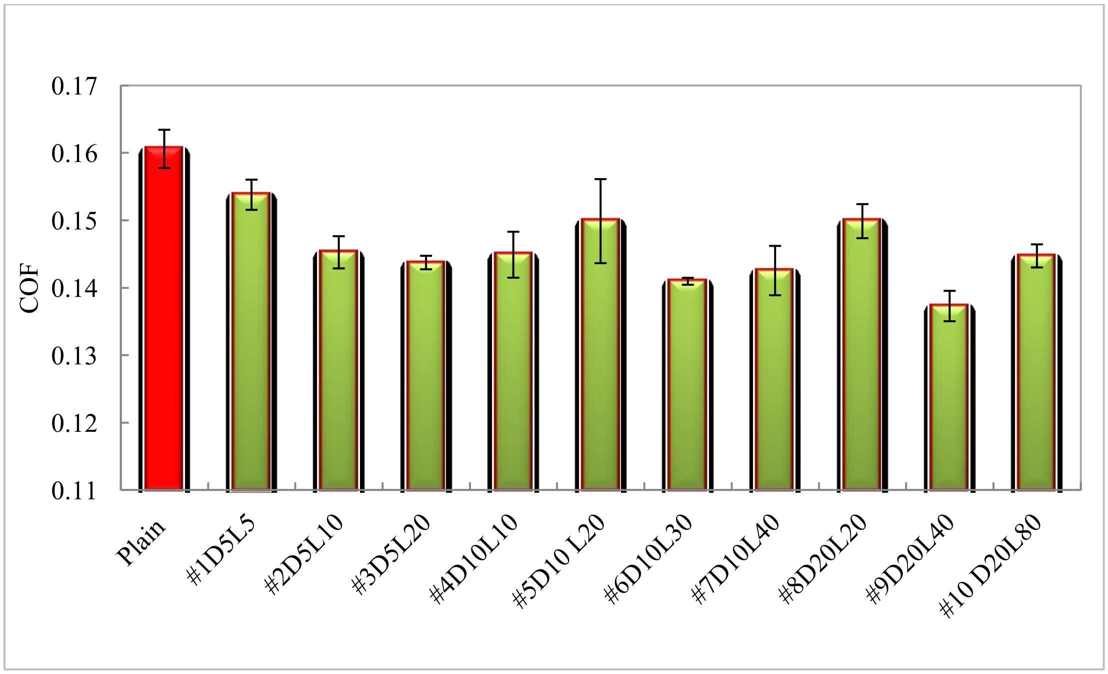

Figure 4-6: The Average Coefficients of Friction of the Textured Samples and the Plain (un-textured) Reference Sample

When the coefficient of friction is plotted against the sliding distance in Figure 4-7 through Figure 4-9 for the textured samples that have the same dimple diameter, but different spatial dimple densities that range from 0.25 to 1, the following observations are noticed. The coefficient of friction initially increases very rapidly with the sliding distance until it reaches a maximum value where the contact asperities start to deform plastically. The coefficient of friction starts to stabilize when the real contact area of the micro asperities undergoes full plastic deformation and they start to support the load.

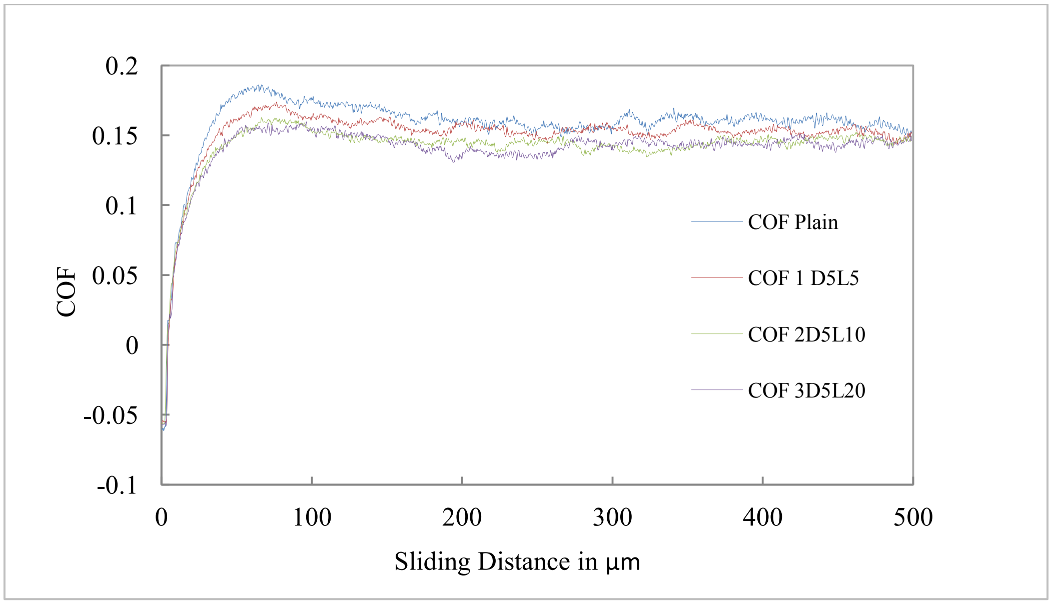

Figure 4-7: The Coefficient of Friction vs. the Sliding Distances for the Dimple Size of 5 µm

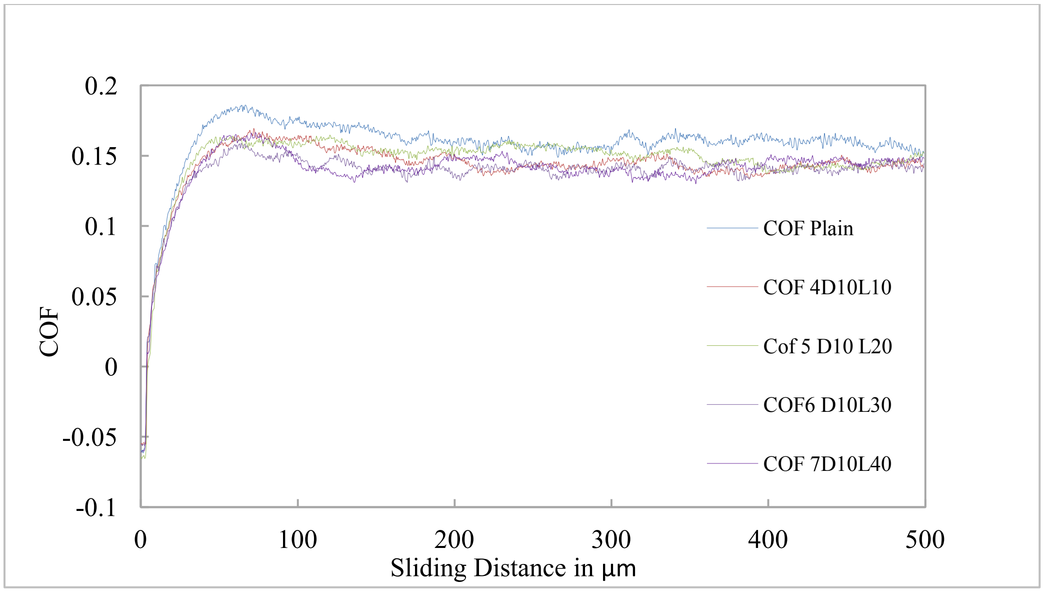

Figure 4-8: The Coefficient of Friction vs. the Sliding Distances for the Dimple Size of 10 µm

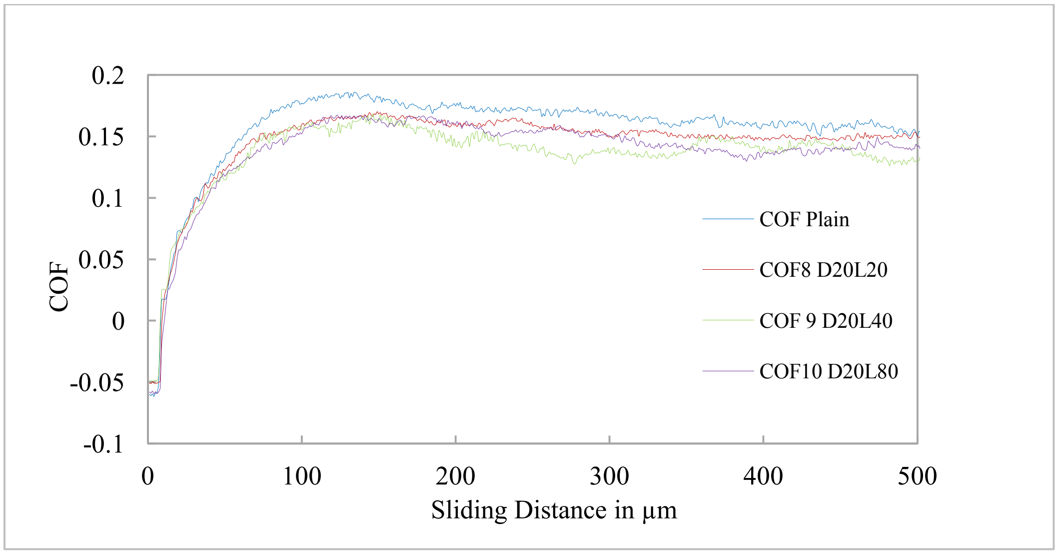

Figure 4-9: The Coefficient of Friction vs. the Sliding Distances for the Dimple Size of 20 µm

Despite the fact that texturing reduces the contact area, the contact pressure and the plastic deformation component increase as a consequence. These dimples also entrap any wear debris, and reduce the number of the asperities that might interlock with the countersurface. So, the overall consequence is less plowing force, and less plastic deformation.

4.6.1 The Effect of Individual Texturing Parameters on COF

Some researchers [12, 26, 43] recommended specific optimum dimple sizes. In Figure 4-10, neither the effect of the diameter size (D), nor the spacing between the dimples (L) has a clearly pronounced trend as an independent parameter. For example, for the same spacing of L= 20 μm, the lowest coefficient of friction belongs to D= 10 μm, and the highest value occurs at D= 20 μm. Therefore, it is quite imprecise to specify certain values for the individual texture parameters at which the lowest coefficient of friction might exist. However, the combined texture parameters might be more indicative as shown in section 4.6.2.

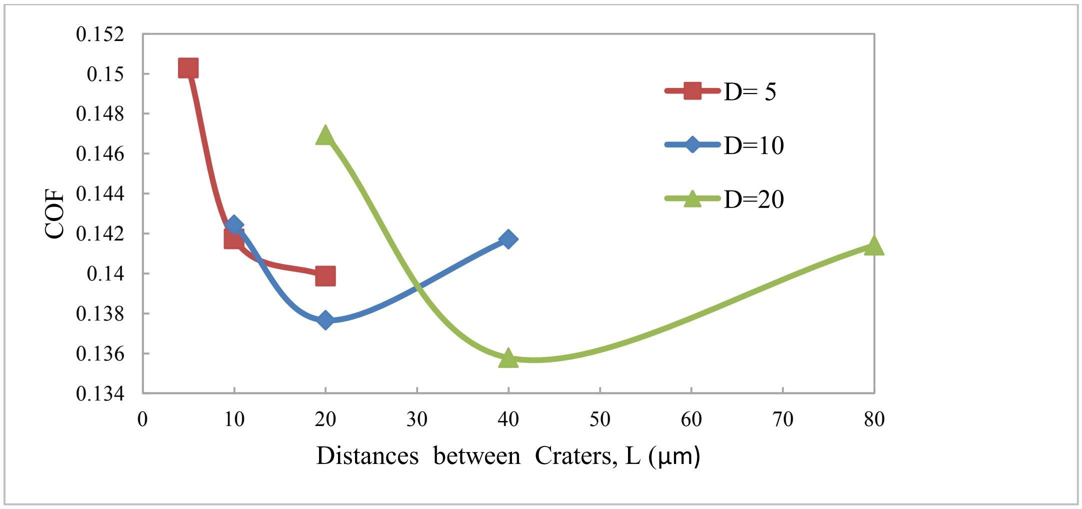

Figure 4-10: Effect of the Spacing L for Different Dimple Diameters

4.6.2 The Effect of the Spatial Texture Density on COF

When the spatial texture density $\frac{D}{L}$ increases from 0.25 to 1, the corresponding coefficient of friction varies. At the spatial texture density $\frac{D}{L}$ of 1, the coefficient of friction is the highest. This is repeated with all dimple diameters, yet it is very much manifested with the small dimple size. This phenomenon might be due to the increase in the overall number of the asperities around the rims of laser craters that interlock with the other asperities of the countersurface. In addition, this might be due to the significant decrease of the area of contact that results in high contact pressure, causing severe plastic deformation and a high coefficient of friction as a result.

If the averaged friction coefficients are plotted against the different $\frac{D}{L}$ of the spatial dimple densities as shown in Figure 4-11, there is a certain spatial texture density at which the coefficient of friction is at a minimum. This texture density does not depend either on the dimple diameter (D), or the spacing between the dimples (L), but it does depend on the interaction (ratio) between the diameter of the dimples (D) and the distance between the centers of two consecutive dimples (L). The minimum coefficient of friction is obtained at a certain spatial texture density (D/L), and this ratio is found to be 0.5. To be more precise and to generalize this observation, this ratio ranges between 0.25 and 0.5, yet it should not exceed 0.5 of the spatial dimple density.

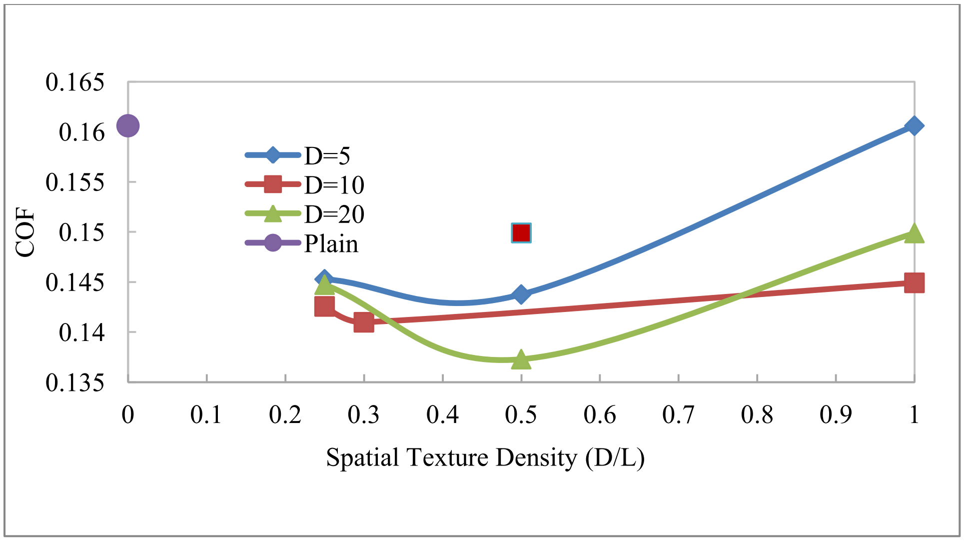

Figure 4-11: the Effect of the Spatial Dimple Densities for Different Diameters

The curve of the coefficient of friction vs. the spatial texture density can be divided into three regions. The first region is where the spatial texture density is high, while the contact area is small and the traction is very high. In this scenario, the adhesion component is relatively small since the contact area is small, while the mechanical deformation component contributes to the high traction as a result of high stresses, which are concentrated at a small area of contact.

In region II where the spatial texture density decreases and the contact area increases, the adhesion component increases, yet the plastic flow is relatively low due to the fact that the contact stresses are not very high, therefore the plowing component decreases. As a net result, the overall friction reaches its minimum value within this region. As for region III when the spatial texture density goes to 0, which means an un-textured (plain) surface, the adhesion component is rapidly increasing, but the concentrated stresses are decreasing as they are distributed over a large contact area. Accordingly, the coefficient of friction increases to a maximum value, but this time it is due to a high adhesion component. This proves that when the coefficient of friction is plotted against the contact area, it should have a minimum value, and this minimum value depends on the density of the surface texture and the material properties.

4.7 Comparison between Numerical Models and Experimental Results

If the outcomes of the numerical simulations are compared with the experimental results as shown in Figure 4-12, similar trends could be seen. When the spatial texture density is less than 0.25, higher coefficients of friction are observed. This might be attributed to the adhesion due to the increase in the real area of contact. In addition, the coefficients of friction increase when the spatial texture densities increase beyond the value of 0.5. This might be due to the increase of the number of the asperities around the dimples(holes) which result in higher interlocking and mechanical deformation, consequently increase in coefficient of friction. While, the minimum coefficients of friction fall between the values of 0.25 and 0.5 of spatial texture densities for both the numerical simulations and the experimental tests where both components of the friction force at minima.

Generally, the numerical simulation can be used as a time and cost effective tool for testing the different texture parameters before fabrication.

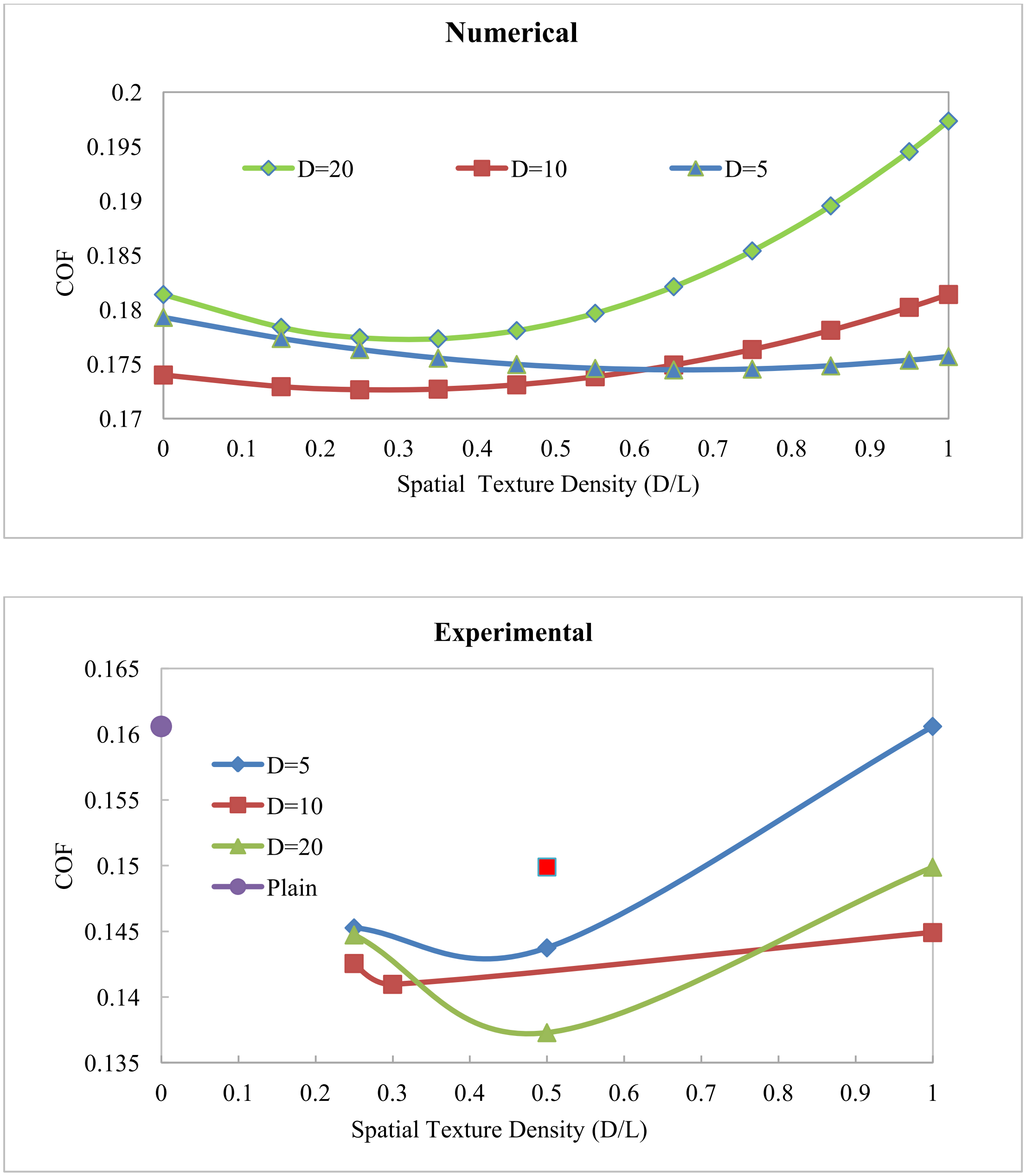

Figure 4-12: The Overall Fitted Coefficients of Friction Vs. the Spatial Texture Densities (D/L) for Numerical Simulations and Experimental Results

4.8 Conclusions of the Circular Patterns

In this study, the optimum texture parameters to control friction are sought. Laser ablation was used to create specific micro circular dimples on tool steel samples with different densities ranging from 0.25 to 1. The tribological performance of the textured surfaces, which undergoes the dry sliding condition, was evaluated by the scratch tester. The results demonstrate a reduction in the coefficient of friction of up to14.5%, and the following are concluded:

- In the case of the spatial dimple densities approaching 1, in other words when the circular dimples are overlapping or adjacent to each other, the coefficient of friction increases due to an increase in the plowing component of traction due to the reduction of the real contact area.
- Spatial dimple densities range from 25 % to 50 % and maintain a minimum COF for the different holes' sizes.
- The influence of dimple diameter or the spatial distance between the dimples on the COF is not evident as an independent parameter, and no trend is revealed.
- The ratio D/L is shown to have a trend when it is plotted against the coefficient of friction.
- The numerical simulations provide good approximations of the effect of texturing on the friction coefficients.

Chapter 5 HEXAGONAL PATTERNS USING PHOTOLITHOGRAPHY

After investigating the effect of circular dimples on the friction coefficients, the hexagonal pattern was designed and fabricated. In this chapter, the effect of a hexagonal pattern on the coefficient of friction was studied. First, the design of the hexagonal pattern is explained, followed by a description of photolithography (which is used to fabricate the hexagonal pattern). Then, scratch tribometer tests were done under the same conditions as the circular patterns. Finally, the results are presented and discussed.

5.1 Hexagonal Pattern Design

A hexagonal pattern is suggested as a viable way to propagate and distribute the concentrated load. The suggested pattern is shown in Figure 5-1. In addition to the fact that honeycomb-shaped structures allow for the minimization of the amount of material to reach minimal weight and minimal material cost, honeycomb-shaped structures also provide relatively high out-of-plane compression and high shear properties.

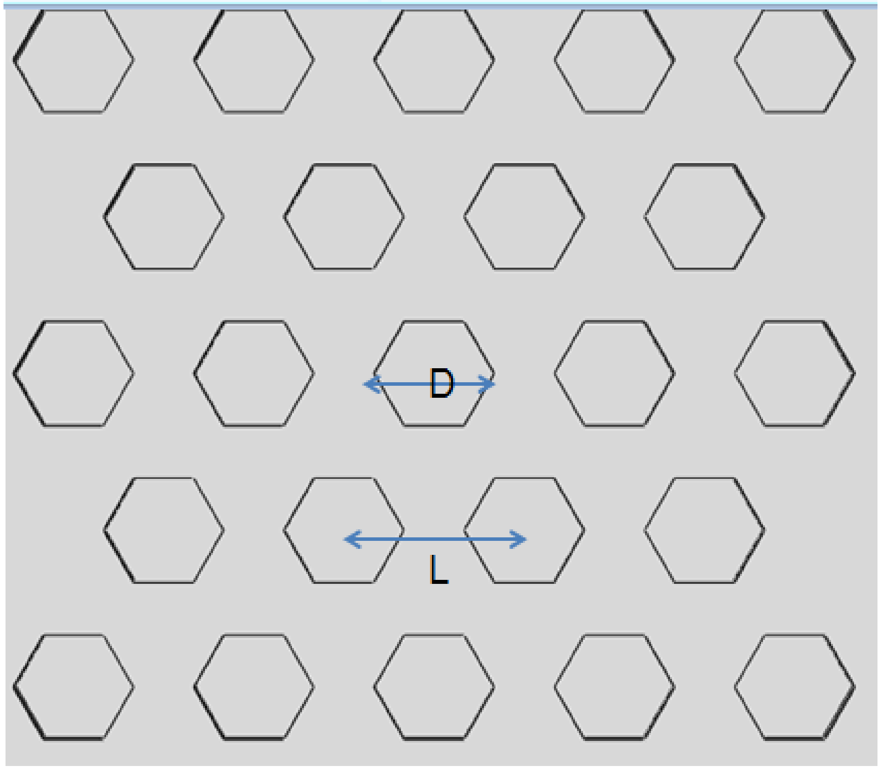

Figure 5-1: 2D Hexagonal Pattern Layout

Three parameters describe the hexagonal pattern: D, which is the hexagonal diameter (head to head); L, which is the distance between the centers of two neighboring hexagons; and t, the hexagon wall thickness. Three hexagonal diameters are investigated: 15μm, 20μm, and 40μm. Since we narrowed the optimum bracket for the surface texture density from Chapter 4 to range from 0.25 to 0.5, in this section, the recommended range is reinvestigated. In addition, the higher texture densities of 0.57 and 0.667 confirm the previously obtained results. Table 5-1 shows the different parameters of each sample.

Table 5-1: Dimensions of the Patterned Samples

Sample #	D(μm)	T(μm)	L(μm)	D/L
1	40	20	60	0.6667
2	40	40	80	0.5
3	40	60	100	0.4
4	40	120	160	0.25
5	20	60	80	0.25
6	20	30	50	0.4
12	20	20	40	0.5
13	20	15	35	0.577
8	15	15	30	0.5
9	15	7.5	22.5	0.667
10	15	22.5	37.5	0.4
11	15	45	60	0.25

5.2 Hexagonal Patterns Fabrication

5.2.1 Sample Preparation for Hexagonal Patterns

The samples were cut to a thickness of 3 mm and a width and length of 10 mm. Samples are ground by different silicon carbide grades then polished using a diamond paste of 9 μm and 3 μm, and then an Al_2O_3 suspension of 0.05μm.

5.2.2 Photolithography Process

Chemical etching and photolithography are used to create the hexagonal patterns. The steps of the pattern fabrication are synopsized in Figure 5-2.

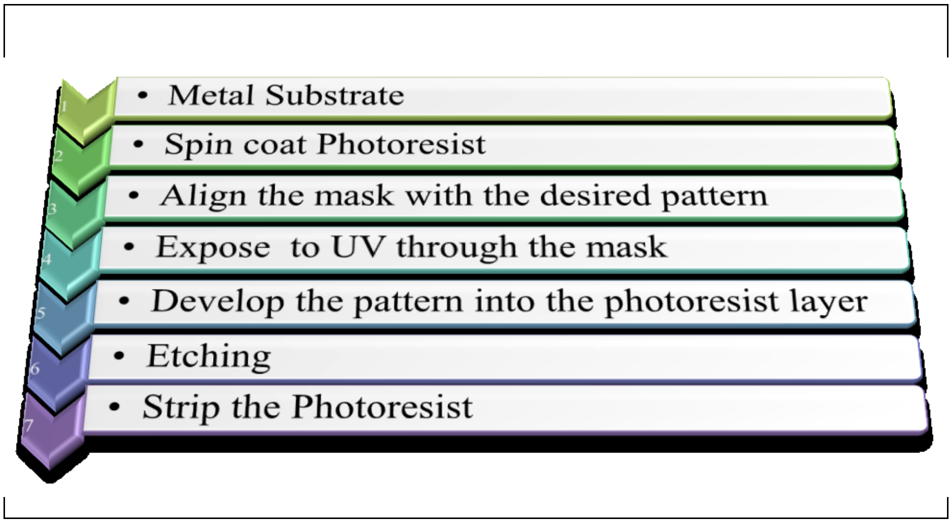

Figure 5-2: The Basic Steps for Photolithography Etching

Shipley 1805 photoresist is spun at 4000 rpm over the tool steel substrate to form a coating thickness of 0.5μm. The mask is then placed on top via a Karl Suss mask aligner. The coated samples are then exposed to light of 105 mJ/cm2 of wavelength of 405 nm for 90 seconds to be developed. The isotropic etchant FeCl3 is used for 10 seconds at 40ºC.

The pattern's dimensions are checked and the sizes are conformed with the design with a tolerance of ±3μm.

5.2.3 Challenges of Photolithography

For the diameters of 15 μm and 20μm, the sharp corners of the hexagons are rounded due to the undercut phenomenon, which appears as a result of either over-etching or using isotropic etching. In the current case, the undercut occurs due to isotropic etching. In Figure 5-3, the undercut is shown as a rounded edge instead of a sharp edge.

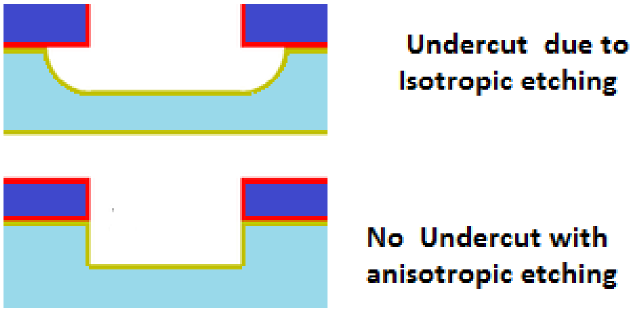

Figure 5-3: Undercut Challenge with Small Diameters

5.3 Tribological Tests for Hexagonal Patterns

The same scratch tester that was used with the circular pattern is used to measure the coefficient of friction for the hexagonal patterned samples. The same loading conditions are used. A scratch length of 500 μm, and indenter speed of 500 μm /min at constant load of 7N is used The indenter is made of diamond and the diamond tip has a radius of 200 μm.

Five scratches were made per each patterned sample and a plain reference sample as well. Three horizontal scratches and two vertical stretches are made. The orientation of the vertical and horizontal scratches with respect to the pattern is shown in Figure 5-4. A constant normal load of 7 N is applied. The instantaneous tangential and normal forces are recorded at an interval of one micrometer. The penetration depth is recorded as well. The average coefficient of friction resulting from the three scratches is calculated for each sample with a maximum standard deviation of 3.0%.

A scanning electron microscope is utilized to take magnified micrographs of the scratches in order to investigate the patterned samples and the impact on the coefficient of friction. EDS is then made to investigate the chemistry of the patterned spots versus the unpatented surface because there is a chemical change involved in chemical etching.

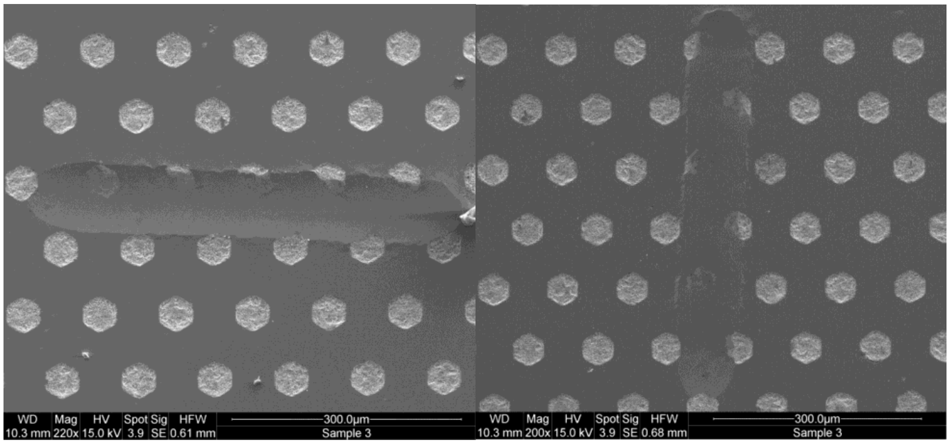

(a) (b)

Figure 5-4: Alignment of a Horizontal Scratch in (a) and Vertical Scratch in(b).

5.4 Results and Analysis of the Hexagonal Patterns

Unexpectedly, the plain sample has the lower coefficient of friction compared to all hexagonal patterned samples, which contradicts the previous results obtained from laser patterned surfaces, as well as the numerical models. Thorough investigation of the surface morphology was done, which will be discussed in section 5.4.5. In the next section, the effect of the texturing parameters on the coefficient of friction is investigated, and it is compared with a plain etched sample.

5.4.1 Micrographs of the Hexagonal Textured Samples

Scanning electron microscope micrographs for horizontal and vertical scratches, in addition to micrographs taken by the scratch tester during the test, and finally 3D profilometer images that capture closely the depth and the topography of the scratch, are depicted in Figures 5.5 to 5.16.Two observations are noticed. First, for hexagon diameters of 20μm and 15μm, the sharp corners of the hexagonal patterns are rounded. Second, the roughness of most textured samples before the scratch test ranges between 2μm to 5μm except for samples # 1D40L60 and #13D20L35, which have high roughness of 7μm as shown in WYKO pictures.

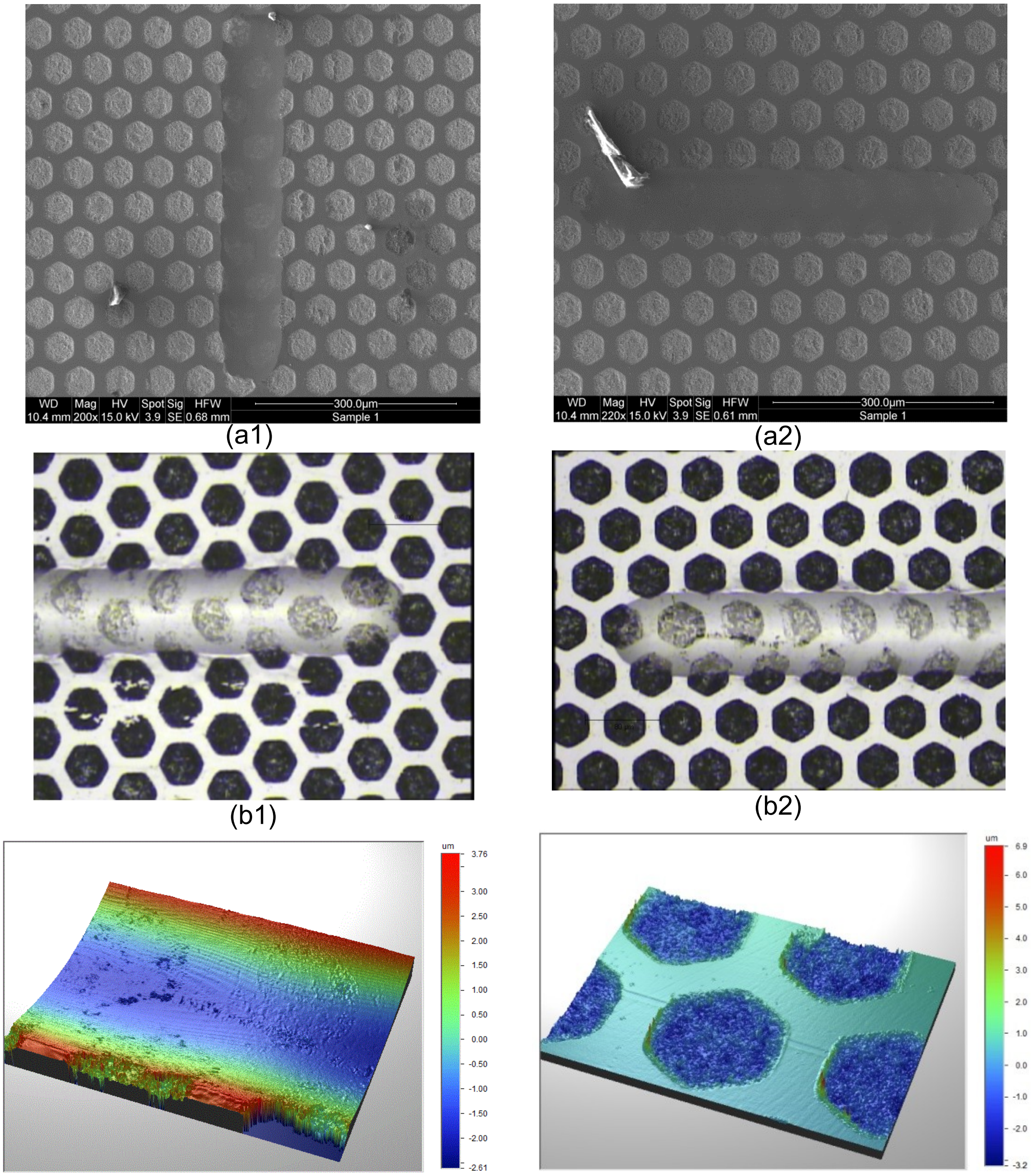

(a1) (a2)

(b1) (b2)

(c1) (c2)

Figure 5-5: Sample# 1 D40L60 SEM Pictures for vertical scratch in (a1) and horizontal scratch in (a2). Scratch tester Integrated Microscopic pictures for vertical scratch in (b1) and horizontal scratch in (b2). 3D Profilometer Images for Scratched Path in(c1) and Unscratched sample in (c2).

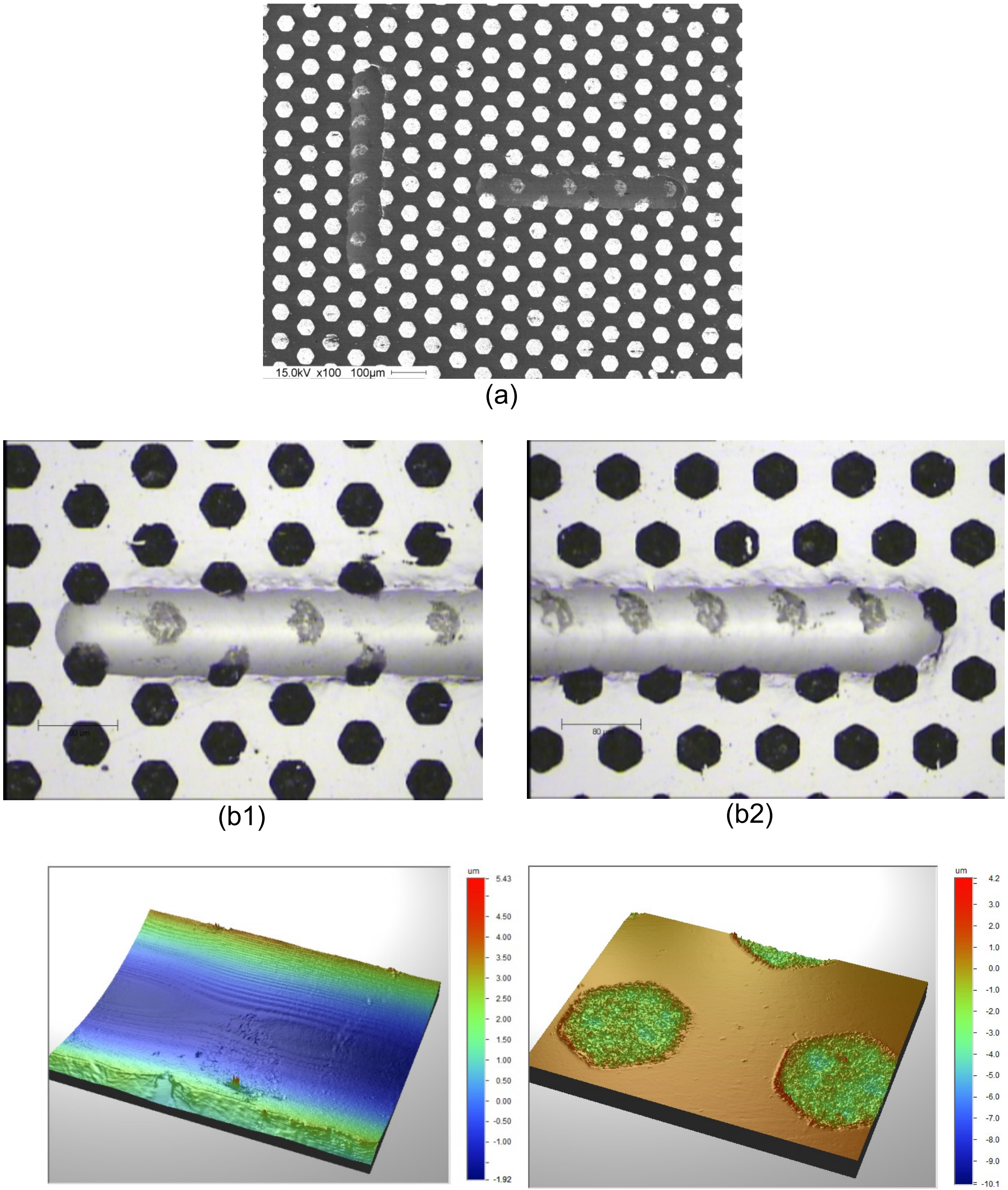

(a)

(b1) (b2)

(c1) (c2)

Figure 5-6: Sample#2 D40L80 SEM Pictures for vertical scratch and horizontal scratch in (a). Scratch tester Integrated Microscopic pictures for vertical scratch in (b1) and horizontal scratch in (b2). 3D Profilometer images for Scratched path in(c1) and unscratched sample in (c2).

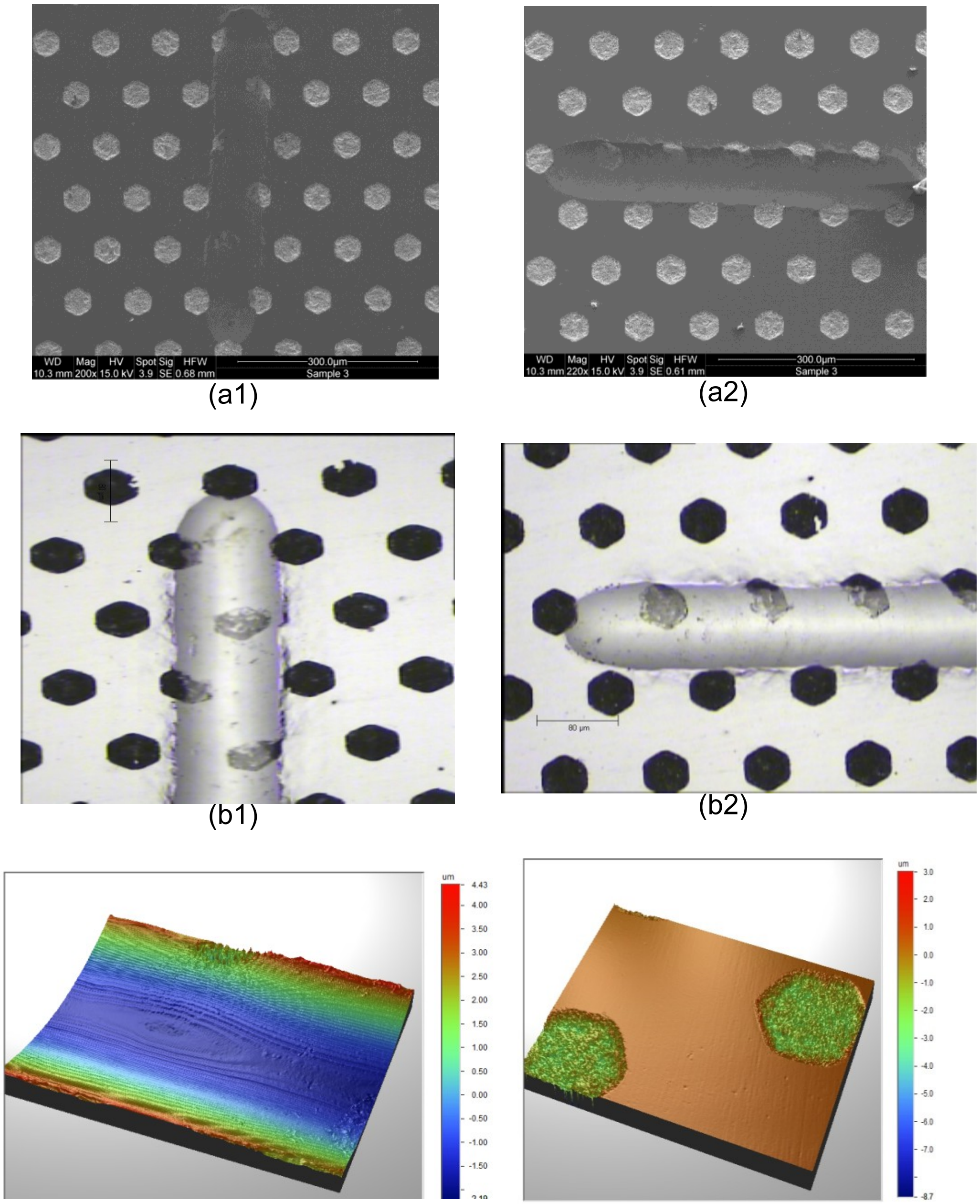

(a1) (a2)

(b1) (b2)

(c1) (c2)

Figure 5-7: Sample#3 D40L100 SEM Pictures for vertical scratch in (a1) and horizontal scratch in (a2). Scratch tester Integrated Microscopic pictures for vertical scratch in (b1) and horizontal scratch in (b2). 3D Profilometer images for Scratched path in (c1) and unscratched sample in(c2).

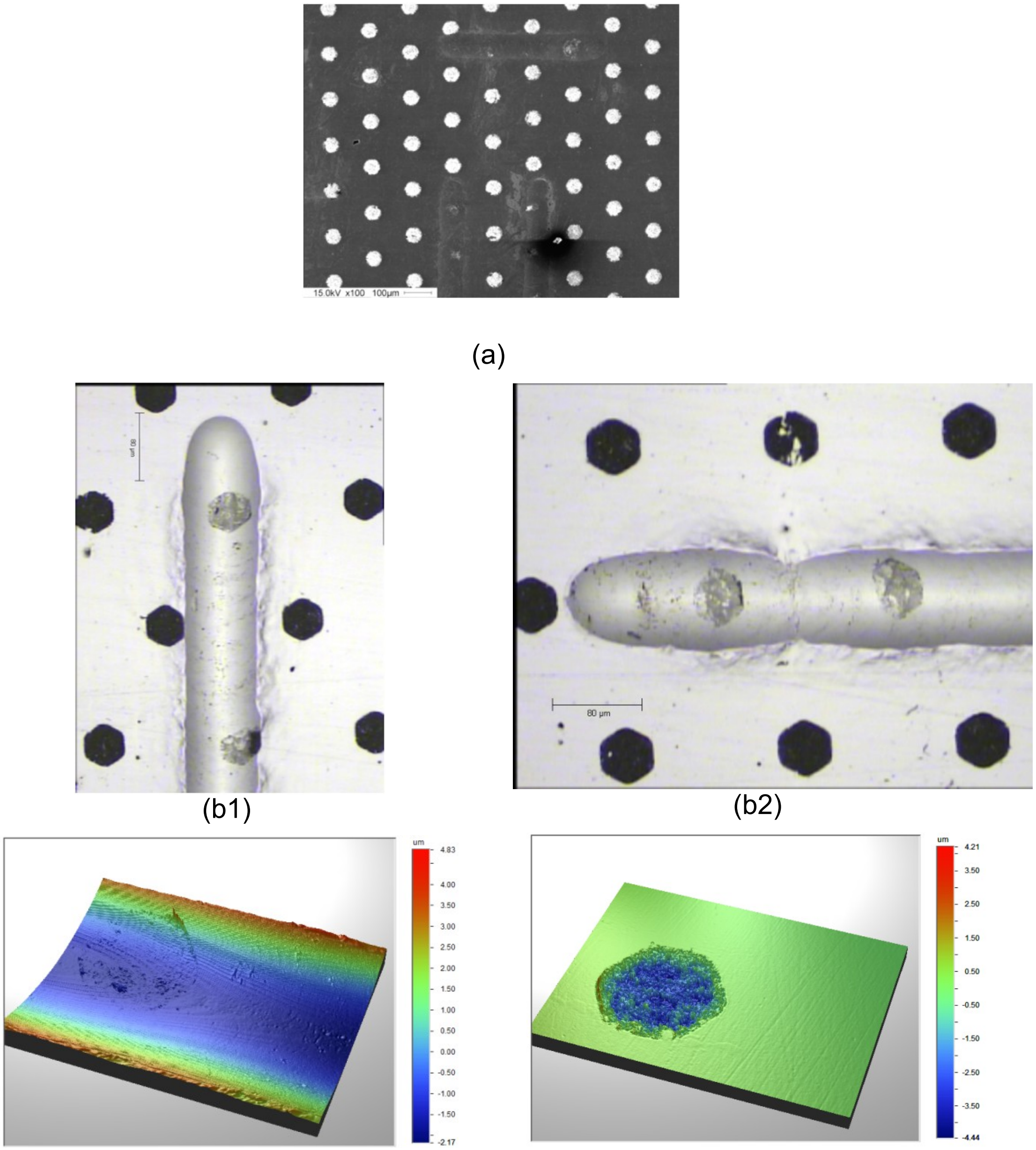

(a)

(b1) (b2)

(c1) (c2)

Figure 5-8: Sample#4 D40L160 SEM Pictures for vertical scratch and horizontal scratch in (a). Scratch tester Integrated Microscopic pictures for vertical scratch in(b1) and horizontal scratch in (b2). 3D Profilometer images for Scratched path in (c1) and unscratched sample in (c2).

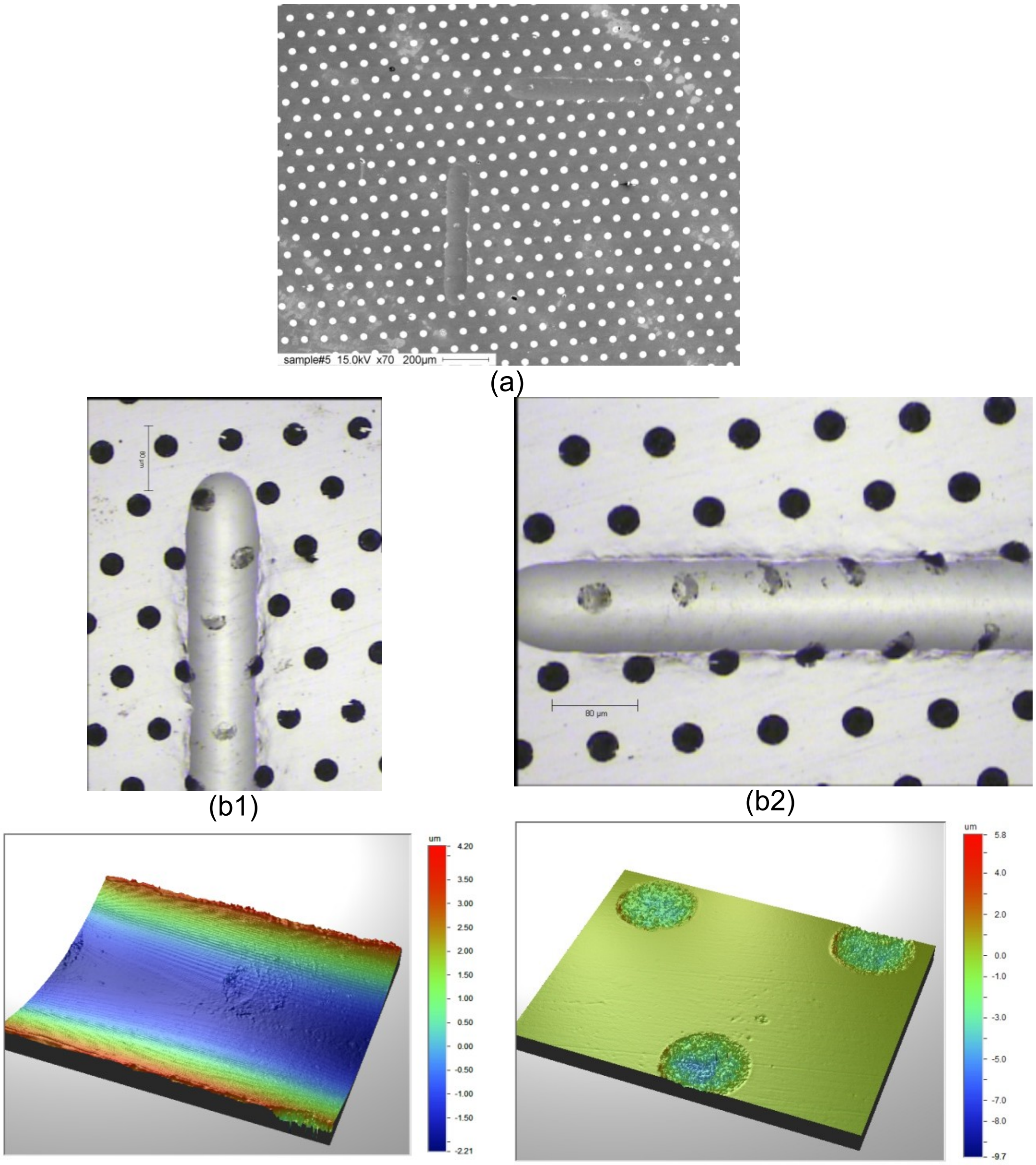

(a)

(b1)

(b2)

(c1)

(c2)

Figure 5-9: Sample#5 D20L80 SEM Pictures for vertical scratch and horizontal scratch in (a). Scratch tester Integrated Microscopic pictures for vertical scratch in (b1) and horizontal scratch in (b2). 3D Profilometer images for Scratched path in (c1) and unscratched sample in (c2).

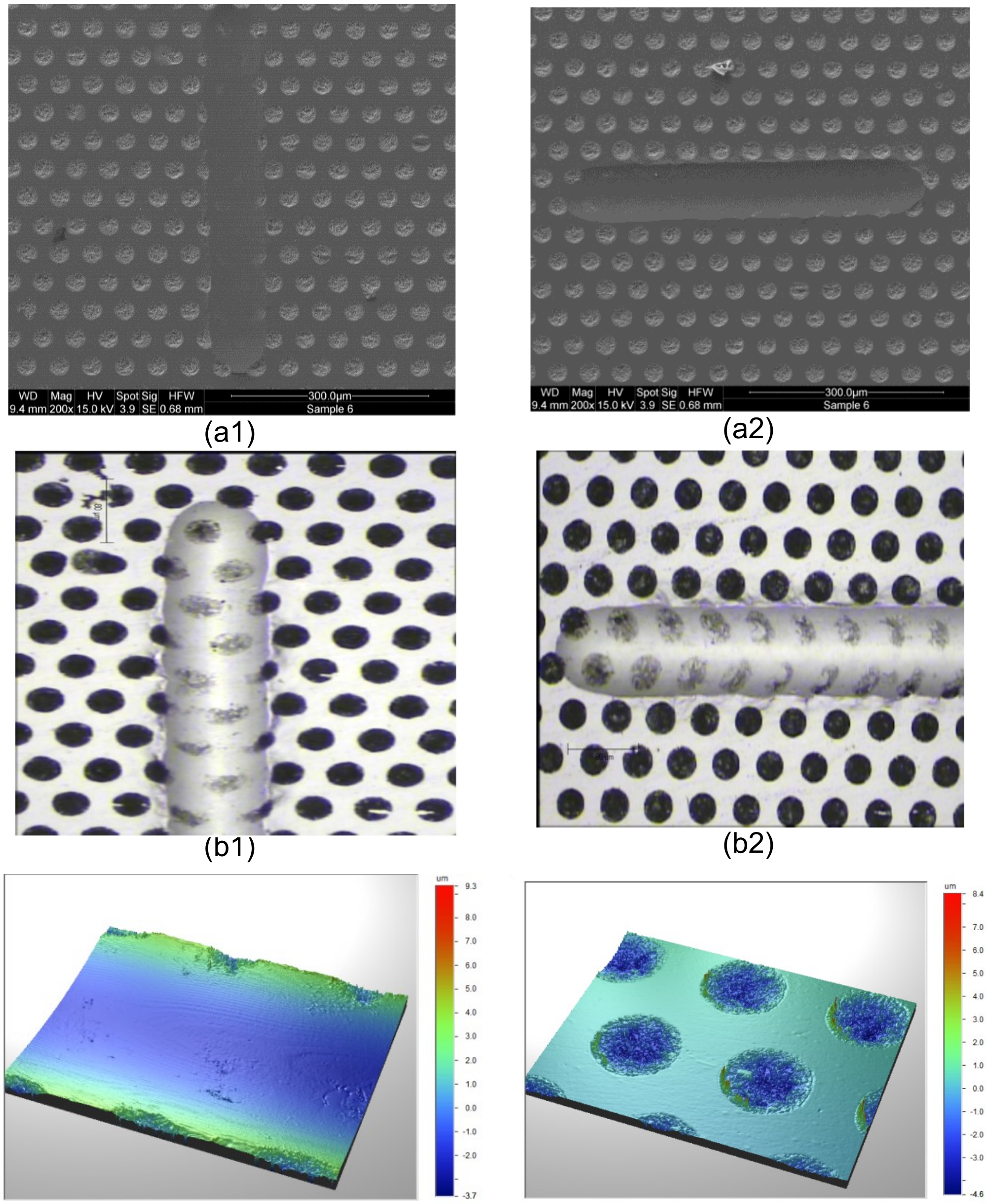

(a1) (a2)

(b1) (b2)

(c1) (c2)

Figure 5-10: Sample#6 D20L50 SEM Pictures for vertical scratch in (a1) and horizontal scratch in (a2). Scratch tester Integrated Microscopic pictures for vertical scratch in (b1) and horizontal scratch in (b2). 3D Profilometer images for Scratched path in (c1) and unscratched sample in (c2).

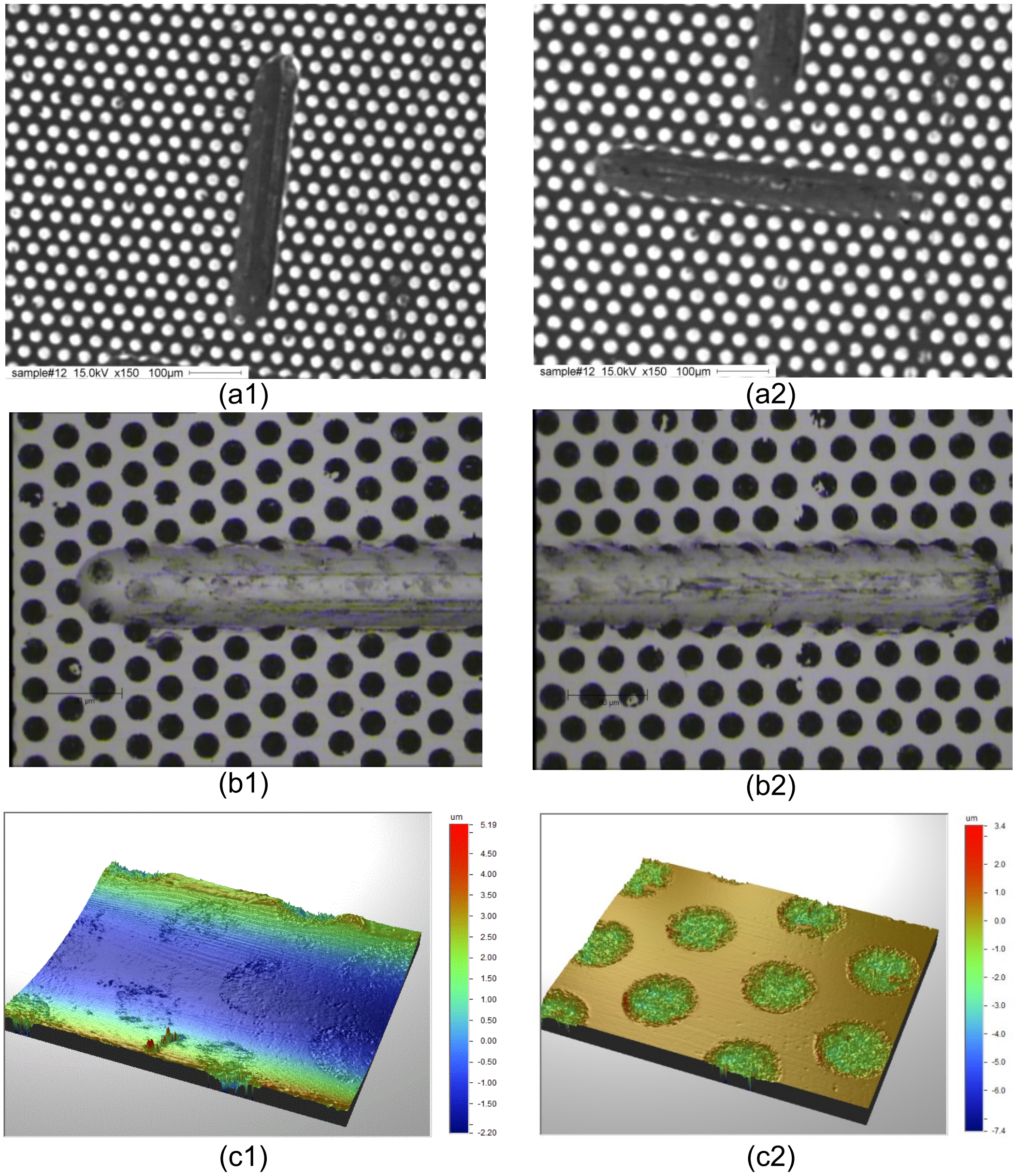

(a1) (a2)

(b1) (b2)

(c1) (c2)

Figure 5-11: Sample #12 D20L40 SEM Pictures for vertical scratch in (a1) and horizontal scratch in (a2). Scratch tester Integrated Microscopic pictures for vertical scratch in (b1) and horizontal scratch in (b2). 3D Profilometer images for Scratched path in (c1) and unscratched sample in (c2).

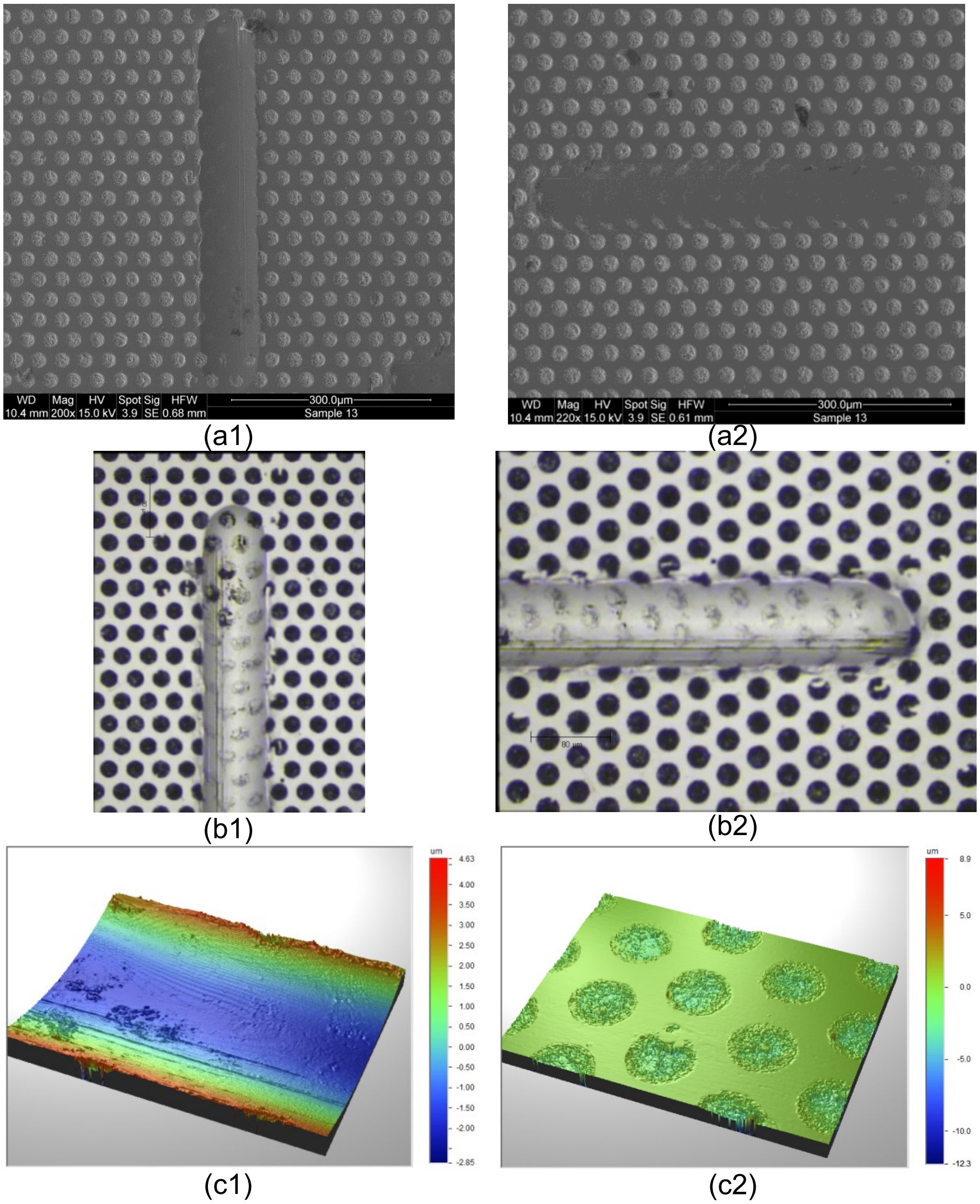

(a1) (a2)

(b1) (b2)

(c1) (c2)

Figure 5-12: Sample #13 D20L35 SEM Pictures for vertical scratch in (a1) and horizontal scratch in (a2). Scratch tester Integrated Microscopic pictures for vertical scratch in (b1) and horizontal scratch in (b2). 3D Profilometer images for Scratched path in (c1) and unscratched sample in(c2).

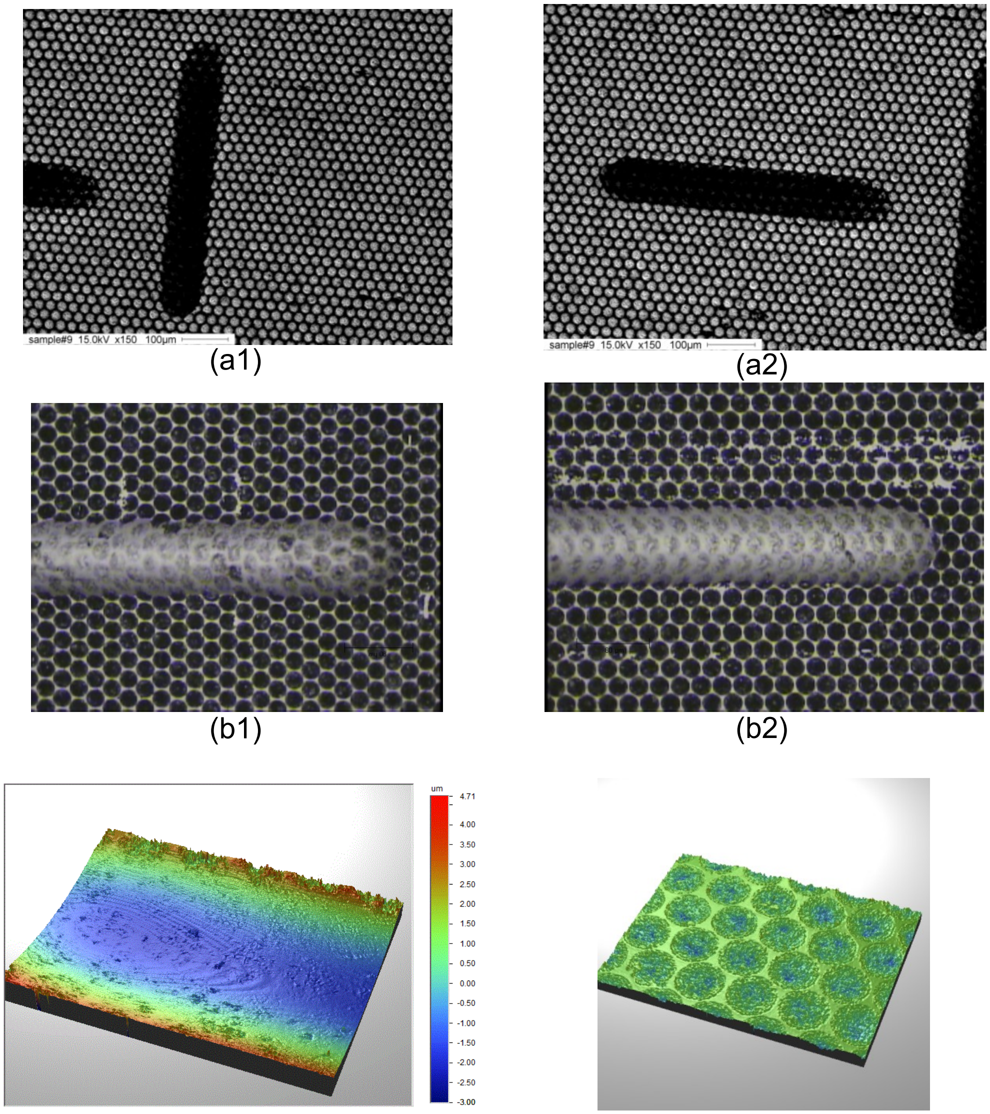

(a1) (a2)

(b1) (b2)

(c1) (c2)

Figure 5-13: Sample #9 D15L22.5 SEM Pictures for vertical scratch in (a1) and horizontal scratch in (a2). Scratch tester Integrated Microscopic pictures for vertical scratch in (b1) and horizontal scratch in (b2). 3D Profilometer images for Scratched path in (c1) and unscratched sample in(c2).

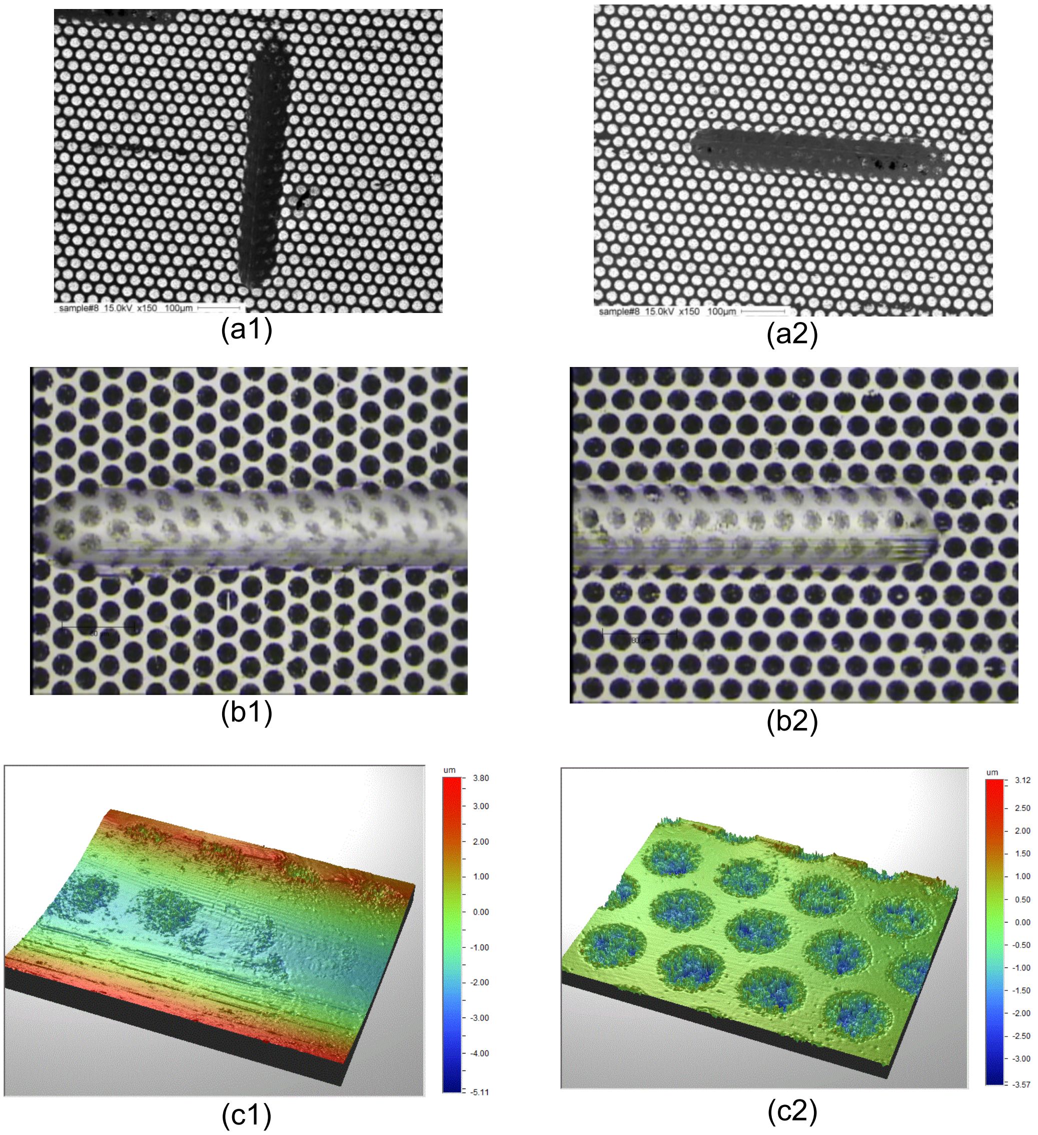

Figure 5-14: Sample #8 D15L30 SEM Pictures for vertical scratch in (a1) and horizontal scratch in (a2). Scratch tester Integrated Microscopic pictures for vertical scratch in (b1) and horizontal scratch in (b2). 3DProfilometer images for Scratched path in (c1) and unscratched sample in (c2).

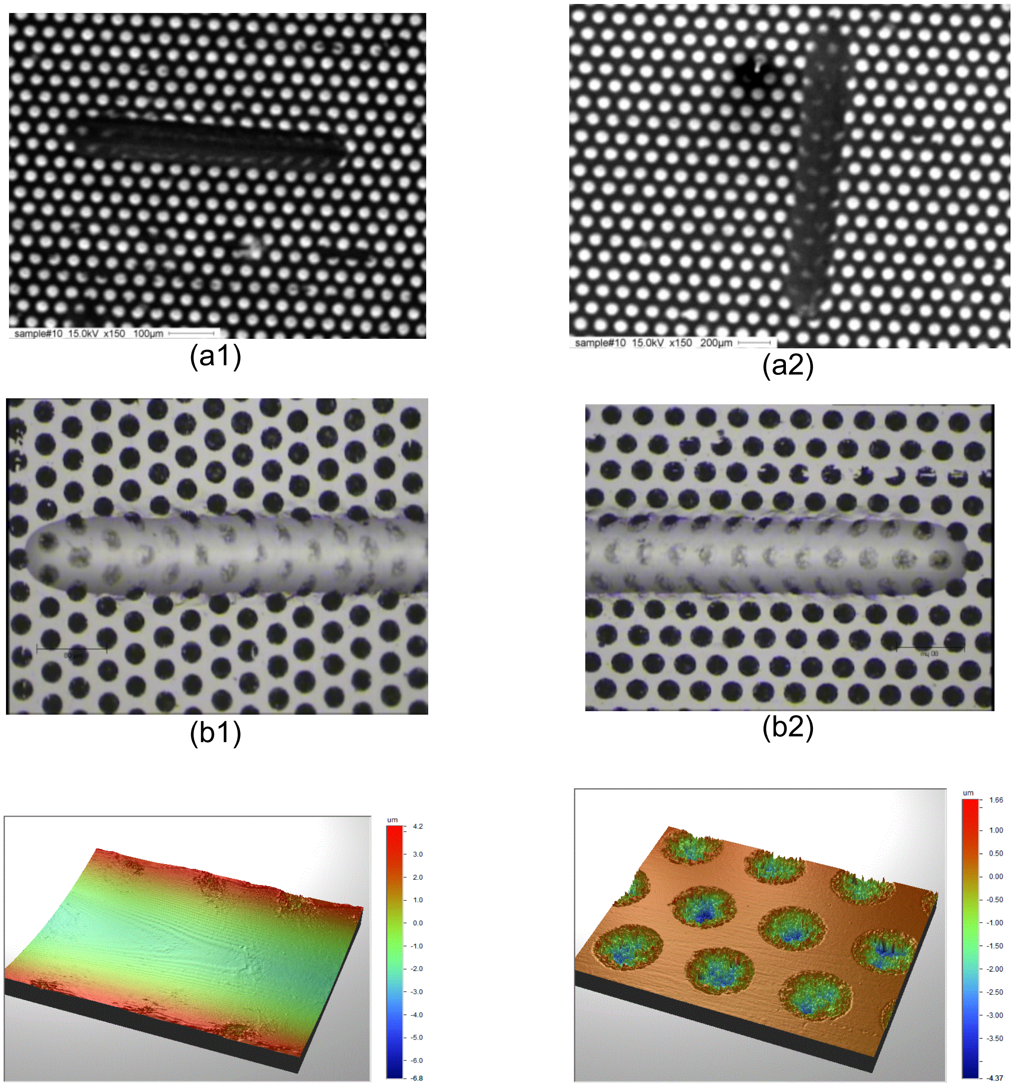

(a1) (a2)

(b1) (b2)

(c1) (c2)

Figure 5-15: Sample #10 D15L37.5 SEM Pictures for vertical scratch in (a1) and horizontal scratch in (a2). Scratch tester Integrated Microscopic pictures for vertical scratch in (b1) and horizontal scratch in (b2). 3 D Profilometer images for Scratched path in (c1) and unscratched sample in (c2).

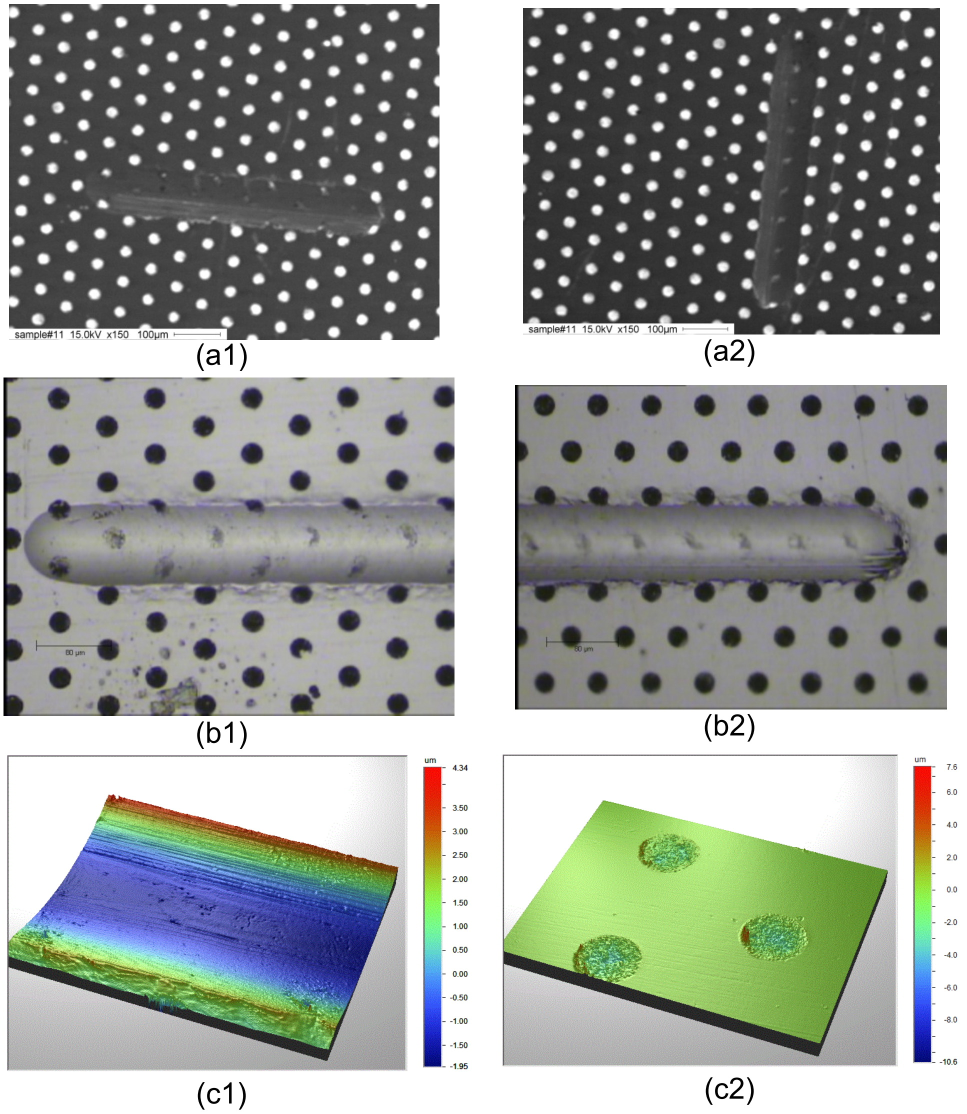

Figure 5-16: Sample #11 D15L60 Pictures for vertical scratch in (a1) and horizontal scratch in (a2). Scratch tester Integrated Microscopic pictures for vertical scratch in (b1) and horizontal scratch in (b2).3D Profilometer images for Scratched path in (c1) and unscratched sample in (c2).

5.4.2 COF and PD vs. the Sliding Distance of Hexagonal Patterns

When friction coefficients are plotted versus the sliding distance as shown in Figure 5-17 to Figure 5-19, fluctuations in the coefficients of friction appear as a result of texturing. The bumps in the coefficient of friction curve correspond to the contact between the rigid indenter and un-textured areas while the valleys correspond to the recessed areas. The small-scale zigzag is due to the surface roughness.

The average penetration depth ranges between 1.8 μm to 6.5 μm. It is obvious that the penetration depth follows the same fluctuations as the coefficients of friction. Besides, the penetration depth is found to be decreasing with the decrease of spatial texture densities.

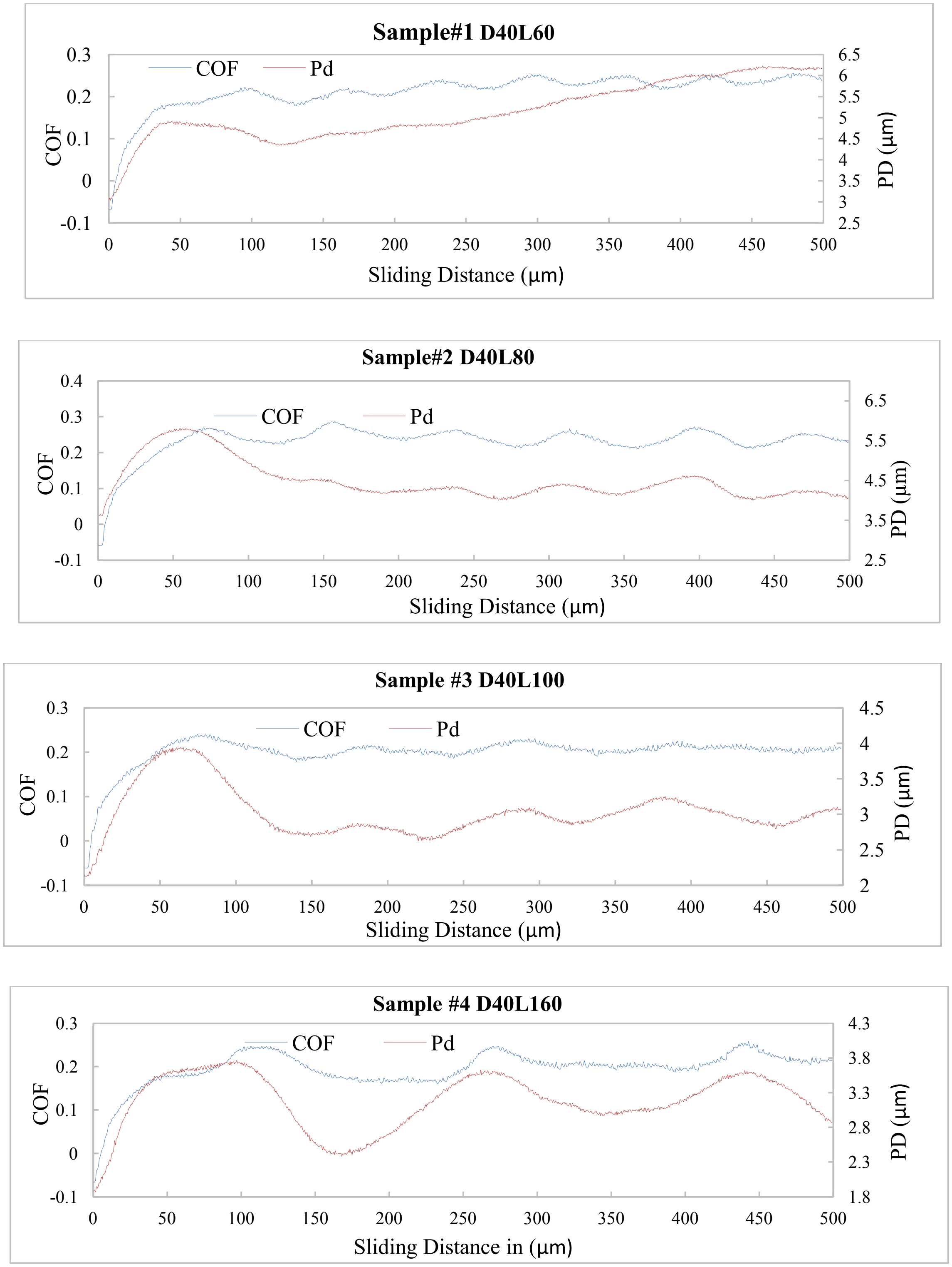

Figure 5-17: Coefficients of Friction and Penetration Depth(PD) for Diameter 40 µm

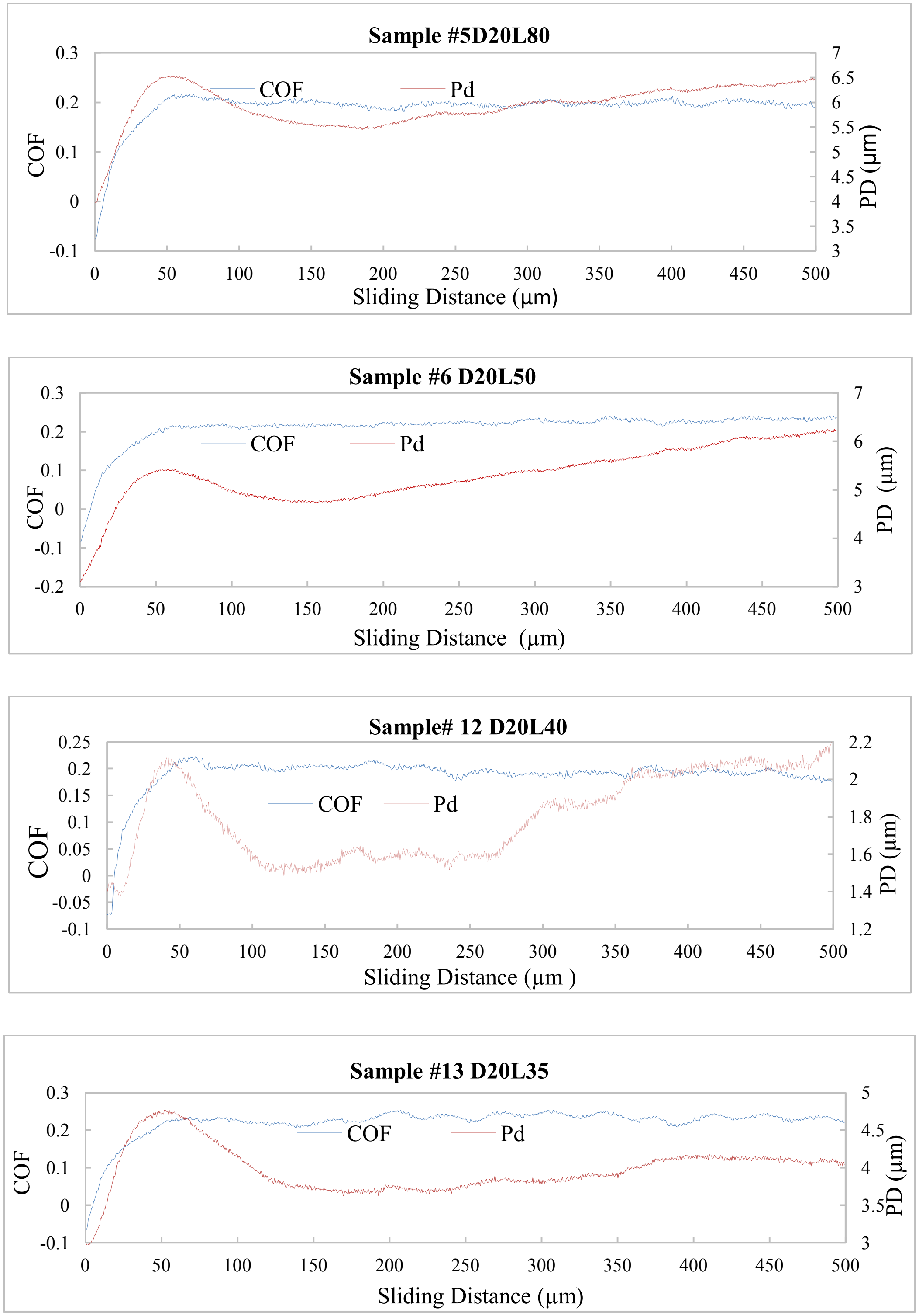

Figure 5-18: Coefficients of Friction and Penetration Depth for Diameter 20 µm

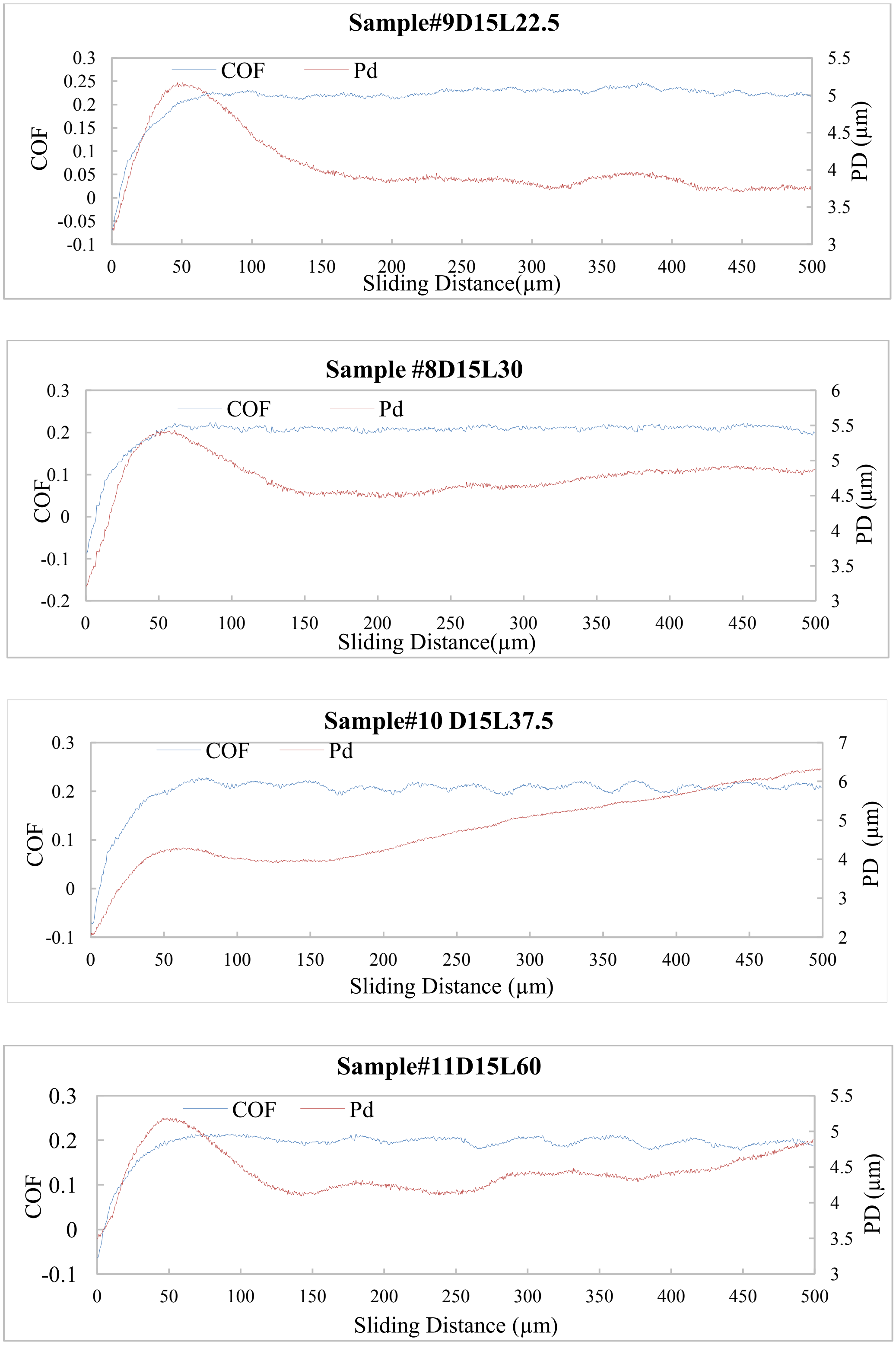

Figure 5-19: Coefficients of Friction and Penetration Depth (PD) for Diameter15 µm

5.4.3 The Effect of Texturing Parameters on COF

There is no explicit trend observed between the coefficients of friction and the hexagonal diameters (D). On the other hand, when the coefficients of friction are plotted versus the spatial texture densities for different diameters as depicted in Figure 5-20, it is observed that for the hexagonal diameters of 15μm and 40μm, the minimum coefficients of friction are obtained at a spatial texture density of 0.25. But, for a diameter of 20 μm, the minimum coefficient of friction is found at the spatial texture density of 0.5. Whilst spatial texture density is greater than 0.5, an abrupt increase in the coefficient of friction is noticed. The latter observation is noticed with all hexagonal and circular diameters as well.

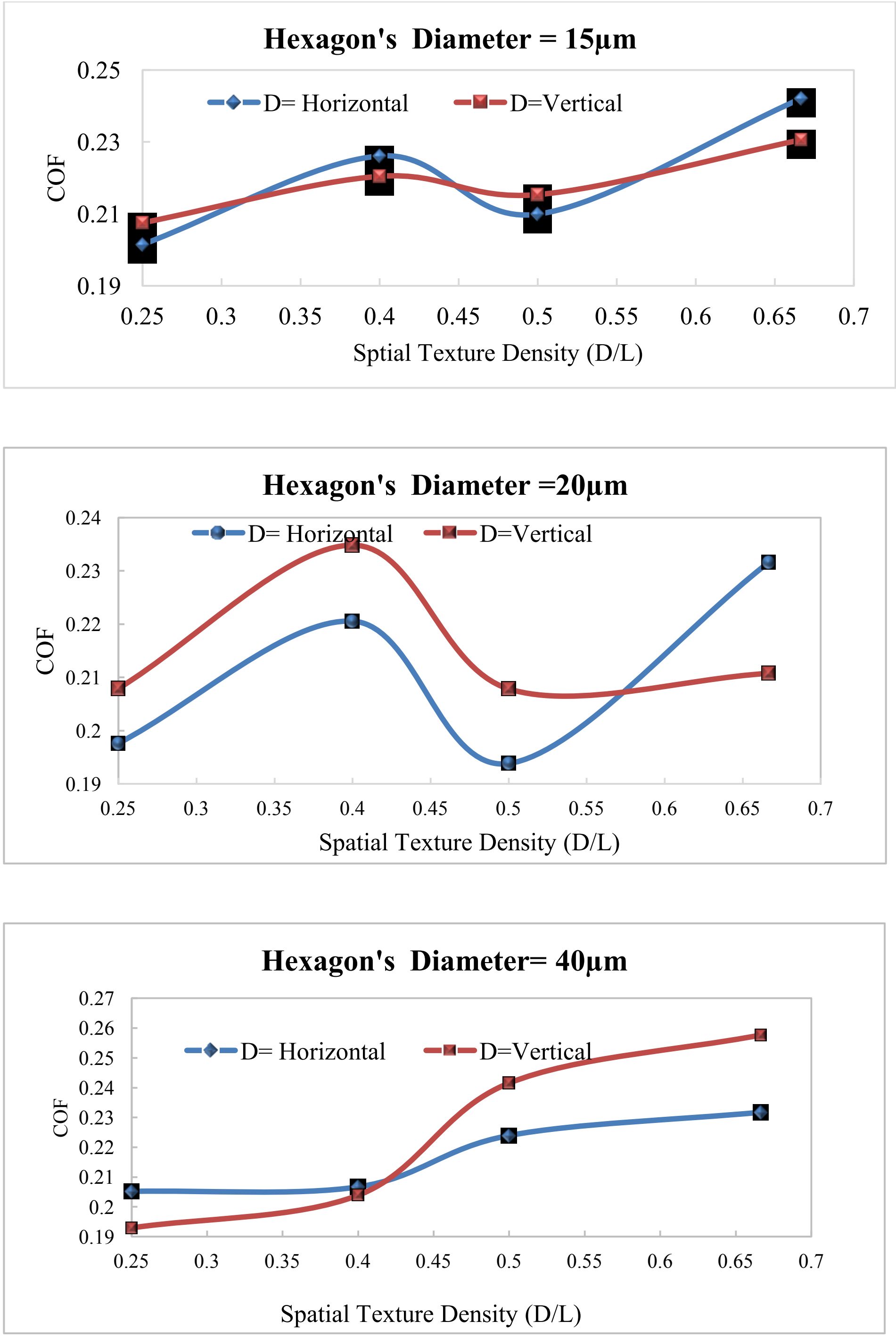

Figure 5-20: Coefficients of Friction for the Three Hexagonal Diameters vs. the Spatial Texture Densities

In Figure 5-21, the average coefficients of friction of three different hexagonal diameters are plotted versus the spatial texture densities. The average coefficient of friction of the plain etched sample is plotted as well at a spatial texture density equal to zero. A 28% reduction in coefficient of friction is achieved at a spatial texture density of 0.5 and a hexagonal diameter of 20 μm. It is worth mentioning that the maximum reduction in coefficient of friction, which is obtained with the circular patterning, has exactly the same texturing parameters as the hexagonal pattern. The coefficients of friction of the hexagonal diameters 15 μm and 20 μm follow the same trend. For the hexagonal diameters of 15 μm and 40 μm, the minimum coefficient of friction occurs at the spatial texturing density of 0.25. Although the minimum coefficient of friction does not fall at the spatial texture density of 0.4, a considerable reduction in coefficient of friction still occurs at this spatial texture density with all hexagonal diameters. The behavior of a hexagonal diameter of 40 μm is quite different. There is no explicit minimum as the coefficient of friction increases smoothly with the increase of spatial texture densities, yet an abrupt increase is observed when the spatial texture density is larger than 0.5.

When the spatial texture density increases beyond 0.5, the coefficient of friction increases with all hexagonal diameters.

Recalling Figure 5-22, coefficients of friction versus the spatial texture densities of circular patterns, the behaviour is very similar to the hexagonal patterns. The minimum coefficients of friction for both shapes occur at the same texturing parameters: The spatial texture density of 0.5 , the dimple diameter of 20μm and the distance between the dimples (L) is 40 μm.

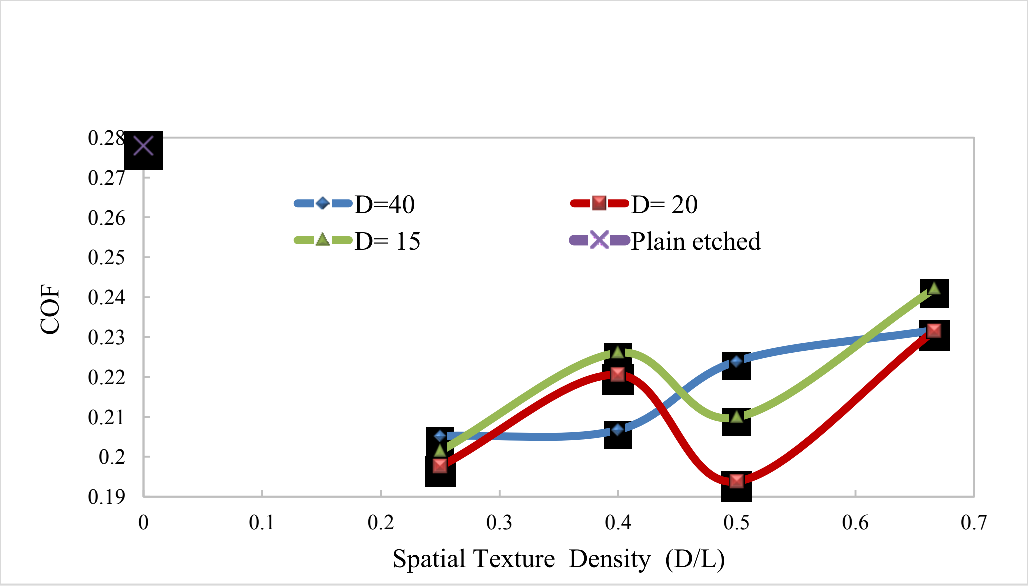

Figure 5-21: The Coefficients of Friction vs. the Spatial Texture Densities for Horizontal Scratches of the Hexagonal Patterns

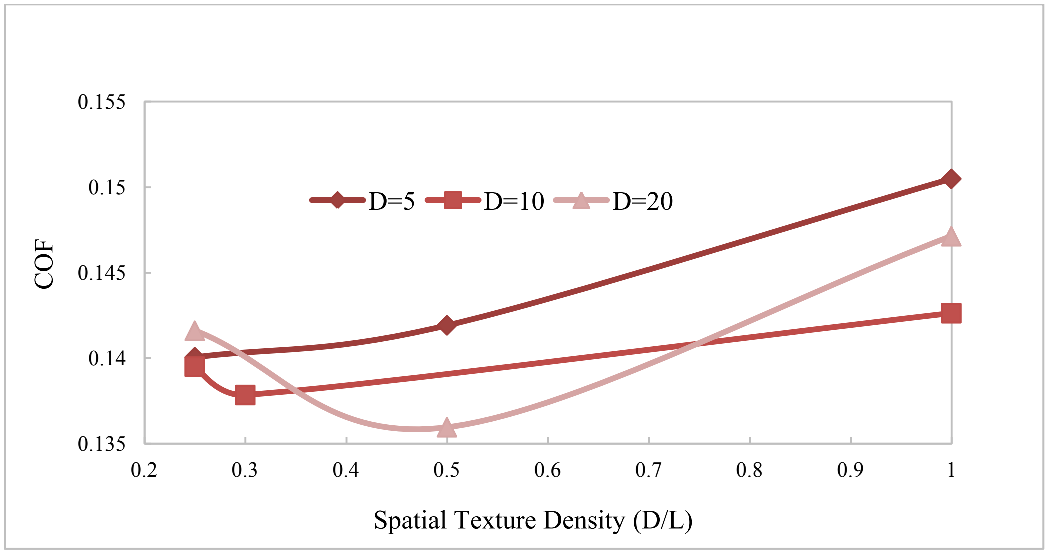

Figure 5-22: Coefficients of Friction vs. the Spatial Texture Densities for Circular Patterns

5.4.4 The Patterns Anisotropy

The friction coefficients that result from the vertical scratches follow the same trend as the horizontal scratches as shown in Figure 5-23. The difference between horizontal and vertical scratch is the distance between the centers of the two consecutive craters, L_v. This distance increases by $\sqrt{3}$, and consequently, the spatial texture density decreases by $\sqrt{3}$. As a result, the spatial texture densities in the vertical direction change from 0.14 to 0.39. The problem is with the spatial texture density of 0.14, which falls outside the minimum bracket. This observation is shown in Figure 5-20 where the friction coefficients corresponding to the vertical scratches are higher than those belonging to the horizontal scratches at the spatial texture density of 0.25. The opposite behavior is observed at a spatial texture density of 0.67. A hexagonal diameter of 40 μm does not follow this remark.

Figure 5-24 and Table 5-2 show the difference between friction coefficients for the horizontal and vertical scratches and the reduction percentage for each sample. Although the hexagonal layout of the pattern has an anisotropic characteristic, the difference is still less than 3%.

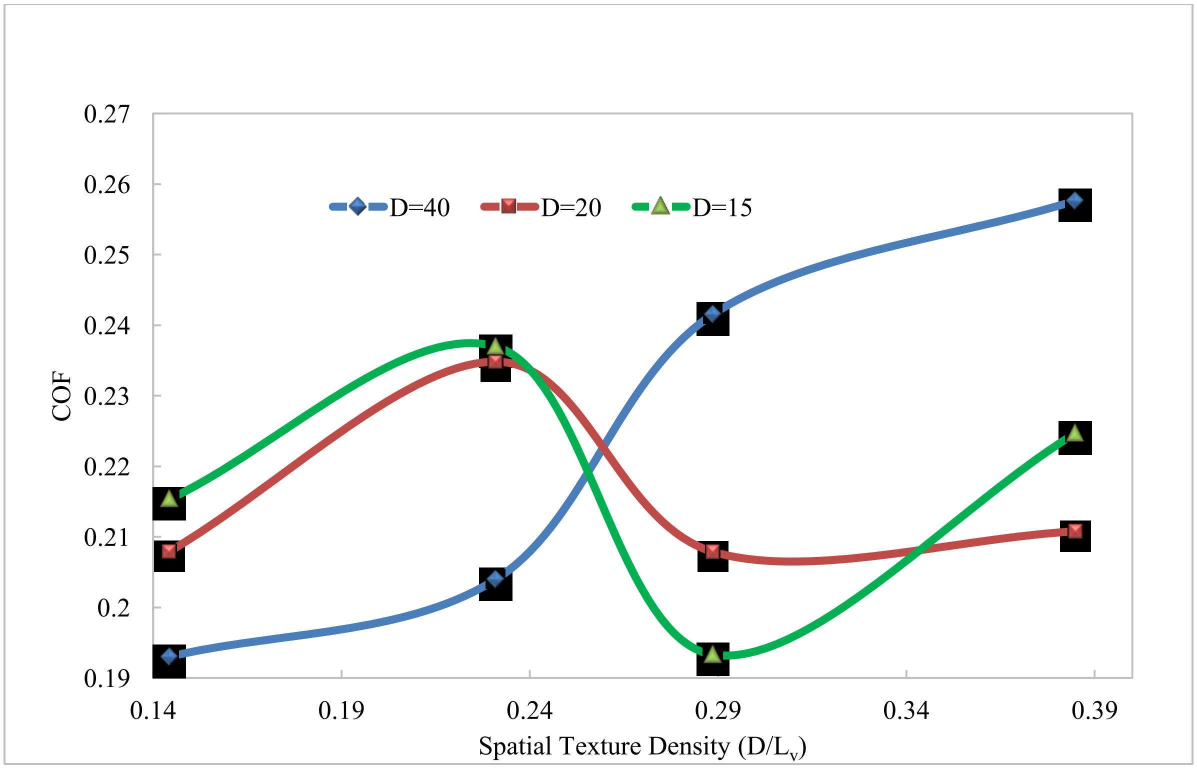

Figure 5-23: Coefficients of Friction vs. Texture Densities for the Vertical Scratches

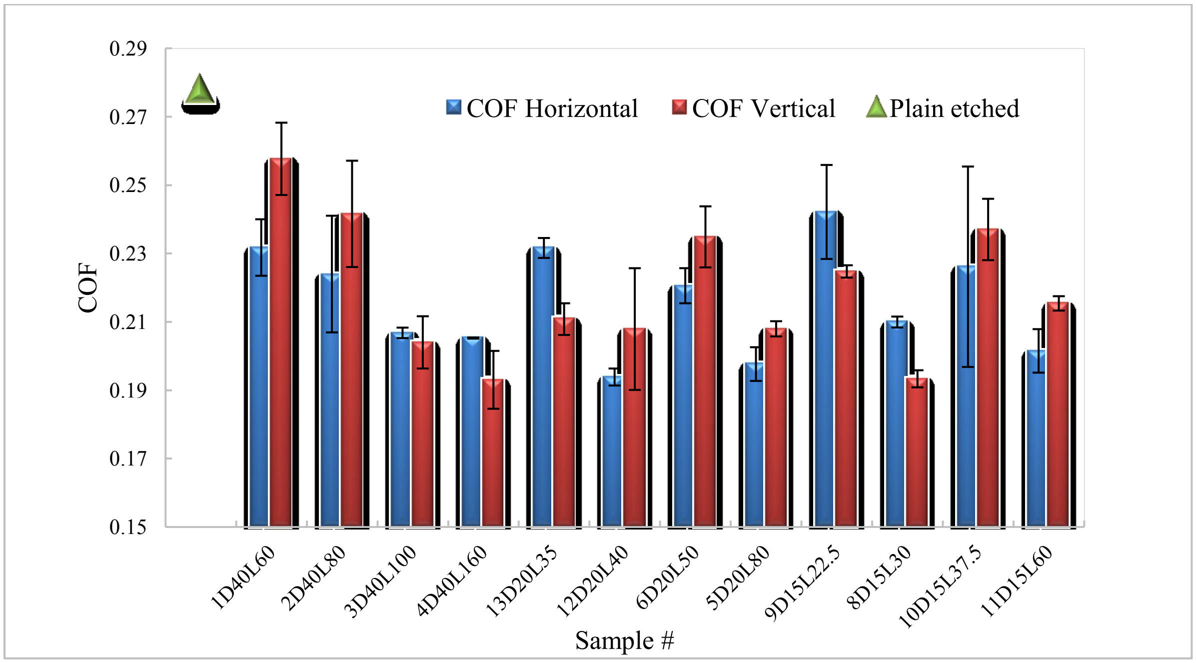

Figure 5-24: The Coefficients of Friction for Horizontal and Vertical Scratches and the Plain Etched Sample

Sample #	**1D40 L60**	**2D40 L80**	**3D40 L100**	**4D40 L160**	**5D20 L80**	**6D20 L50**	**8D15 L30**	**D15 L22.5**	**10D15 L37.5**	**11D15 L60**	**12D20 L40**	**13D20 L35**
D/L	.667	0.5	0.4	0.25	0.25	0.4	0.5	.667	0.4	0.25	0.5	0.577
COF (H)	.226	.212	.205	.205	.197	.216	.209	.226	.20	.197	.195	.231
% Red	16.34	21.52	23.85	23.94	26.99	19.96	22.28	16.18	22.67	26.93	27.82	14.15
COF (V)	.27	.22	.20	.19	.21	.23	.22	.23	.22	.21	.19	.23
% Red	1.8	19.2	24.5	28.9	22.5	15.4	20.2	14.5	18.3	23.1	28.5	16.3

Table 5-2: Summary of the Coefficients of Friction for the Hexagonal Patterns with the Reduction %

5.4.5 Un-textured Sample vs. Textured Samples of Hexagonal Patterns

As it was mentioned earlier, the coefficient of friction of the plain sample is lower than all textured samples, which contradicts with what was concluded in the numerical models and circular patterns which are fabricated by laser ablation.

A thorough investigation was conducted in order to explain this phenomenon. Energy dispersive spectroscopy (EDS) was done to check the chemical characterization of the samples at different spots: the unscratched textured spot, the unscratched plain spot, the scratched textured spot, and finally the scratched plain spot.

In the first spot depicted in Figure 5-25 (patterned and unscratched), the chromium weight content is about 20% and the iron content is 60%. In the second spot (un-patterned and un-scratched), as shown in

Figure 5-26, the chromium content is only 5% and the iron content is 85.5%. The third and fourth spots are inside the scratched area. The third spot is shown in Figure 5-27, where the chromium content decreases to 15% and iron increases to 67%. The fourth spot, which is shown in Figure 5-28, is inside the scratch path but not textured, and the iron content is at its highest value of 86%, while the Cr % is at lowest value of 4.5%.

These observations are explained as follows. During the chemical etching step, the chemical morphology of the surface has been changed due to the fast dissolution of the iron molecules, resulting in a high concentration of chromium, which in essence, exceeds the favorable limit, which is less than 15% in weight as suggested by Miyoshi and Buckley [118] who examined the effect of chromium content on the coefficient of friction. They concluded that when the chromium weight percentage in iron as an alloying element exceeds a certain limit, the coefficient of friction increases at least one order of magnitude as shown in Figure 5-29.

In our case, the unpatterned spots within the scratched area have the highest iron content and the lowest chromium content due to the plowing of an iron transfer layer. Whereas the patterned spots outside the scratch region have the highest chromium content, this justifies why the patterned surfaces have higher friction coefficients than the plain surface.

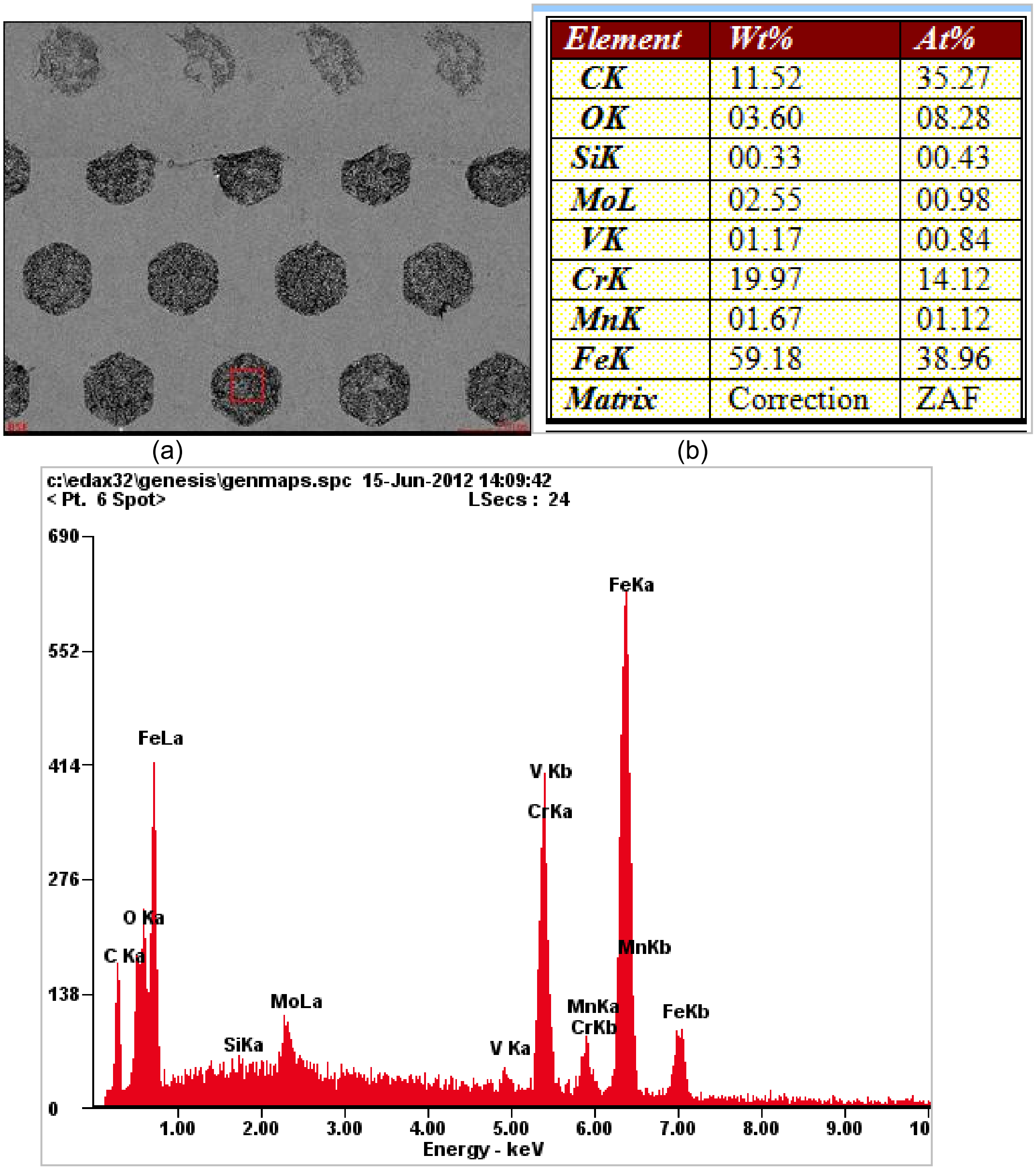

(a) (b)

Element	Wt%	At%
CK	11.52	35.27
OK	03.60	08.28
SiK	00.33	00.43
MoL	02.55	00.98
VK	01.17	00.84
CrK	19.97	14.12
MnK	01.67	01.12
FeK	59.18	38.96
Matrix	Correction	ZAF

(c)

Figure 5-25: First Spot – Textured and Non-Scratched Spot. (a) SEM Picture with a Square of the Examined Spot. (b) The Material Compositions of the Squared Spot. (c) EDS Spectra of the Squared Spot.

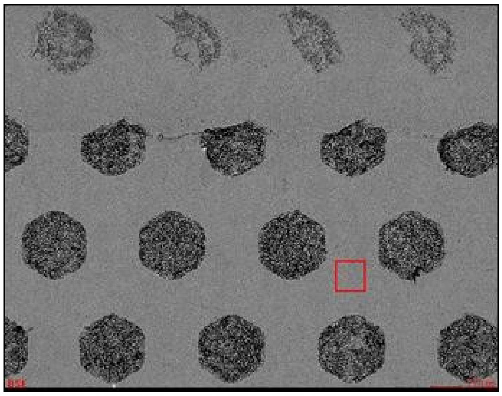

(a)

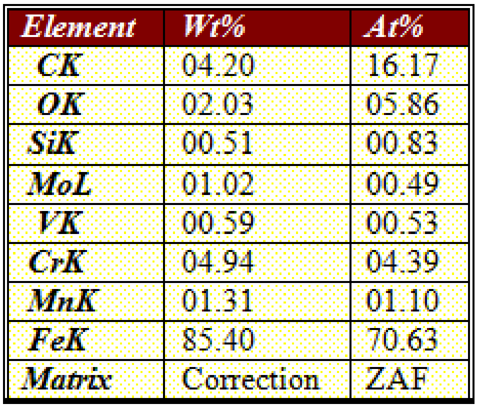

Element	Wt%	At%
CK	04.20	16.17
OK	02.03	05.86
SiK	00.51	00.83
MoL	01.02	00.49
VK	00.59	00.53
CrK	04.94	04.39
MnK	01.31	01.10
FeK	85.40	70.63
Matrix	Correction	ZAF

(b)

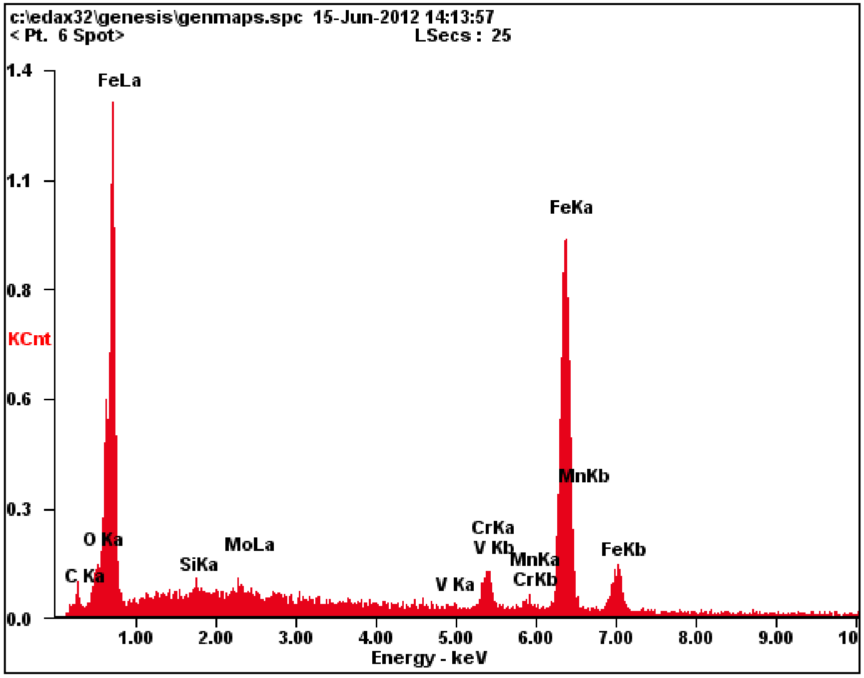

(c)

Figure 5-26: Second Spot – Un-Textured and Un-scratched (a) SEM picture with a Square of the Examined Spot. (b) The Material Compositions of the Squared Spot. (c) EDS Spectra of the Squared Spot.

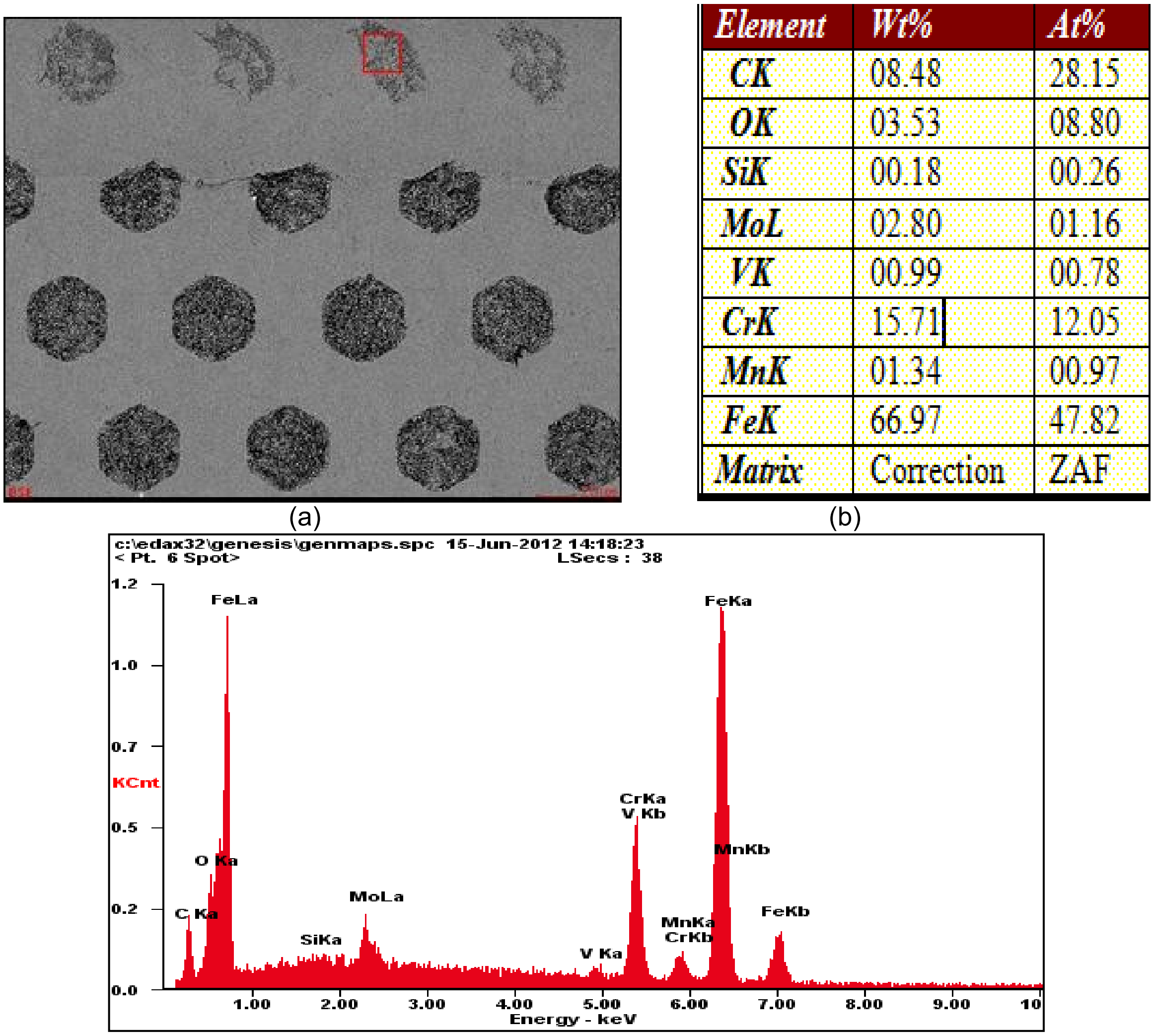
(a)

Element	Wt%	At%
CK	08.48	28.15
OK	03.53	08.80
SiK	00.18	00.26
MoL	02.80	01.16
VK	00.99	00.78
CrK	15.71	12.05
MnK	01.34	00.97
FeK	66.97	47.82
Matrix	Correction	ZAF

(b)

```
c:\edax32\genesis\genmaps.spc  15-Jun-2012 14:18:23
< Pt.  6 Spot>                          LSecs :  38
```

(c)

Figure 5-27: Third Spot – Scratched Textured Spot (a) SEM picture with a Square of the Examined Spot. (b) The Material Compositions of the Squared Spot. (c) EDS Spectra of the Squared Spot.

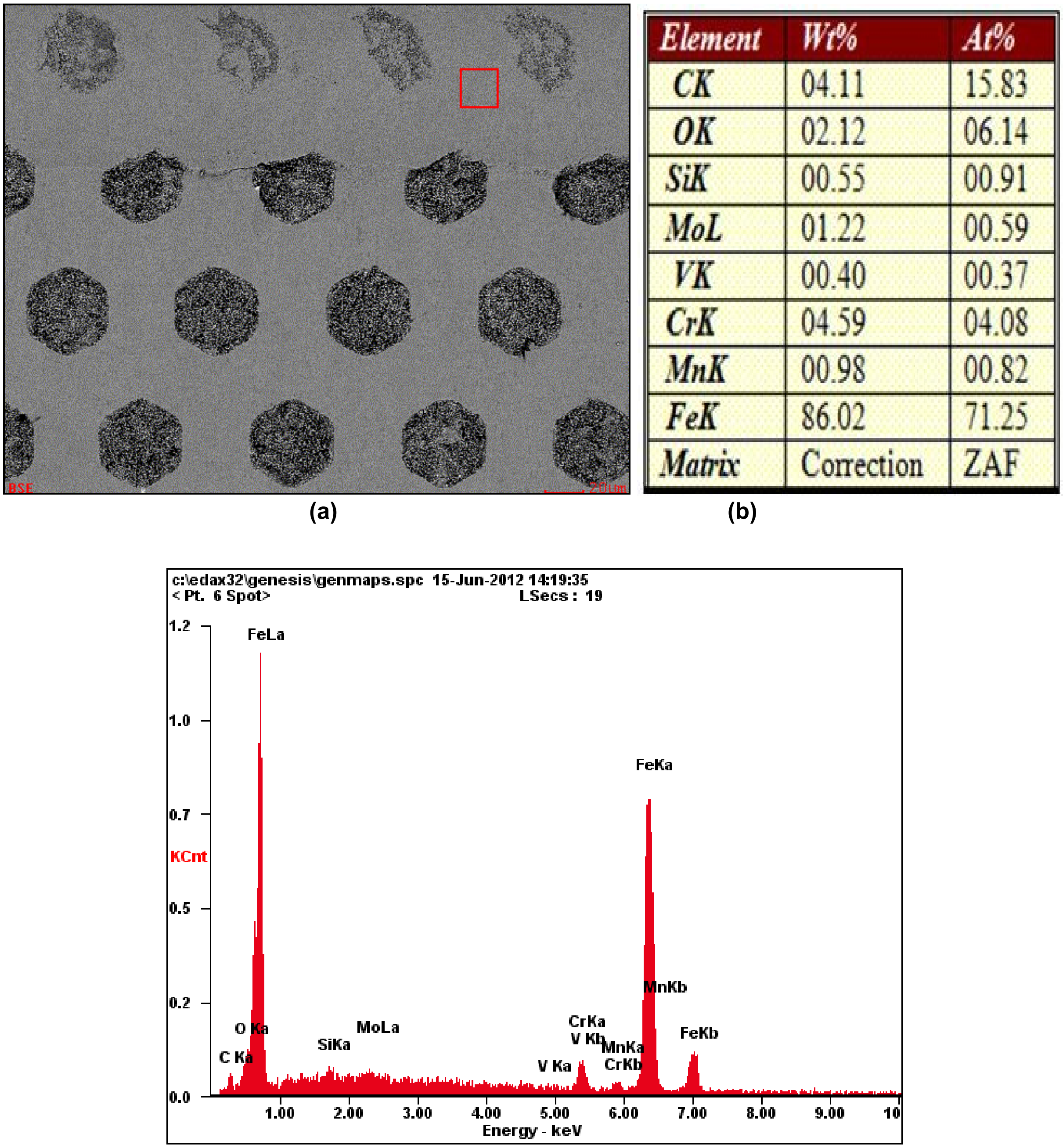

Element	Wt%	At%
CK	04.11	15.83
OK	02.12	06.14
SiK	00.55	00.91
MoL	01.22	00.59
VK	00.40	00.37
CrK	04.59	04.08
MnK	00.98	00.82
FeK	86.02	71.25
Matrix	Correction	ZAF

(a) (b)

(c)

Figure 5-28: Fourth Spot – Un textured and Scratched (a) SEM picture with a Square of the Examined Spot. (b) The Material Compositions of the Squared Spot. (c) EDS Spectra of the Squared Spot.

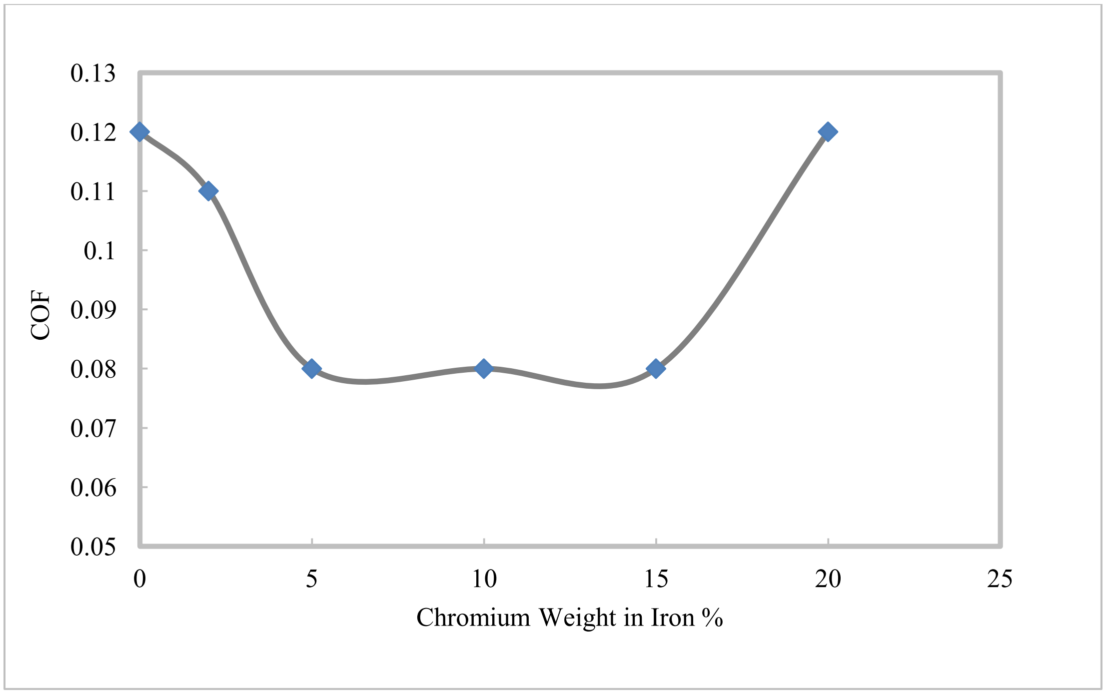

Figure 5-29: The Effect of Chromium Content on the Coefficient of Friction, reproduced [118]

5.5 Conclusions of Hexagonal Texturing by Photolithography

In this chapter, the hexagonal pattern was investigated. Three diameters of 40, 20, and 15 μm were selected, and the texture densities were narrowed down to between 0.25 and 0.67.

Photolithography with chemical etching was used to fabricate the patterns on air hardened tool steel samples. Twelve samples were patterned and tested using the scratch tester with a 200 μm radius Rockwell indenter tip to investigate the effect of the patterns on the coefficients of friction. Two scratches are made: one scratch is horizontally aligned with the hexagonal dimples, and the other scratch is done perpendicular to the first scratch. The following are concluded:

1. A minimum coefficient of friction is obtained when the friction coefficients are plotted versus the spatial texture densities for different hexagon's diameters.
2. A reduction of 28% in coefficient of friction was obtained vs. untextured etched plain sample.
3. This minimum coefficient of friction falls between the spatial texture density of 0.25 and 0.5.
4. The effect of the diameter as an independent parameter is still not as pronounced as with the patterned samples with circular dimples.
5. The spatial texture density (D/L) is still the most significant parameter, and the minimum coefficient of friction is obtained when the spatial texture

density is equal to 0.5, which is the same conclusion obtained from the circular dimples and the numerical models.

6. The orientation of the scratch, whether it is horizontal or vertical, has little impact on the result. However, in most cases, the vertical scratches record higher friction coefficients except for the spatial texture density of 0.67.
7. Photolithography is not recommended to be used in texturing since it causes changes in the chemical morphology of samples.
8. The coefficient of friction of the plain un-textured sample is lower than all the textured samples. This unexpected behavior is due to a high concentration of chromium in the hexagonal dimples, which results from dissolving iron during chemical etching.
9. When chromium weight percentage exceeds 15%, the coefficients of friction increase dramatically.
10. For the small diameters of 15 μm and 20 μm, the exact sharp angles of the hexagons could not be fabricated due to the undercut results from the isotropic etchants; these sharp corners are somewhat rounded.
11. Finally, photolithography with isotropic chemical etchants is not recommended for micro surface texturing due to undercuts and changes in chemical composition.

Chapter 6 EFFECT OF SURFACE PATTERNING ON ADHESION FORCES

6.1 Introduction on Adhesion Force

Adhesion between two surfaces in contact plays a crucial role on functionality and reliability of numerous applications, such as, micro-electrical-mechanical systems (MEMS), semiconductors, and electronic storage devices. Adhesion as discussed in chapter 2 is primarily caused by surface forces, such as van der Waals forces, capillary forces, and hydrogen bonding forces, along with external forces, such as electrostatic, magnetic or thermal forces.

Various models which were developed to determine the adhesion force between the contacting surfaces were in fact based on Hertz theory for elastic contact. The best known models are the Johnson, Kendall and Roberts (JKR)model and the Derjauin, Muller and Toprov (DMT) model [83]. JKR model assumed that the adhesion force between a flat surface and a sphere occurs only inside the elastic contact area. Derjauin, Muller and Toprov (DMT) model differed from the JKR model as it defined the adhesion force outside the contact zone [119-120].

Meine et al. [121] highlighted another difference between the two models, which included the material properties of the sphere and the type of the interaction force. They concluded that JKR model could be applicable to a contact system that involves a soft sphere and short range interaction forces while DMT model could be applied to a rigid sphere and weak long range interaction forces. Maguis et al [122] included the plastic deformation effect. Hamaker [123] developed a model of summation of the molecular forces based on the non-retarded additivity of the interaction energies. All aforementioned models used the surface energy and Dupré equation to predict the adhesion force.

As for the experimental investigations, the atomic force microscope (AFM) has been used extensively to directly measure the pull off forces from the force-displacement curves. Komvopoulos [124] carried out extensive analyses to explain the contact mechanisms of the adhesion and friction in MEMS, and he highlighted the influential role of roughness on the adhesion force. Meine et al [121] also drew attention to the effect of the surface roughness on the measured adhesion force using AFM. They concluded that for a constant geometric contact area, additional roughening led to a decrease in the adhesion force. Tayebi and Polycarpou [56, 125] identified three factors that controlled the adhesion force: roughness, asymmetry and peakiness. They found that the adhesion force could be reduced by an order of magnitude by increasing these three factors. Bachmann and Hierold [126-127] measured the adhesion force between different sizes of AFM tips and smooth and rough flat samples of silicon wafers, and it was concluded that as the area of contact between the tip and the sample decreased, the measured pull off forces decreased as well. In addition, rough samples showed less adhesion force compared to the smooth samples.

Ando and Ino [128] investigated the effect of the radius of curvature of the asperities which were fabricated using a focused ion beam on the friction and adhesion force.

Despite the extensive research efforts, the current state of the art lacks a thorough investigation on the effect of engineered surface patterning on the adhesion forces Therefore, the objective of the current study is twofold. First is to investigate the effects of the individual texture parameters, such as the dimple diameter (D), the spacing between the dimples (L), and the spatial texture density $\frac{D}{L}$ as well on the pull off force. The air hardened tool steel samples with circular craters which were fabricated by laser ablation are used in this investigation. Secondly, a comparison of the trends of the experimentally measured pull off forces, and the analytically estimated adhesion forces with respect to the spatial texture density is performed.

6.2 Analytical Model for Adhesion Force Measurement

As it was mentioned earlier, the most common surface interactions forces are capillary forces due to hydrogen bridging and van der Waals forces. The capillary forces are usually related to high relative humidity (RH) of the surroundings, and become important when relative humidity is greater than 50%. Therefore, capillary condensation can be eliminated if all measurements are done at room temperature with a RH of about 30% [129].

In the current study, the Hamaker summation model was adopted. This model is based on pair-wise additivity in which the spatial influence on the interaction force is neglected. The overall adhesion force $\boldsymbol{F_{adh}}$ is the summation of all individually calculated van der Waals forces between either a sphere and flat plane as in Equation 6.1 or two spheres as in Equation 6.2.

$$\boldsymbol{F_{adh}} = \frac{\boldsymbol{H_{12}R}}{\boldsymbol{6a_i^2}} \qquad (6.1)$$

where R is the radius of the sphere , H_{12} is the Hamaker constant for the combined materials in contact, and $\boldsymbol{a_i}$ is the separation distance between the sphere and the plane.

For the contact between the two spheres, the adhesion force can be calculated according to the Hamaker model as follows:

$$\boldsymbol{F_{adh}} = \frac{\boldsymbol{H_{12}(R_1R_2)}}{\boldsymbol{6a_i^2(R_1+R_2)}} \qquad (6.2)$$

where R_1 and R_2 are the radii of each of the two spheres in contact. The Hamaker constant, H_{12}, can be estimated from [123].

$$\boldsymbol{H_{12}} = \sqrt{\boldsymbol{H_1H_2}} \qquad (6.3)$$

where H_1 and H_2 are the individual Hamaker constants for the two materials in contact.

In the current study, the Hamaker Summation model has been modified to account for the surface texturing. The experimental approach considers a sphere (the AFM tip) with radius R_1 interacting with the textured surface. The textured surface is described as a set of the largest imaginary spheres with radii R_2's that fit between two adjacent dimples as shown in Figure 6-1.

The analytical model is developed based on this configuration, where the total number of inscribed spheres (m) can be calculated by summing up the number of spheres that are contained within the projected surface area of the spherical tip in contact. The separation distance, a_i, is modified to account for the surface roughness of the textured area, which is represented by root mean squares (rms) of the roughness, such that

$$\boldsymbol{a_i = rms + a_o} \qquad (6.4)$$

where a_o is the atomic distance which ranges between 0.3 to 0.4 nm.

Hamaker assumed that the interaction forces are additive. So, the total van der Waals forces are then calculated by summing up all the surface interactions between the fitted spheres and the tip as shown in Equation 6.5.

$$\boldsymbol{F_{adh} = \sum_0^m \frac{H_{12}(R_1 R_2)}{6{a_i}^2(R_1+R_2)}} \qquad (6.5)$$

This approximation is adequate for the objective of this study as the effect of the texturing parameters is the primary focus and not the exact values of the pull off forces.

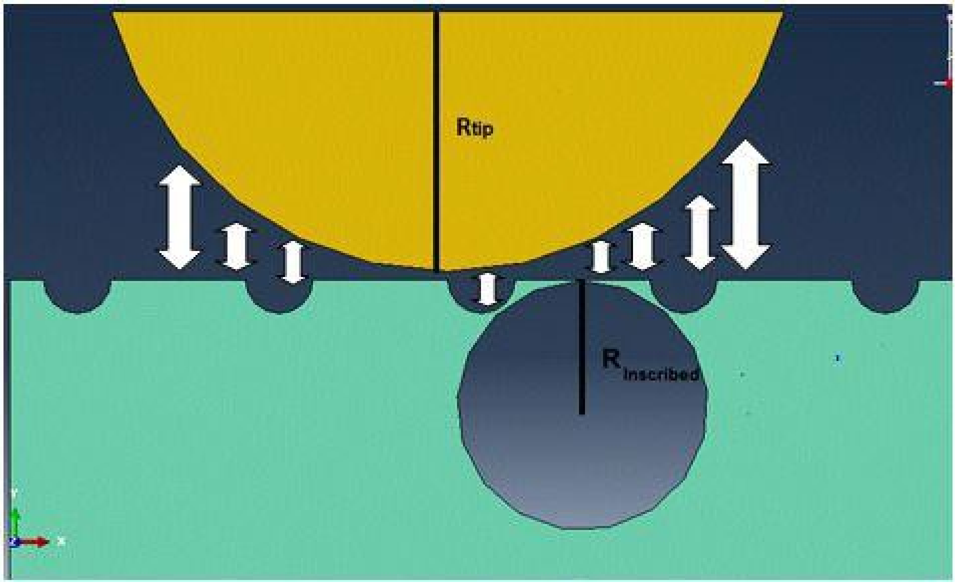

Figure 6-1: Illustration of the spherical tip (R1) in contact with the textured surface with the largest inscribed sphere, R2 fitted in between the laser craters.

6.3 Experimental Procedure for Adhesion Force Measurement

First, the samples with the circular pattern which are fabricated by laser ablation are used. Second, the probe of the AFM is customized in such a way that it can capture the differences between the textured samples in terms of size. Finally, AFM is used in contact mode to measure the adhesion force via recording force-distance curves. All AFM measurements are performed in dry condition.

6.3.1 Measurement of the Adhesion Force Using AFM

Digital Instruments Nanoscope IV AFM is utilized in contact mode. The cantilever tip contacts the surface while the change in cantilever deflection is monitored by a spilt photodiode. A feedback loop keeps this deflection constant by vertically moving the piezoelectric scanner at each (x,y) data point. As a result, the force between the cantilever and the sample is kept constant. These vertical distances which are moved by the scanner are stored in a computer to form the topographic image of the surface. Figure 6-2 shows a schematic diagram for the components of AFM in contact mode.

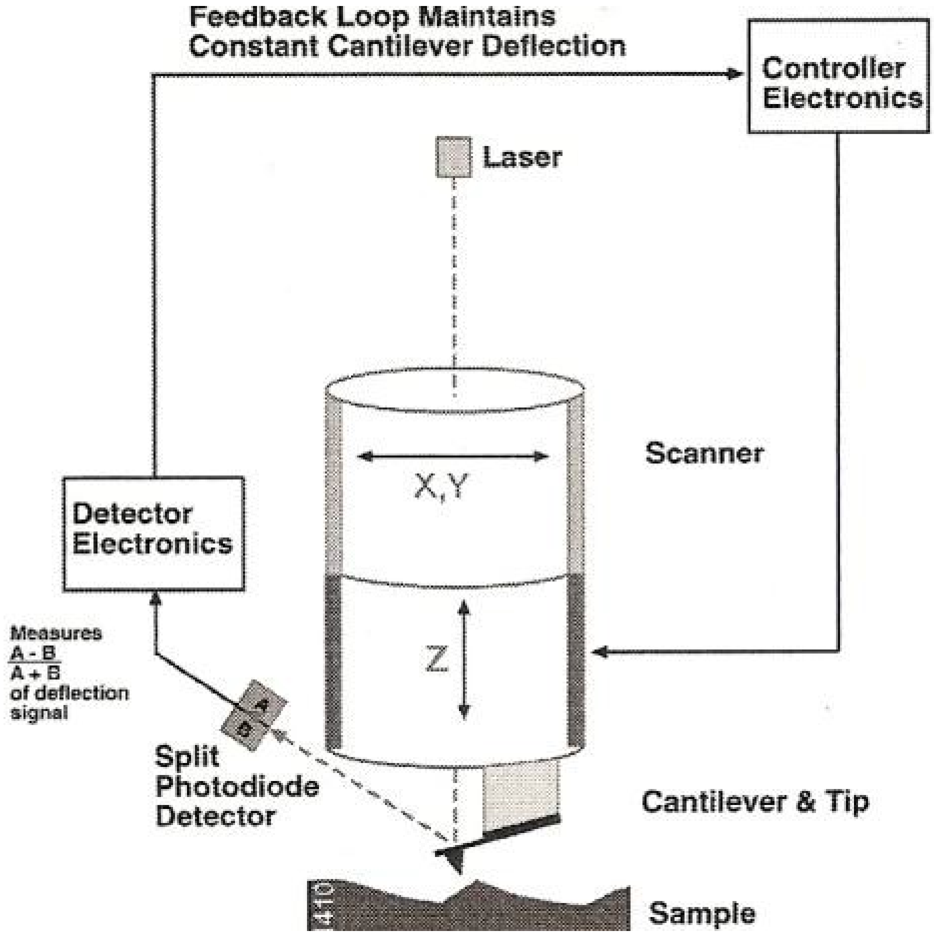

Figure 6-2: Schematic diagram of AFM in Contact Mode

A polystyrene spherical attachment of 120 μm in diameter is mounted on the silicon nitride cantilever. A SEM picture of the mounted probe is depicted in Figure 6-3. The size of the ball is chosen to cover at least one wavelength of the largest set of the dimples' pattern so that the effect of texturing size can be detected.

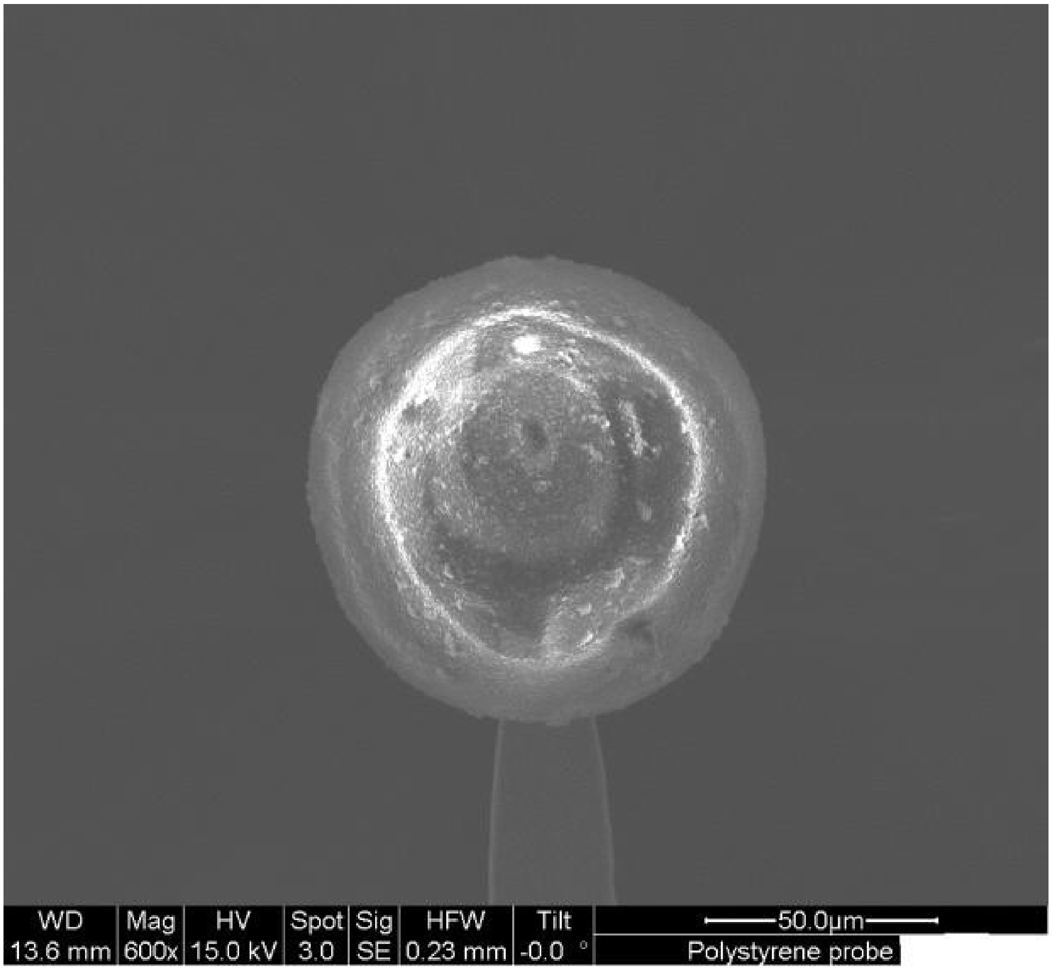

Figure 6-3: SEM Micrograph of the AFM tip with Spherical Probe (600X)

The polystyrene ball has Young's modulus of 3.3 GPa and Poisson ratio of 0.32. The cantilever springs are calibrated and the springs' constants for different cantilevers range between 0.35 to 0.42 N.m. This customized cantilever is prepared and calibrated by Nova Scan Lab (USA). For each sample, the force - distance curve is recorded. This reading is repeated ten times at three different spots for each sample. Then, the overall average pull off force is calculated.

6.4 Results and Discussion of Adhesion Force Measurement

Using the AFM in contact mode, and adjusting the sensitivity deflections, force-distance curves are obtained for each textured sample. Ten force-displacement curves are recorded at three different spots with a total of 30 force-deflection curves for each sample. The average of these 30 force -deflection curves is taken with standard deviation ranging between 10 and 20%. In addition, the pull-off force is determined for a polished plain sample to be used as a reference. Figure 6-4 shows a typical force -displacement (Z) curve of a textured sample. The highest pull-off force of 200nN amongst all samples was recorded for the reference polished non-textured sample. The measured pull-off forces for any of the textured samples were at least two times smaller than the reference non-textured sample.

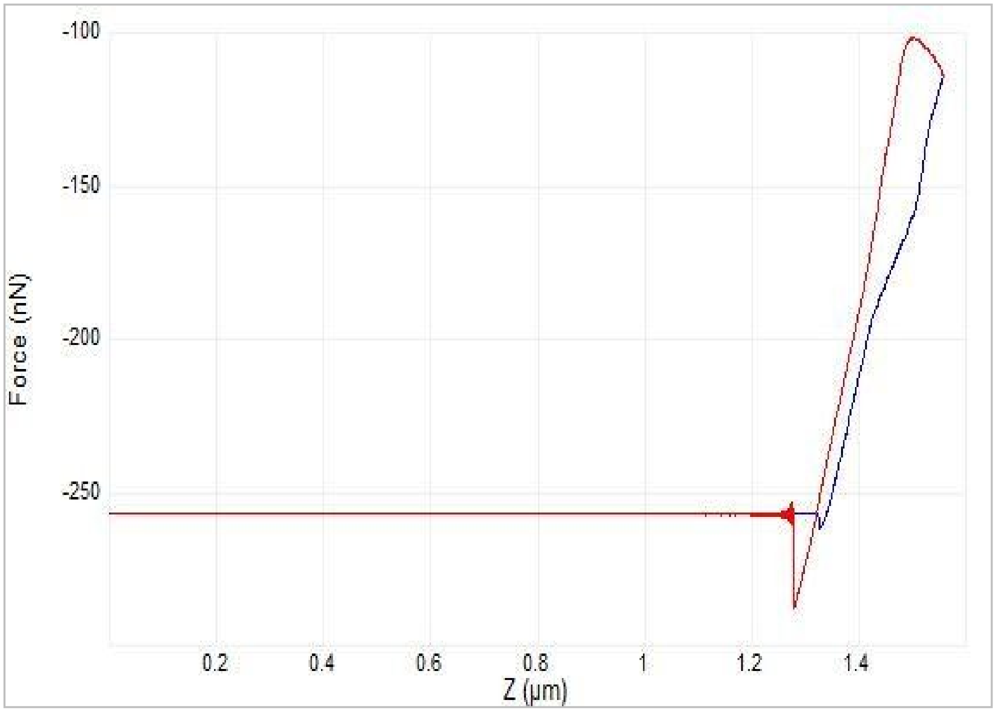

Figure 6-4: The Force-Displacement (Z) Curve for Sample#3

6.4.1 The Effect of Individual Texture Parameters on the Measured Adhesion Force

Based on the pull-off forces measurements for different texturing parameters, the diameter of the texture is inversely proportional to the adhesion force for the same texture density as shown in Figure 6-5 and Figure 6-7 except for sample #7D10L40. It is also noticed when the diameter increases from 10 μm to 20 μm, the reduction of the adhesion force is very small unlike the case when the diameter goes up from 5 μm to 10 μm, the adhesion force is 50 % less. This might be an indication that there is threshold texture size above which the adhesion forces - contact area curve shows a monotonic behavior.

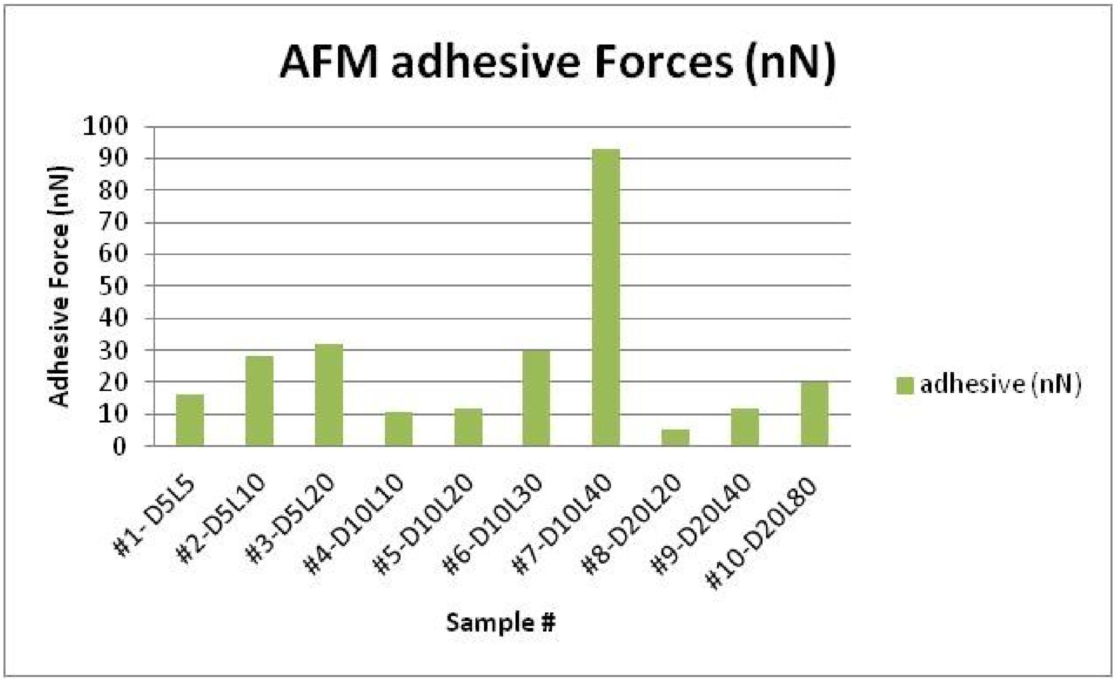

Figure 6-5: The AFM Measured Adhesion Forces for the Textured Samples

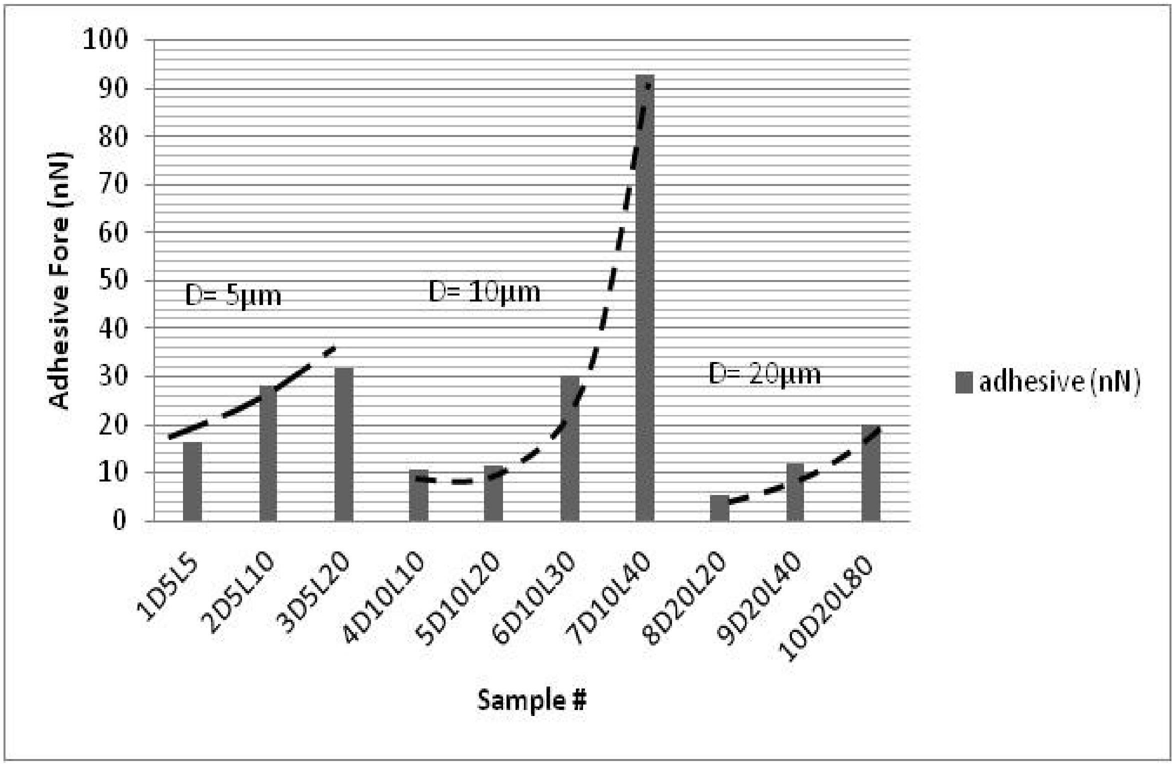

Figure 6-6: The Effect of the Texture Size on Adhesion Force (dotted line shows the increasing trend with the increase of the distance between the laser craters, L)

In Figure 6-6, the dotted lines show the increasing trend of the adhesion force when the spacing (L) between the laser craters increases while the diameter of the crater is kept constant. This can be explained by the increase of the contact area between the craters.

6.4.2 The Effect of the Spatial Texture Density on the Measured Adhesion Force.

The spatial texture density has a pronounced effect on the measured adhesion force. As the texture density increases, the measured adhesion force decreases. In this study, three different surface texture densities' were examined: 0.25,0.5, and 1.

From Figure 6-7, it is observed that as the spatial texture density increases from 0.25 to 1, the measured adhesion forces decrease by almost 50%. This observation is noticed for all different dimples' diameters but with different reduction percentages. This is due to the fact that if the spatial texture density is converted to areal texture density, it represents the non-contact area.

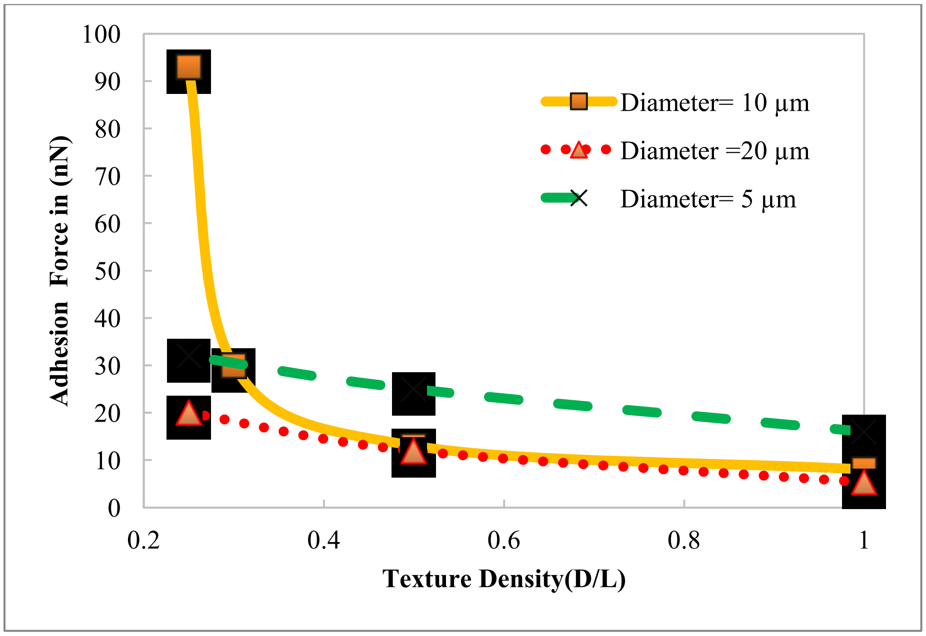

Figure 6-7: The Effect of the Texture Density on Adhesion Forces Measured by AFM

6.4.3 Empirical Relation between the Spatial Texture Density and Adhesion Forces

If it is assumed that the relationship between the adhesion forces and the spatial texture densities $\left(\frac{D}{L}\right)$ follows the power law, equation.6.6 is written as :

$$F_{adh} = C\left(\frac{D}{L}\right)^{n} \qquad (6.6)$$

where C and n are constants that depend on the properties of the two materials in contact. The least squares fitting power law method is used to estimate the coefficients C and n for the tool steel and polystyrene pair. They are equal to 9.0744 and -1.014 respectively as shown in Figure 6-8.

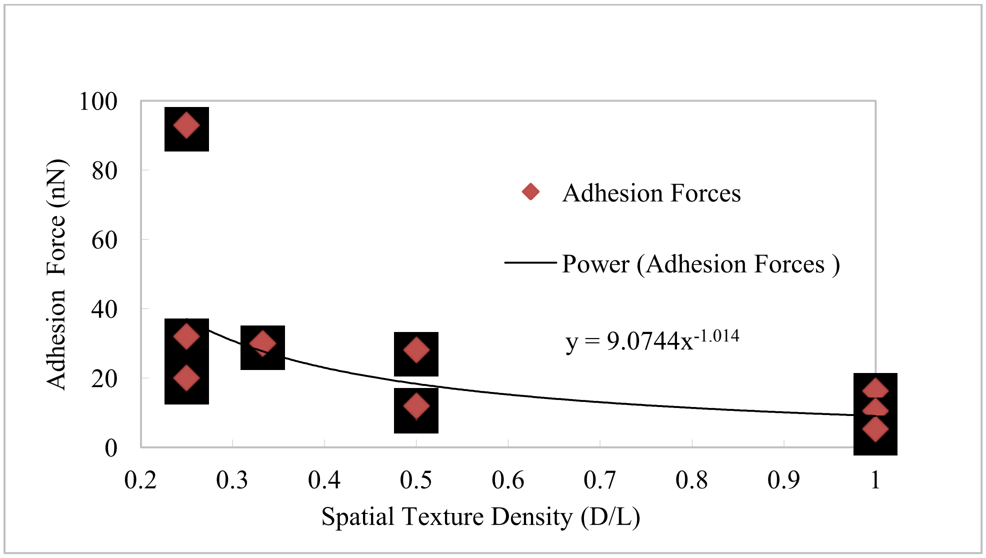

Figure 6-8: The Least Squares Fitting Power Law of the Measured Adhesion Forces

6.5 Results of Hamaker Summation Model

As it was mentioned in the previous section, van der Waals forces are the sole surface interactions that determine the adhesion force between the patterned samples and the polystyrene tip. Hamaker summation model is modified to analytically approximate the pull off force between the tool steel textured surface and the polystyrene spherical tip.

The Hamaker constant, H_{12}, for the Polystyrene-Tool steel is estimated by Eq.6.4 where H_{11} for tool steel is equal to 5.04x10^{-18} while H_{22} for polystyrene is 6.9x10^{-20} [123]. So, H_{12} is estimated to be 5.7.x10^{-19}J. R_1 is the radius of polystyrene ball and is equal to 60 μm and R_2 is the radius of the largest imaginary sphere fitted between the two adjacent dimples as shown in Figure 6-1. The total number of inscribed spheres (m) varies for each sample and it is based on the distance between the centers of the adjacent dimples (L). The separation distance a_i is calculated for each sample based on root mean square roughness that is obtained from the optical profilometer (WYKO). Then, the total adhesion force is estimated according to Equation 6.5 and the results are plotted in Figure 6-9.

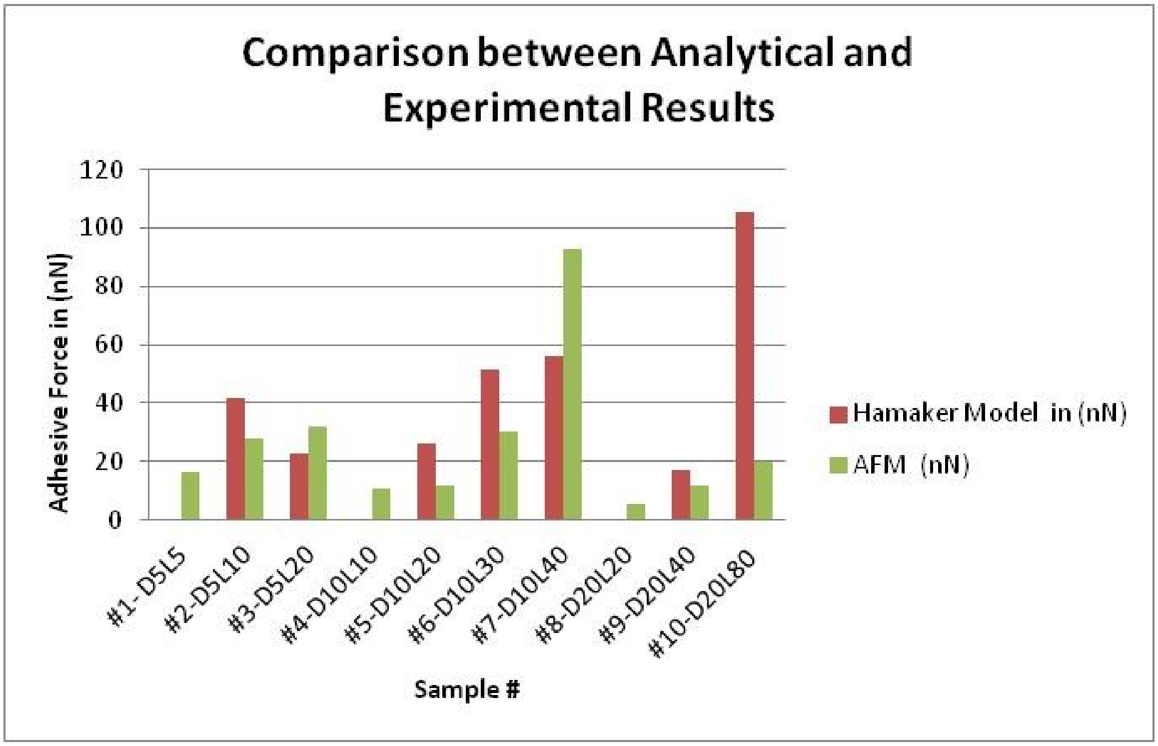

Figure 6-9: The analytically Calculated Adhesion Forces Using Hamaker Summation Model

In this comparison, the analytically estimated adhesion forces overestimate the experimentally measured adhesion. This might be due to including of the root mean square roughness which is just an estimate. Moreover, it might be due to the approximation of the area in between the dimples. On the other hand, they follow the same trend of the experimentally measured adhesion forces by AFM. For the same texture diameter, as the distance L, increases, the adhesion force increases. It can also be observed that the adhesion forces for samples #1D5L5 ,#4D10L0, and # 8D0L20 are not shown since the holes are adjacent and the calculated contact area is zero. So, the adhesion force is zero. Besides, The adhesion force for sample #3D5L20 does not follow the trend because it has very high roughness compared to other samples.

It is evident that the effect of surface roughness influences the analytical results significantly. So, care should be taken when ignoring the roughness in calculating the adhesion force. Finally, for the results of the analytical model, the diameter of dimples does not show any uniform trend with respect to the adhesion forces.

6.6 Conclusions of the Adhesion Force Measurement

The premise of this study was to investigate the effect of the surface texturing on adhesion forces between two solid surfaces in contact. The most commonly used analytical models were presented with the emphasis of the advantages and drawbacks of each model, and the parameters that influence the adhesion force. The Hamaker summation model was modified to include the effect of the texturing parameters, and it was used to calculate the adhesion forces. The resulting adhesion forces are quite high in comparison with the experimentally measured pull off forces, and this is attributed to the direct involvement of the root mean squares surface roughness.

AFM is also used to measure the pull off forces from the force-distance curves. The adhesion forces between the air hardened tool steel textured samples and the polystyrene ball for different D and L combinations are measured. It was found that the effect of the texture diameter, D, is pronounced, and it is inversely proportional to the adhesion force. Whereas, the spacing between the centres of the texture dimples, L, is directly proportional to the adhesion force. It is concluded that the accurate parameter to define the surface texture is the spatial texture density (D/L). This parameter includes both parameters, L and D.

It is clear that when the spatial surface texture density increases, the adhesion force decreases due to the reduction of the contact area, yet attention should be paid also to the high stresses which might be developed, and resulting in high mechanical deformation.

Chapter 7 GENERAL DISCUSSION AND CONCLUSIONS

Friction is involved in thousands of everyday applications, such as car engines, mechanical seals, hydraulics, MEMS devices, metal forming tools, magnetic storage devices, and human implants. The energy and raw material waste due to friction is enormous. Therefore, the importance of understanding and analysing the mechanisms involved in friction is a constant demand to be able to find a feasible solution to control friction. If friction is controlled then functionality, reliability, energy, and raw materials savings would definitely improve.

7.1 Summary of the Research

This dissertation has investigated the effects of micro-surface texturing as an evolving means for tribological performance improvement on the coefficient of friction in dry sliding contact under constant normal loading.

Returning to the hypothesis posed at the beginning of this study, it is now possible to state that there is a certain spatial texture density at which the coefficient of friction is minimal.

In other words, this dissertation set out to investigate if a minimum coefficient of friction exists or not. If yes, then the most significant surface texturing parameter(s) which control the coefficient of friction need to be identified, then the minimum value(s) need to be found. To reach this objective, the above hypothesis has been tested analytically, numerically, and experimentally.

As for analytical investigation, it has been proven that the two components of the friction force, adhesion and mechanical deformation, have opposite trends with respect to the real contact area. Therefore, the summation of their derivatives with respect to area could be zero, which proves the existence of a minimum friction force.

With regard to the numerical approach, two and three dimensional finite element models have been developed and analyzed using ABAQUS 6.10, a multipurpose finite element code. The two dimensional plane strain elastic-perfectly plastic textured surface in contact with a rigid spherical indenter has been modeled. Randomized canter set fractal geometry was used to model the surface roughness so that more realistic conclusions could be drawn. The fractal roughness was superimposed on micro meandered surface texturing. Different widths of the square pads were tested to check the effects on the friction coefficient. No obvious trend was noticed when the different texturing widths are plotted vs. the coefficients of friction; nevertheless, when the texturing size (D) is divided by the distance between the centers of two consecutive rectangular depressions (L), a minimum coefficient of friction is found at $\frac{D}{L}$ equals 0.4.

This dimensionless quantity, $\frac{D}{L}$ is called spatial texture density, and is identified as a significant texturing parameter for many reasons. First, this quantity shows an explicit minimum when it is plotted against the friction coefficient. Second, it is a dimensionless quantity, so it can be used at different length scales. Finally, this quantity combines the effect of the size and the density of the texture, thus it is very informative.

Further investigation was needed to test the hypothesis and verify the findings of the two-dimensional models. Therefore, three-dimensional finite element models were developed. In the three-dimensional models, two patterns were investigated, circular and hexagonal, to check the effect of the texture shape on the friction coefficient. A range of texture sizes are tested. This range varies from 5 µm to 80 µm. In addition, the different spatial texture densities were explored, ranging between 25% and 100%. The effect of the pattern anisotropy on the friction was also checked. The recessed texturing of either circular or hexagonal shapes was arranged in a hexagonal layout so that the resulting stresses are propagated throughout the walls of the honeycomb arrangement. This hexagonal layout was also used to fabricate textured samples. The material properties of air hardened tool steel were modeled with an elastic-fully plastic deformation assumption. The size of the indenter was modeled sufficiently large so as to capture the effect of the largest texturing wavelength. The results obtained from the three dimensional simulations agree with the results of the initial two dimensional models, and are shown by the following:

- The spatial texture density (D/L) still has a pronounced trend when it is plotted against the friction coefficient.

- The minimum coefficient of friction exists, and falls in a range of between 0.25 and 0.5 of the spatial texture density.
- The two friction components, mechanical deformation and adhesion, behave inversely to each other when they are plotted vs. the spatial texture density. As the spatial texture density increases, the adhesion decreases but the mechanical deformation increases. The behaviour can be justified due to the change in real contact area which can be measured by the square of the complement of the spatial texture density (D/L). When the real area of contact decreases, the adhesion forces decrease. On the other hand, the mechanical deformation increases due to concentrated high stresses which result in the flow of material at the interface.
- The hexagonal patterns outperform the circular patterns for both components of the friction within the minimum range of the spatial texture density.
- The proposed pattern layout has anisotropic properties; however, the difference in the coefficients of friction is less than 3% due to the increase of contact area.

The above mentioned findings were validated by measuring the friction coefficients of the circular and hexagonal textured samples of air hardened tool steel which were mirror polished. The circular patterns were fabricated using laser ablation, while photo lithography with isotropic chemical etchant was used to fabricate the hexagonal patterns. A micro scratch tester with a diamond

Rockwell tip radius of 200 μm was used to measure the friction coefficients of the textured samples under a constant normal load and sliding distance of 500 μm.

For the circular laser surface texturing, three diameters were fabricated, 5, 10, and 20 μm, and three spatial surface texturing densities, 0.25, 0.5, and 1. The most obvious findings to emerge from this experiment are:

- The minimum coefficient of friction appears between the spatial texture densities of 0.25 and 0.5.
- The highest reduction of 13% in the coefficient of friction occurs at a spatial texture density of 0.5, where the diameter (D) of the dimple equals 20 μm and the distance (L) between the centers of two consecutive dimples is 40 μm.
- In the case of a spatial dimple density of 1, the coefficient of friction increases due to the increase of the mechanical deformation component of the friction.

For the hexagonal patterns, three diameters of 15, 20, and 40 μm were fabricated, and the spatial texture densities were narrowed down from 0.25 to 0.6667. Photolithography with a ferric chloride etchant was used to fabricate the hexagonal patterns. Horizontal and vertical scratches were made under the same conditions as with circular pattern. The following conclusions can be drawn:

- The spatial texture density (D/L) is still the most significant parameter, and the lowest friction coefficients are obtained when the spatial texture densities range from 0.25 to 0.5. This is the same conclusion which was obtained from the numerical simulations and the circular patterns.

- A reduction of 28% in the coefficient of friction was achieved at a spatial texture density of 0.5 with D = 20 μm and L= 40 μm. These are the same texturing parameters at which the lowest coefficient of friction of the circular patterning was obtained.

Investigations on the effect of the surface texturing on adhesion were independently carried out experimentally and analytically. Using AFM, the adhesion forces between the circular textured samples and spherical smooth probe were estimated. A customized polystyrene particle with a diameter of 125 μm was attached to a calibrated silicon nitride cantilever for this purpose. Moreover, the basic Hamaker summation model was modified to incorporate the surface texturing in modeling the rough surface. The following conclusions emerged from the adhesion investigation.

- The adhesion force decreases with the increase of the spatial surface texturing due to the reduction of the real area of contact.
- The decrease in the adhesion force with respect to the spatial texture density reveals an exponential trend.
- The analytically measured adhesion forces are rather low in comparison with the experimentally measured values, and this is attributed to the consideration of the root mean square surface roughness in the analytical model.

7.2 Research Contributions

As it is mentioned in Chapter 1, there have been very few researchers tackling the friction of dry sliding conditions due to the lack of theoretical foundations [2]. This comprehensive study serves as a base for future research since the posed hypothesis has been verified analytically, numerically, and experimentally. The following is a summary of findings which have been mentioned earlier, and they would add to the current state of the art:

1. Micro surface texturing does reduce the coefficient of friction if appropriate surface texturing parameters are identified and optimized.
2. The dimensionless quantity, spatial texture density (D/L), is the most significant texture parameter because it incorporates the size of the texturing features, and the density as well.
3. A minimum coefficient of friction does exist, and it is correlated to the real area of contact.
4. The minimum coefficient of friction falls between 0.25 and 0.5 of the spatial texture density.
5. Adhesion forces decrease nonlinearly with the increase of the spatial texture density.
6. The mechanical deformation, either elastic or plastic, increases with the increase of the spatial texture density.
7. With the circular patterning, a reduction of 14.5 % in the coefficient of friction is obtained under normal and sliding conditions with zero lubrication. The spatial texture density at which the minimum coefficient of

friction is achieved is 0.5, the circular diameter is equal to 20 μm, and the spatial distance is equal to 40 μm.

8. With the hexagonal patterning, a reduction of 28 % in the coefficient of friction is obtained. The texturing parameters at which the minimum coefficient of friction is attained are the same as the circular patterning. The hexagon's diameter is 20 μm and the spatial distance (L) is 40 μm.
9. Hexagonal patterning outperforms the circular patterning with regard to the reduction in the friction coefficient.
10. The hexagonal layout of the patterning is very effective in reducing the pattern anisotropy.

7.3 Recommendations and Future Research

- Laser ablation is highly recommended to fabricate the different patterns of surface texturing.
- Different materials, such as aluminum and magnesium alloys, which are used in different automotive engine components, need to be investigated.
- The premise of surface texturing can be extended to lower length scales, i.e. the nano scale, and the effect on the coefficient of friction can be explored.
- This study is limited to negative surface texturing. Further investigation might be done to test similar hypotheses for positive (protruding) surface texturing.
- Combining surface texturing with a low friction coating material needs to be further explored.

REFERENCES

1. Nakada,M., *Trends in engine technology and tribology.* Tribol. Int, 1994. **27**(1): p. 3-8.
2. Etsion, I., *State of the art in laser surface texturing.* Journal of Tribology, 2005. **127**(1): p. 248-253.
3. Costa, H.L. and I.M. Hutchings, *Effects of die surface patterning on lubrication in strip drawing.* Journal of Materials Processing Technology, 2009. **209**(3): p. 1175-1180.
4. Etsion, I. *Improving tribological performance of mechanical components by laser surface texturing*. 2004. USA: Kluwer Academic/Plenum Publishers.
5. Borghi, A., E. Gualtieri, D. Marchetto, L. Moretti and S. Valeri, *Tribological effects of surface texturing on nitriding steel for high-performance engine applications.* Wear, 2008. **265**(7-8): p. 1046-51.
6. Burstein, L. and D. Ingman. *Pore ensemble statistics in application to lubrication under reciprocating motion(C)*. 2000: Society of Tribologists and Lubrication Engineers.
7. Etsion, I. and L. Burstein, *A model for mechanical seals with regular microsurface structure.* Tribology Transactions, 1996. **39**(3): p. 677-683.
8. Kovalchenko, A., O. Ajayi, A. Erdemir, G. Fenske and I. Etsion. *The effect of laser surface texturing on transitions in lubrication regimes during unidirectional sliding contact*. 2005: Elsevier Ltd.
9. Ronen, A., I. Etsion and Y. Kligerman, *Friction-reducing surface-texturing in reciprocating automotive components.* Tribology Transactions, 2001. **44**(3): p. 359-366.
10. Ryk, G., Y. Kligerman, I. Etsion and A. Shinkarenko, *Experimental investigation of partial laser surface texturing for piston-ring friction reduction.* Tribology Transactions, 2005. **48**(4): p. 583-588.
11. Siripuram, R.B. and L.S. Stephens, *Effect of deterministic asperity geometry on hydrodynamic lubrication.* Journal of Tribology, 2004. **126**(3): p. 527-534.
12. Tnder, K. *Hydrodynamic effects of tailored inlet roughnesses: Extended theory*. 2004: Elsevier Ltd.
13. Venkatesan, S. and L.S. Stephens. *Surface textures for enhanced lubrication: Fabrication and characterization techniques*. Proceedings of the World Tribology Congrss III,2005.p.521-522.
14. Wang, X., K. Kato, K. Adachi and K. Aizawa, *Loads carrying capacity map for the surface texture design of SiC thrust bearing sliding in water.* Tribology International, 2003. **36**(3): p. 189-197.
15. Xiaolei, W., K. Adachi, K. Otsuka and K. Kato, *Optimization of the surface texture for silicon carbide sliding in water.* Applied Surface Science, 2006. **253**(3): p. 1282-6.
16. Xiaolei, W., K. Kato and K. Adachi, *The critical condition for the transition from HL to ML in water-lubricated SiC.* Tribology Letters, 2004. **16**(4): p. 253-8.
17. Xinqi, Y., L. Meihong, W. Zhenhui, P. Peiying and C. Renliang, *Experimental investigation on friction performance of mechanical seals with a laser-textured seal face.* Materials Science Forum, 2007. **532-533**: p. 81-4.
18. Gualtieri, E., A. Borghi, L. Calabri, N. Pugno and S. Valeri, *Increasing nanohardness and reducing friction of nitride steel by laser surface texturing.* Tribology International, 2009. **42**(5): p. 699-705.
19. Koide, S. and S. Kambe, *Formation of Bi2Sr2Ca1-xYxCu2Oy thin film grown by excimer laser ablation technique.* Physica C, 2002. **378-381**: p. 1260-4.

20. Wang, Q.J. and Z. Dong, *Virtual texturing: modeling the performance of lubricated contacts of engineered surfaces.* Transactions of the ASME. Journal of Tribology, 2005. **127**(4): p. 722-8.
21. Wang, X., K. Kato and K. Adachi, *The lubrication effect of micro-pits on parallel sliding faces of sic in water.* Tribology Transactions, 2002. **45**(3): p. 294-301.
22. Krupka, I., M. Hartl and P. Svoboda, *Effects of surface topography on lubrication film formation within elastohydrodynamic and mixed lubricated non-conformal contacts.* Proceedings of the Institution of Mechanical Engineers, Part J (Journal of Engineering Tribology), 2010. **224**(J8): p. 713-22.
23. Saka, N., H. Tian and N.P. Suh, *Boundary lubrication of undulated metal surfaces at elevated temperatures.* Tribology Transactions, 1989. **32**(3): p. 389-395.
24. Tian, H., N. Saka and N.P. Suh, *Boundary lubrication studies on undulated titanium surfaces.* Tribology Transactions, 1989. **32**(3): p. 289-296.
25. Wakuda, M., Y. Yamauchi, S. Kanzaki and Y. Yasuda, *Effect of surface texturing on friction reduction between ceramic and steel materials under lubricated sliding contact.* Wear, 2003. **254**(3-4): p. 356-63.
26. Komvopoulos, K., *Sliding friction mechanisms of boundary-lubricated layered surfaces. Part II. Theoretical analysis.* Tribology Transactions, 1991. **34**(2): p. 281-291.
27. Pettersson, U. and S. Jacobson. *Influence of surface texture on boundary lubricated sliding contacts*. 2003. Stockholm, Sweden: Elsevier Ltd.
28. Suh, N.P., M. Mosleh and P.S. Howard, *Control of friction.* Wear, 1994. **175**(1-2): p. 151-158.
29. Brizmer, V., Y. Kligerman and I. Etsion, *A laser surface textured parallel thrust bearing.* Tribology Transactions, 2003. **46**(3): p. 397-403.
30. McNickle, A.D. and I. Etsion, *Near-contact laser surface textured dry gas seals.* Journal of Tribology, 2004. **126**(4): p. 788-794.
31. Nosonovsky, M. and B. Bhushan, *Multiscale friction mechanisms and hierarchical surfaces in nano- and bio-tribology.* Materials Science and Engineering R: Reports, 2007. **58**(3-5): p. 162-193.
32. Saka, N. and N.P. Suh, *Plowing friction in dry and lubricated metal sliding.* Journal of Tribology, 1986. **108**(3): p. 301-313.
33. Voevodin, A.A. and J.S. Zabinski, *Laser surface texturing for adaptive solid lubrication.* Wear, 2006. **261**(11-12): p. 1285-92.
34. Schneider, Y.G., Formation of surfaces with uniform micropatterns on precision machine and instrument parts. Precision Engineering, 1984. **6**(4): p. 219-225.
35. Willis, E.,*Surface finish in relation to cylinder liners*. Wear, 1985. **109**(1-4): p. 351-366.
36. Wet Etching of (100) Silicon Wafer. Available from: http://www.parallel-synthesis.com/SiliconMicrofabrication.htm [cited 2012 Oct 13,2012].
37. Greco, A., S. Raphaelson, K. Ehmann, Q.J. Wang and C. Lin, *Surface texturing of tribological interfaces using the vibromechanical texturing method.* Journal of Manufacturing Science and Engineering, Transactions of the ASME, 2009. **131**(6): p. 0610051-0610058.
38. Kononenko, T.V., S.V. Garnov, S.M. Pimenov, V.I. Konov, V. Romano, B. Borsos, and H.P. Weber, *Laser ablation and micropatterning of thin TiN coatings.* Applied Physics A (Materials Science Processing), 2000. **A71**(6): p. 627-31.
39. Zhao, J., F. Sadeghi and H.M. Nixon. *A finite element analysis of surface pocket effects in Hertzian line contact*.Journal of Triboloy,1999.122(1):p47-54.

40. Stephens, L.S., R. Siripuram, M. Hayden and B. McCartt, *Deterministic micro asperities on bearings and seals using a modified LIGA process.* Transactions of the ASME. Journal of Engineering for Gas Turbines and Power, 2004. **126**(1): p. 147-54.
41. Kligerman, Y. and I. Etsion, *Analysis of the hydrodynamic effects in a surface textured circumferential gas seal.* Tribology Transactions, 2001. **44**(3): p. 472-478.
42. Etsion, I., Y. Kligerman and G. Halperin, *Analytical and experimental investigation of laser-textured mechanical seal faces.* Tribology Transactions, 1999. **42**(3): p. 511-516.
43. Kligerman, Y., I. Etsion and A. Shinkarenko, *Improving tribological performance of piston rings by partial surface texturing.* Transactions of the ASME. Journal of Tribology, 2005. **127**(3): p. 632-8.
44. Tnder, K., *Inlet roughness tribodevices: Dynamic coefficients and leakage.* Tribology International, 2001. **34**(12): p. 847-852.
45. Ryk, G., Y. Kligerman and I. Etsion, *Experimental investigation of laser surface texturing for reciprocating automotive components.* Tribology Transactions, 2002. **45**(4): p. 444-449.
46. Suh, N.P. and H.C. Sin, *The genesis of friction.* Wear, 1981. **69**(1): p. 91-114.
47. Dumitru, G., V. Romano, H.P. Weber, H. Haefke, Y. Gerbig, and E. Pfluger, *Laser microstructuring of steel surfaces for tribological applications.* Applied Physics A (Materials Science Processing), 2000. **A70**(4): p. 485-7.
48. Varenberg, M., G. Halperin and I. Etsion, *Different aspects of the role of wear debris in fretting wear.* Wear, 2002. **252**(11-12): p. 902-10.
49. Sugihara, T. and T. Enomoto, *Improving anti-adhesion in aluminum alloy cutting by micro stripe texture.* Precision Engineering, 2012. **36**(2): p. 229-237.
50. Hamilton, D.B., J.A. Walowit and C.M. Allen, *Theory Of Lubrication By Microirregularities.* American Society of Mechanical Engineers -- Transactions -- Journal of Basic Engineering, 1966. **88**(1): p. 177-185.
51. Anno, J.N., J.A. Walowit and C.M. Allen. *Microasperity lubrication*. 1967. New York, NY, United States: American Society of Mechanical Engineers (ASME).
52. Etsion, I. and O. Michael, *Enhancing sealing and dynamic performance with partially porous mechanical face seals.* S T L E Tribology Transactions, 1994. **37**(4): p. 701-710.
53. Etsion, I. and G. Halperin, *A laser surface textured hydrostatic mechanical seal.* Tribology Transactions, 2002. **45**(3): p. 430-434.
54. Yu, X.Q., S. He and R.L. Cai. *Frictional characteristics of mechanical seals with a laser-textured seal face*. Journal of Materials Processing Techology, 2002.**129**(1-3): p.463-466.
55. Tung, S.C. and M.L. McMillan, *Automotive tribology overview of current advances and challenges for the future.* Tribology International, 2004. **37**(7): p. 517-536.
56. Tayebi, N. and A.A. Polycarpou, *Reducing the effects of adhesion and friction in microelectromechanical systems (MEMSs) through surface roughening: comparison between theory and experiments.* Journal of Applied Physics, 2005. **98**(7): p. 73528-1.
57. Baumgart, P., D.J. Krajnovich, T.A. Nguyen and A.G. Tam. *A new laser texturing technique for high performance magnetic disk drives*. IEEE Transactions on Magentics, 1995. **31**(6): p.2946-2951.
58. Tayebi, N. and A.A. Polycarpou, *Adhesion and contact modeling and experiments in microelectromechanical systems including roughness effects.* Microsystem Technologies, 2006. **12**(9): p. 854-69.
59. Rivin, E., *Stiffness and Damping in Mechanical Design*. 1999, CRC Press. p. 528.

60. Wiklund, D., B.-G. Rosen and L. Gunnarsson, *Frictional mechanisms in mixed lubricated regime in steel sheet metal forming.* Wear, 2008. **264**(5-6): p. 474-479.
61. Geiger, M., U. Popp and U. Engel, *Excimer laser micro texturing of cold forging tool surfaces - Influence on tool life.* CIRP Annals - Manufacturing Technology, 2002. **51**(1): p. 231-234.
62. Geiger, M., S. Roth and W. Becker, *Influence of laser-produced microstructures on the tribological behaviour of ceramics.* Surface and Coatings Technology, 1998. **100-101**(1-3): p. 17-22.
63. Bowden, F.P. and D. Tabor, *Theory of metallic friction and role of shearing and ploughing*. 1942. p. 7-38.
64. Bowden, F.P. and D. Tabor, *Metallic friction: theory.* Bulletin of the Council for Scientific and Industrial Reseach, 1942(145): p. 59.
65. Bowden, F.P. and D. Tabor, *Mechanism of metallic friction.* Nature, 1942. **149**: p. 197-199.
66. Bowden, F.P., A.J.W. Moore and D. Tabor, *The ploughing and adhesion of sliding metals.* Journal of Applied Physics, 1943. **14**: p. 80-91.
67. Persson, *Sliding Friction , Physical Principals and Applications*. second ed. 2000: Springer.
68. Bhushan, B., *Principles and Applications of Tribology*. 1999.
69. Bhushan, B.a.G., B., *Handbook of Tribology* 1991.
70. Tabor, D., *FRICTION - THE PRESENT STATE OF OUR UNDERSTANDING.* Journal of lubrication technology, 1981. **103**(2): p. 169-179.
71. Chang, W.R., I. Etsion and D.B. Bogy. *STATIC FRICTION COEFFICIENT MODEL FOR METALLIC ROUGH SURFACES*. in *Papers Presented at the ASLE/ASME Tribology Conference.* 1987. San Antonio, TX, USA: ASME, USA, 7p.
72. Chang, W.R., D.B. Bogy and I. Etsion. *ELASTIC-PLASTIC MODEL FOR THE CONTACT OF ROUGH SURFACES*. in *ASME/ASLE Joint Tribology Conference.* 1986. Pittsburgh, PA, USA: ASME.
73. Kogut, L. and I. Etsion, *Elastic-plastic contact analysis of a sphere and a rigid flat.* Journal of Applied Mechanics, Transactions ASME, 2002. **69**(5): p. 657-662.
74. Kogut, L. and I. Etsion, *A semi-analytical solution for sliding inception of a spherical contact.* Journal of Tribology, 2003. **125**(3): p. 499-506.
75. Nosonovsky, M. and B. Bhushan, *Multiscale friction mechanisms and hierarchical surfaces in nano- and bio-tribology.* Materials Science & Engineering R, 2007. **58**(3-5): p. 162-93.
76. Nosonovsky, M. and B. Bhushan, *Biomimetic superhydrophobic surfaces: Multiscale approach.* Nano Letters, 2007. **7**(9): p. 2633-2637.
77. Nosonovsky, M. and B. Bhushan, *Multiscale effects and capillary interactions in functional biomimetic surfaces for energy conversion and green engineering.* Philosophical Transactions of the Royal Society London, Series A (Mathematical, Physical and Engineering Sciences), 2009. **367**(1893): p. 1511-39.
78. McFarlane, J.S. and D. Tabor, *Adhesion of solids and effect of surface films.* Royal Society of London -- Philosophical transactions -- Proceedings Series A, 1950. **202**(1069): p. 224-243.
79. McFarlane, J.S. and D. Tabor, *Relation between friction and adhesion.* Royal Society of London -- Philosophical transactions -- Proceedings Series A, 1950. **202**(1069): p. 244-253.

80. Bhushan, B. and M.F. Doerner, *Role of mechanical properties and surface texture in the real area of contact of magnetic rigid disks.* Transactions of the ASME. Journal of Tribology, 1989. **111**(3): p. 452-8.
81. Bhushan, B., B.S. Sharma and R.L. Bradshaw, *Friction in magnetic tapes. I. Assessment of relevant theory.* ASLE Transactions, 1984. **27**(1): p. 33-44.
82. N.A. Burnham , A.J.K., *Surface Forces and Adhesion*, in *Handbook of Micro/Nanotribology*, B. Bhushan, Editor. 1997, CRC Press.
83. Johnson, K.L., K. Kendall and A.D. Roberts, *Surface energy and the contact of elastic solids.* Proceedings of the Royal Society of London, Series A (Mathematical and Physical Sciences), 1971. **324**(1558): p. 301-13.
84. Derjaguin, B.V., V.M. Muller and Y.P. Toporov, *Effect of contact deformations on the adhesion of particles.* Journal of Colloid and Interface Science, 1975. **53**(2): p. 314-26.
85. Tabor, D., *Junction growth in metallic friction: the role of combined stresses and surface contamination.* Proceedings of the Royal Society of London, Series A (Mathematical and Physical Sciences), 1959. **251**: p. 378-393.
86. Tabor, D. *Surface forces and surface interactions*. 1977. USA.
87. Johnson, K.L., *Adhesion and friction between a smooth elastic spherical asperity and a plane surface.* Proceedings of the Royal Society of London, Series A (Mathematical, Physical and Engineering Sciences), 1997. **453**(1956): p. 163-79.
88. Johnson, *Contact Mechanics*. 1985: Cambridge University Press.
89. Greenwood,J.A and ,.J.B.P.Williamson, *Contact of Nominally Flat Surfaces.* Proc. R. Soc. Lond., 1966. **295**(1442): p. 300-319.
90. Greenwood, J.A. and J.H. Tripp, *The contact of two nominally flat rough surfaces.* Proceedings of the Institution of Mechanical Engineers, 1970. **185**(48): p. 625-33.
91. Tayebi, N. and A.A. Polycarpou, *Modeling the effect of skewness and kurtosis on the static friction coefficient of rough surfaces.* Tribology International, 2004. **37**(6): p. 491-505.
92. Adams, G.G. and M. Nosonovsky, *Contact modeling - forces.* Tribology International, 2000. **33**(5): p. 431-442.
93. Jackson, R.L. and J.L. Streator, *A multi-scale model for contact between rough surfaces.* Wear, 2006. **261**(11-12): p. 1337-47.
94. McCool, J.I., *Comparison of models for the contact of rough surfaces*. Wear, 1986. **107**(1): p. 37-60.
95. Polycarpou, A.A. and I. Etsion, *Analytical approximations in modeling contacting rough surfaces.* Journal of Tribology, 1999. **121**(2): p. 234-239.
96. Yu, N. and A.A. Polycarpou, *Contact of rough surfaces with asymmetric distribution of asperity heights.* American Society of Mechanical Engineers, Tribology Division, TRIB, 2001(69): p. 1-10.
97. Yu, N. and A.A. Polycarpou, *Extracting summit roughness parameters from random Gaussian surfaces accounting for asymmetry of the summit heights.* Journal of Tribology, 2004. **126**(4): p. 761-766.
98. Tangena, A.G. and P.J.M. Wijnhoven, *Finite element calculations on the influence of surface roughness on friction.* Wear, 1985. **103**(4): p. 345-54.
99. Faulkner, A. and R.D. Arnell, *The development of a finite element model to simulate the sliding interaction between two, three-dimensional, elastoplastic, hemispherical asperities.* Wear, 2000. **242**(1-2): p. 114-22.

100. Faulkner, A., K.C. Tang, S. Sen and R.D. Arnell, *Finite element solutions comparing the normal contact of an elastic-plastic layered medium under loading by (a) a rigid and (b) a deformable indenter.* Journal of Strain Analysis for Engineering Design, 1998. **33**(6): p. 411-418.
101. Jackson, R.L. and I. Green, *A finite element study of elasto-plastic hemispherical contact against a rigid flat.* Transactions of the ASME. Journal of Tribology, 2005. **127**(2): p. 343-54.
102. Komvopoulos, K., *Finite element analysis of a layered elastic solid in normal contact with a rigid surface.* Journal of Tribology, 1988. **110**(3): p. 477-485.
103. Komvopoulos, K., *Elastic-plastic finite element analysis of indented layered media.* Transactions of the ASME. Journal of Tribology, 1989. **111**(3): p. 430-9.
104. Kral, E.R. and K. Komvopoulos, *Three-dimensional finite element analysis of subsurface stresses and shakedown due to repeated sliding on a layered medium.* Transactions of the ASME. Journal of Applied Mechanics, 1996. **63**(4): p. 967-73.
105. Kral, E.R., K. Komvopoulos and D.B. Sogy, *Finite element analysis of repeated indentation of an elastic-plastic layered medium by a rigid sphere. II. Subsurface results.* Transactions of the ASME. Journal of Applied Mechanics, 1995. **62**(1): p. 29-42.
106. Ye, N. and K. Komvopoulos, *Effect of residual stress in surface layer on contact deformation of elastic-plastic layered media.* Journal of Tribology, 2003. **125**(4): p. 692-699.
107. Gong, Z.Q. and K. Komvopoulos, *Effect of surface patterning on contact deformation of elastic-plastic layered media.* Journal of Tribology, 2003. **125**(1): p. 16-24.
108. Gong, Z.Q. and K. Komvopoulos, *Mechanical and thermomechanical elastic-plastic contact analysis of Layered media with patterned surfaces.* Transactions of the ASME. Journal of Tribology, 2004. **126**(1): p. 9-17.
109. Ramachandra, S. and T.C. Ovaert, *Effect of coating geometry on contact stresses in two-dimensional discontinuous coatings.* Transactions of the ASME. Journal of Tribology, 2000. **122**(4): p. 665-71.
110. Shao, W., *Real contact area of fractal-regular surfaces and its implications in the law of friction.* Transactions of the ASME. Journal of Tribology, 2004. **126**(1): p. 1-8.
111. Zhuangde, J., W. Hairong and F. Bin. *Research into the application of fractal geometry in characterising machined surfaces*. in *8th International Conference on Metrology and Properties of Engineering Surfaces, 26-29 April 2000*. 2001. UK: Elsevier.
112. Borodich, F.M. and D.A. Onishchenko, *Similarity and fractality in the modelling of roughness by a multilevel profile with hierarchical structure.* International Journal of Solids and Structures, 1999. **36**(17): p. 2585-612.
113. Ye, N. and K. Komvopoulos, *Effect of residual stress in surface Layer on contact deformation of elastic-plastic Layered media.* Transactions of the ASME. Journal of Tribology, 2003. **125**(4): p. 692-9.
114. Sahoo, P. and S.K.R. Chowdhury, *A fractal analysis of adhesive friction between rough solids in gentle sliding.* Proceedings of the Institution of Mechanical Engineers, Part J (Journal of Engineering Tribology), 2000. **214**(J6): p. 583-95.
115. Warren, T.L. and D. Krajcinovic, *Fractal models of elastic-perfectly plastic contact of rough surfaces based on the cantor set.* International Journal of Solids and Structures, 1995. **32**(19): p. 2907-2922.

116. Liu, S.H., T. Kaplan and L.J. Gray. *Theory of the AC response of fractal interfaces*. in *1987 IEEE International Symposium on Circuits and Systems (Cat. No.87CH2394-5), 4-7 May 1987*. 1987. New York, NY, USA: IEEE.
117. *Abaqus Documentations 6.10*, Dassault Systeme Simulia Corp, 2010.
118. Miyoshi, K and D.Buckley, *Friction and Wear Characterisics of Iron-Chromium Alloys in Contact with Themselves and Silicon Carbide.* NASA Technical Paper, 1979., #**1387**.
119. Hongben, Z. and W. Peukert, *Modeling adhesion forces between deformable bodies by FEM and hamaker summation.* Langmuir, 2008. **24**(4): p. 1459-1468.
120. Gotzinger, M. and W. Peukert, *Particle adhesion force distributions on rough surfaces.* Langmuir, 2004. **20**(13): p. 5298-5303.
121. Meine, K., K. Klob, T. Schneider and D. Spaltmann. *The influence of surface roughness on the adhesion force*. 2004. UK: Wiley.
122. Maugis, D. and H.M. Pollock, *Surface forces, deformation and adherence at metal microcontacts.* Acta Metallurgica, 1984. **32**(9): p. 1323-34.
123. Israelachvili, J.N., 2nd ed.; and : London, *Intermolecular and Surface Forces*. 2 ed. 1992, London: Academic Press. 204-205.
124. Komvopoulos, K., *Adhesion and friction forces in microelectromechanical systems: mechanisms, measurement, surface modification techniques, and adhesion theory.* Journal of Adhesion Science and Technology, 2003. **17**(4): p. 477-517.
125. Tayebi, N. and A.A. Polycarpou, *Adhesion and contact modeling and experiments in microelectromechanical systems including roughness effects.* Microsystem Technologies, 2006. **12**(9): p. 854-869.
126. Bachmann, D., S. Kuhne and C. Hierold, *Determination of the adhesion energy of MEMS structures by applying Weibull-type distribution function.* Sensors and Actuators, A: Physical, 2006. **132**(1 SPEC. ISS.): p. 407-414.
127. Bachmann, D. and C. Hierold, *Determination of the pull-off forces and pull-off dynamics of an electrostatically actuated silicon disk.* Journal of Microelectromechanical Systems, 2008. **17**(3): p. 643-652.
128. Ando, Y. and J. Ino, *Friction and pull-off forces on submicron-size asperities.* Wear, 1998. **216**(2): p. 115-122.
129. Bhushan, B., *Adhesion and stiction: mechanisms, measurement techniques, and methods for reduction.* Journal of Vacuum Science & Technology B (Microelectronics and Nanometer Structures), 2003. **21**(6): p. 2262-96.

PUBLICATIONS

a. Refereed Journal Papers

1. **O. Rashwan**, V. Stoilov, A. Alpas, and A. Guerrero, *Effect of Surface Patterning on the Adhesive Friction*. Proceedings of ASME 2012 International Mechanical Engineering Congress & Exposition**,** IMECE2012-89644, accepted on July9, 2012.
2. **O. Rashwan** and V. Stoilov, *Numerical Model of Microstructure and Fracture of Coated Aluminum Alloys: A Novel Design Approach.* Materials Science Forum, 2012, **706-709,** p:2640-2645.
3. **O. Rashwan**, V. Stoilov, and A. Alpas (2013), *Laser Surface Texture for Controlled Friction: Numerical and Experimental. To be Submitted*.
4. **O. Rashwan**, V. Stoilov, and A. Alpas (2013), *The Effect of Hexagonal Patterning on Coefficient of Friction* ". *To be submitted*.

b. Refereed Conference Proceedings and Conference Presentations

1. **V.Stoilov**, O.Rashwan and A. Alpas, *Effect of Surface Texturing on Friction Reduction under Dry Sliding Contact.* The 68th annual meeting and exhibition of STLE (Society of Tribologists and Lubrication Engineers 2013), Detroit, MI, May 5-9, 2013.
2. **O. Rashwan**, V.Stoilov, A. Alpas, and A. Guerrero, *Effect of Surface Patterning on the Adhesive Friction.* ASME 2012 International Mechanical Engineering Congress & Exposition, Houston, Texas, Nov 9-15, 2012.
3. **O. Rashwan**, V. Stoilov, and A. Alpas*, Surface Texture for Reduction and Control of Friction*. Proceedings of the 67th annual meeting and exhibition

of STLE (Society of Tribologists and Lubrication Engineers, accepted March16, 2012, St. Louis, Missouri, May 6 -10, 2012.

4. **O. Rashwan**, V.Stoilov, A.Alpas, and A.Guerrero, *The Effect of the Surface Texturing on Pull off Forces.* 24th Canadian materials Science Conference 2012, London, ON, June 5 -8,2012.
5. **O. Rashwan**, V. Stoilov, and A. Alpas, *Surface Texture for Reduction and Control of Friction*. The 67th annual meeting and exhibition of STLE (Society of Tribologists and Lubrication Engineers 2012), St. Louis , Missouri, May 6 -10, 2012.
6. ***O. Rashwan** and V. Stoilov, "Macro-Scale Friction of Multiscale Textured Surface"*,7thInternational Conference on Processing and Manufacturing of advanced Materials, Quebec city, Quebec, Canada, August 1-5, 2011.
7. **O. Rashwan** and V.Stoilov, *Numerical Model of Microstructure and Fracture of Coated Aluminum Alloys: A Novel Design Approach.* 7thInternational Conference on Processing and Manufacturing of advanced Materials, Quebec city, Quebec, August 1-5, 2011.
8. **O. Rashwan** and V. Stoilov, *Multi-Scale Contact Modelling of Textured Surfaces Under Dry Sliding Conditions*. 37th International Conference on Metallurgical Coating & Thin Films, San Diego, CA, April 26-30, 2010.
9. **O. Rashwan** and V. Stoilov, *Microstructure and Properties Evolution of Al/Si Coated Surfaces.* 37th International Conference on Metallurgical Coating & Thin Films, San Diego, CA, April 26-30, 2010.

10. **O. Rashwan** and V. Stoilov. *Mechanical Analysis of Al/Si Alloys Layered and Textured Surfaces*. 21th Canadian Materials Science Conference, Kingston, ON,   June 9-11, 2009.

VITA AUCTORIS

Name: Ola Rashwan

Place of Birth: Egypt

Education: The American University in Cairo, B.Sc. in Mechanical Engineering with high honors, Cairo, Egypt, 2001.
The American University in Cairo, M.Sc., Industrial Engineering Cairo, Egypt, 2006.
University of Windsor, PhD in Engineering Materials, Windor,
Ontario, Canada, 2013